UNIVERSITE BRETAGNE LOIRE

UNIVERSITÉ DE NANTES

Thèse de Doctorat

Assadour KHANJIAN

Mémoire présenté en vue de l'obtention du
grade de Docteur de l'Université de Nantes
sous le sceau de l'Université Bretagne Loire

École doctorale : *n° 602*
Discipline : *Sciences pour l'Ingénieur*
Spécialité : *Energétique-Thermique-Combustion*
Unité de recherche : *LARIS EA 7315 Polytech Angers*

Soutenue le *07 Juin 2019*
Thèse N° :

Auto-Adapting Vortex Generator for Smart Heat Exchangers

JURY

Président du jury	**M. Maxime PONTIE**	Professeur, Université d'Angers
Rapporteurs :	**M. Didier SAURY**	Professeur, ENSMA Poitiers
	Mme Monica SIROUX	Professeur, INSA Strasbourg
Examinateurs :	**M. Daniel BOUGEARD**	Professeur, IMT Lille Douai
	M. Ahmed Ould El Moctar	Maître de conférences HDR, Polytech Nantes
Directeur de Thèse :	**M. Thierry LEMENAND**	Maître de conférences HDR, Polytech Angers
Co-directeur de Thèse :	**M. Charbel HABCHI**	Maître de conférences, NDU University (Liban)
	M. Serge RUSSEIL	Maître de conférences, IMT Lille Douai

ACKNOWLEDGMENTS

First and foremost, I would like to express my sincere gratitude to my advisors: Dr. Thierry Lemenand, Dr. Charbel Habchi, Dr. Serge Russeil, and Dr. Daniel Bougeard. I want to thank you for the continuous support during my PhD study and related research and for your patience, motivation and immense knowledge. Your guidance helped me throughout the time of research and writing of this thesis.

I would like to thank my committee members M. Didier Saury, Mme Monica Siroux, M. Maxime Pontie and M. Ahmed Ould El Moctar.

A special thanks to my family. Words cannot express how grateful I am to my father, mother and sister for all the sacrifice that they have made on my behalf. Your support and prayers were what sustained me this far. I would like to wholeheartedly thank my beloved wife Carine for her unceasing support and unconditional love. I can't thank you enough for encouraging me throughout this experience and through all its ups and downs. I cannot forget you my son, Hovag. The joy you have brought into the family through your smiles inspired me with meaning, purpose and perseverance.

Finally, I thank my Lord and Savior Jesus Christ for guiding and protecting me through all the difficulties. You are the reason why I have come so far, and You'll be the reason why I will keep going.

Trust in the LORD with all your heart
and lean not on your own understanding;
in all your ways submit to him,
and he will make your paths straight.

Proverbs 3:5-6, Holy Bible

Contents

List of Figures

List of Tables

List of Symbols

Nu	Nusselt Number	β	Roll angle
Nu_0	Nusselt Number of the empty channel	D_h	Hydraulic Diameter
Nu_l	Local Nusselt Number	h	Convective heat transfer coefficient
Nu_{avg}	Average Nusselt Number	$\dot{m}$	Mass flow rate
Nu_x	Local Nusselt number	$\dot{q}$	Heat transfer rate
C_f	Coefficient of Friction factor	ΔT_{lm}	Log mean Temperature difference
C_{f0}	Coefficient of Friction factor of the empty channel	c	Convergence order
		ε	Relative error
ξ	Friction factor	θ	Dimensionless Temperature
α	Angle of attack	Re	Reynolds number
C_p	Specific heat at constant pressure	Pr	Prandtl Number
P	Pressure	λ	helicity
μ	Fluid Dynamic Viscosity	$\vec{\omega}$	Momentum vector
$\vec{u}$	Velocity vector	q''	Average wall heat flux
k_f	Thermal conductivity of Fluid	f_{Darcy}	Darcy's friction factor
ρ	Density	U	Mean Velocity
T	Temperature	f	Friction factor
H	Height	E	Young Modulus of Elasticity
W	Width	η	Enhancement factor
L	Length	Φ	Enhancement factor od FSI vs Static

RÉSUMÉ de la THÈSE

1. Objectif

L’objectif de cette étude est d’étudier l’utilisation de générateurs de vortex auto-adaptatifs et pilotés par la pression. Il est ainsi crucial d'étudier et d'évaluer les concepts des générateurs de vortex et leur effet sur l'amélioration du transfert de chaleur. Un aperçu détaillé des méthodes de transfert de chaleur est présenté dans une revue de la littérature, principalement divisée en méthodes passives et actives, l’accent étant mis sur les générateurs de vortex. Les générateurs de vortex sont l’une des méthodes passives qui créent des flux secondaires, perturbent la croissance de la couche limite et créent des flux tourbillonnants qui améliorent l’échange entre les parois et le fluide central, améliorant ainsi le transfert de chaleur. Dans le cas des générateurs de vortex passifs, le nombre de vortex générés est limité. D'autre part, les méthodes actives offrent une flexibilité supplémentaire en contrôlant la fréquence, la vitesse et l'amplitude des oscillations des générateurs de vortex, influençant ainsi le nombre et la force des vortex créés. Néanmoins, les méthodes actives nécessitent la mise en œuvre d'une source d'énergie externe supplémentaire pour contrôler les générateurs de vortex, ce qui entraîne une complexité accrue de l'installation du système et une consommation d'énergie.

Pour pouvoir concevoir un générateur de vortex auto-adaptatif, une stratégie est proposée dans laquelle l'étude est démarrée avec des cas plus simples et a été développée progressivement pour aboutir au générateur de vortex auto-adaptatif.

2. Démarche

L’objectif de cette thèse est de fournir des conceptions pour différents types de générateurs de vortex, et d'analyser les effets du générateur de vortex commandé par la pression lorsque l'angle d'inclinaison est affecté par la vitesse d'écoulement et l'effet de cette déviation sur les modèles d'écoulement, le transfert de chaleur et l'amélioration des performances thermiques de l'échangeur de chaleur.

Cette étude vise à étudier différentes géométries de VG, placées dans un canal rectangulaire, en commençant par un VG statique, puis par une étude plus approfondie d’un VG « auto-

adaptatif ». Le nouveau concept d'auto-adaptatif correspond à un VG dont la géométrie est susceptible d'être modifiée en fonction de l'évolution des modes de fonctionnement de l'échangeur thermique. Dans ce travail de thèse, la forme du promoteur de vortex peut être modifiée en fonction des variations de la vitesse d'écoulement à l'entrée. Dans tous les cas, des études paramétriques sont effectuées pour pouvoir évaluer la conception proposée. Un résultat de calcul numérique du transfert de chaleur par convection laminaire est pris en compte pour chaque cas et son effet sur l'amélioration thermique du système est analysé.

Une première géométrie, un canal rectangulaire équipé d'un générateur de vortex de paires d'ailettes rectangulaires situé sur la paroi inférieure du canal, est prise en compte. Différentes valeurs d'angle de roulis β comprises dans la plage [20°–90°] sont prises en compte, tout en maintenant un angle d'attaque constant (α=30°) dans tous les cas. Le nombre de Reynolds est fixé à deux valeurs, 456 et 911. Les analyses locales et globales sont effectuées à l'aide de paramètres tels que le nombre de Nusselt et le coefficient de frottement. De plus, la position et la force des tourbillons créés dans le conduit sont étudiées, soulignant leur effet sur les taux de transfert de chaleur. La variation longitudinale de la position adimensionnelle du vortex principal est étudiée, ainsi que la variation longitudinale du nombre moyen de Nusselt et du facteur de frottement. Afin d'étudier l'influence de l'angle de roulis β du VG sur l'amélioration du transfert de chaleur, les valeurs globales du nombre de Nusselt et du facteur de frottement sont discutées, ainsi que le facteur d'amélioration. Cette étude est discutée au chapitre 4 et les résultats de celle-ci sont publiés dans un article intitulé « *Effect of rectangular winglet pair roll angle on the heat transfer enhancement in laminar channel flow* », publié dans *International Journal of Thermal Sciences* en 2017.

Une deuxième géométrie est également prise en compte, où l’amélioration du transfert de chaleur est étudiée dans un flux laminaire à plaques parallèles utilisant une aile rectangulaire VG. Des simulations numériques tridimensionnelles sont effectuées pour étudier l'effet de l'angle d'attaque du VG sur le transfert de chaleur et la perte de charge. Pour cela, le nombre de Nusselt et le facteur de friction sont étudiés selon des perspectives locales et globales. Pour toutes les valeurs d'angle d'attaque, le régime d'écoulement est maintenu laminaire. La distribution dans le sens de la largeur du nombre de Nusselt moyen sur la paroi inférieure est étudiée pour les valeurs des angles d'attaque α dans l'intervalle [10°–30°] ainsi que pour le cas du canal vide simulé avec

les mêmes conditions de fonctionnement. La variation du facteur de frottement en fonction de l'écoulement est également analysée. Pour étudier l'influence de l'angle d'attaque α du VG sur l'amélioration du transfert de chaleur, les valeurs globales du nombre de Nusselt et du facteur de frottement sont discutées, ainsi que le facteur d'amélioration des valeurs tracées en fonction de α. Cette étude est discutée au chapitre 5 et les résultats de celle-ci sont publiés dans un article intitulé « *Effect of the angle of attack of a rectangular wing on the heat transfer enhancement in channel flow at low Reynolds number* », publié dans *Heat and Mass Transfer* en 2017.

Le chapitre 6 propose une étude auto-adaptative pilotée par la pression. Après avoir étudié l'effet de l'angle incident du VG sur la performance du transfert de chaleur, il est crucial de proposer une conception où les angles d'attaque du VG sont auto-adaptables avec la vitesse d'entrée. Pour pouvoir étudier ce phénomène, un plan de calcul est défini dans lequel l'interaction fluide-solide (FSI) est prise en compte, où l'angle d'attaque du VG est auto-adapté par la valeur de la vitesse d'entrée. Pour ce faire, deux cas différents sont étudiés pour la validation de la conception, l'un pour le cas en 2D et l'autre en 3D. Dans le cas de la simulation 2D, le domaine de calcul proposé par Turek et Hron [8] est étudié et les résultats sont comparés à ceux présentés dans l'étude de Turek et Hron [8]. De plus, une étude expérimentale pour un cas 3D est réalisée avec un générateur de vortex à aile rectangulaire et les résultats sont comparés à ceux obtenus à partir de la simulation pour une validation du cas 3D.

Enfin, le domaine de calcul du générateur de vortex à aile rectangulaire est pris en compte en tant que domaine 2D et un VG flexible est défini avec l'angle optimal obtenu, comme indiqué au chapitre 5. Dans les mêmes cas opératoires, des simulations VG statique et VG auto-adaptative sont effectuées et leurs résultats sont étudiés.

Le chapitre 7 présente la conclusion et les perspectives. Les générateurs de vortex auto-adaptatifs en sont encore à leurs premiers stades de développement en ce qui concerne les performances thermiques d'un échangeur de chaleur, plusieurs recommandations et suggestions sont formulées en fin de manuscrit.

3. Résultats

Dans la première partie de l'étude, les caractéristiques de transfert de chaleur et d'écoulement de fluide dans un conduit rectangulaire avec générateur de tourbillons à paires d'ailettes

rectangulaires (RWPVG) inséré dans sa paroi inférieure font l'objet d'une simulation numérique. Pour différentes valeurs de l'angle de roulis du générateur de tourbillon statique (β), des paramètres hydrodynamiques et thermiques locaux et globaux sont calculés et étudiés. L'objectif de ces études est de déterminer l'effet de l'angle de roulis sur l'amélioration du transfert de chaleur. Il a été conclu que pour des valeurs d'angle de roulis élevées (proches de β=90°), il est observé que l'hélicité augmente juste après que l'écoulement rencontre le VG où les vortex sont d'abord formés. Le pic d'hélicité pour β=90° est environ 12 fois plus élevé que celui pour β=20°, ce qui signifie des vortex plus énergétiques. De plus, l'augmentation de la vitesse moyenne d'écoulement, c'est-à-dire le nombre de Reynolds, conduit à une augmentation de l'hélicité. On observe que pour Re=456, la position X/H du vortex principal mesurée à partir de la paroi inférieure commence en position basse et augmente le long du conduit jusqu'à atteindre une valeur maximale d'environ 0,5 représentant le milieu du conduit pour la valeur la plus élevée de l'angle de roulis β. Tandis que dans le cas d'un nombre de Reynolds plus élevé, l'emplacement adimensionnel du vortex principal augmente brusquement à Z/H=6,5, puis augmente continuellement le long du conduit. Pour Re=911, la valeur la plus élevée de X/H=0,5 est atteinte par les valeurs élevées de β. Alors que pour β=30°, la valeur est X/H=0,35 et pour β=20° X/H=0,2. Il est crucial de prendre en compte qu'en augmentant la valeur de l'angle de roulis, non seulement le transfert de chaleur sera amélioré mais également la perte de charge augmentera. Pour être en mesure de prendre une décision concernant ce problème, nous étudions le facteur d'amélioration lorsque le transfert de chaleur et la perte de charge sont pris en compte. Pour Re=456, il est montré que le facteur d'amélioration augmente de façon monotone avec l'augmentation de l'angle de roulis β, atteignant sa valeur maximale de 1,20 à β=90°. Par contre, dans le cas de Re=911, le profil du facteur d'amélioration commence à augmenter avec l'angle β jusqu'à atteindre une valeur maximale de 1,32 près de β=70°. Ainsi, on peut considérer que pour Re=911 l'angle de roulis optimal parmi les valeurs testées de β conduisant au meilleur rehaussement est de 70° et non l'angle le plus élevé, tandis que pour Re=456 la valeur optimale de β parmi celles testées est l'angle le plus élevé 90°. Après toutes ces investigations, il est crucial de mentionner que l'angle de roulis β a un effet significatif sur l'amélioration du transfert de chaleur.

Dans la deuxième partie de l'étude, nous analysons numériquement le comportement en matière de transfert de chaleur et d'écoulement de fluide dans un canal à plaques parallèles avec

générateur de tourbillon à aile rectangulaire (RWVG) inséré dans la paroi inférieure. Pour différentes valeurs d'angle d'attaque α, les paramètres locaux et globaux sont calculés et étudiés pour comprendre l'effet de l'angle d'incidence sur l'amélioration du transfert de chaleur. Il a été conclu que pour les fortes valeurs d'attaque (proches de α=30°), les vortex générés s'élargissaient et étaient plus énergétiques le long de la direction longitudinale que pour les faibles valeurs (c'est-à-dire α=10°). En outre, on observe que l'hélicité augmente juste après que l'écoulement rencontre le VG où les vortex sont d'abord formés. Le pic d'hélicité pour α=30° est environ 6 fois plus élevé que celui pour α=10°, ce qui signifie des vortex d'énergie plus élevée. De plus, on observe que pour α dans la plage [10°–25°], la position verticale sans dimension X/H du vortex principal commence en position basse et augmente le long du canal jusqu'à atteindre une valeur maximale à la sortie du canal (Z=15H) autour de X=0,5H représentant le milieu du canal, pour le cas α=25°, il atteint une valeur maximale de X=0,58H. En revanche, pour le cas α=30°, la position X/H sans dimension atteint une valeur maximale de X=0,68H avant la sortie du canal, puis redescend pour atteindre 0,55H à la fin du canal. En conclusion de cette étude, le facteur d'amélioration thermique commence à augmenter avec l'angle d'attaque jusqu'à atteindre une valeur maximale de 1,043 représentant 4,3% d'amélioration à α=25°, au-delà duquel sa valeur diminue. On peut considérer que l'angle d'attaque optimal du générateur de vortex qui permet la meilleure optimisation dans ces conditions de fonctionnement est de 25° et non l'angle le plus élevé.

Dans la troisième partie de l'étude, l'application des générateurs de vortex à l'amélioration du transfert de chaleur dans les échangeurs de chaleur a été approfondie. Le concept du générateur de vortex auto-adaptatif commandé par la pression est présenté et étudié. Après avoir validé le code 2D FSI en comparant les résultats avec ceux de Turek [8], il était important de préparer un banc expérimental avec générateur de vortex auto-adaptatif et de comparer les résultats avec celui du code 3D FSI. Les propriétés mécaniques et physiques du VG étaient préoccupantes dans cette étude pour pouvoir présenter une flèche acceptable à une vitesse d'admission raisonnable. Après des validations expérimentales et des modèles de calcul, le domaine de calcul du chapitre 5 est utilisé pour lequel le VG est auto-adaptatif par rapport à l'écoulement. Différentes valeurs de nombres de Reynolds sont utilisées dans les simulations 2D FSI et leurs résultats sont comparés à ceux du VG statique. Après avoir représenté la température locale et les contours de vitesse, il était intéressant d'étudier certains paramètres globaux affectés par l'adaptation

automatique VG. En étudiant l'effet thermique, il était clair que le VG statique avait un effet plus important sur le transfert de chaleur que celui de l'auto-adaptatif. Pour tous les nombres de Reynolds, la courbe du VG statique est supérieure à celle de l'auto-adaptatif. D'autre part, concernant le paramètre du facteur de frottement global, les VG auto-adaptatifs ont une valeur inférieure et, à mesure que le nombre de Reynolds augmente, le facteur de frottement diminue. Cependant, pour le VG statique, la valeur de départ est supérieure à celle de l'auto-adaptatif et, à mesure que le nombre de Reynolds augmente, il continue d'augmenter. Pour pouvoir étudier et analyser les performances globales de la conception, le facteur d'amélioration thermique est étudié pour tous les nombres de Reynolds : l'amélioration obtenue par le VG auto-adaptatif est supérieure à celle du VG statique, et à mesure que le nombre de Reynolds augmente l'amélioration augmente aussi.

Enfin, cette étude a identifié plusieurs conceptions de configuration pour les générateurs de vortex statiques et auto-adaptatifs. Les systèmes auto-adaptatifs conçus reposent uniquement sur les forces du fluide, sans aucune source d'énergie externe, ce qui conduit à des échangeurs de chaleur plus efficaces et compacts. Cependant, il y aura toujours des suggestions et de nouvelles idées pour améliorer les conceptions fournies dans ce manuscrit, car la méthode proposée et le champ d'interaction fluide-structure appliqué au transfert de chaleur n'ont toujours pas atteint leur niveau de maturité et peuvent toujours être considérés comme innovants. Comme les premiers résultats sont prometteurs, les configurations proposées vont servir de base à d'autres études et investigations futures.

CHAPTER 1

INTRODUCTION

1.1 Background

The consumption of the energy during the last decades is in rapid increase due to the dominancy of the electrical equipment in the daily life usage. Because of this problem [1], overheating problems are being created where the need of cooling systems is studied to enhance the performance of the machines and avoid global warming problems. Studies have been intensified in the domain of heat transfer enhancement during the last years. There are many fields and applications where a high-performance heat exchanger is desired for cooling the systems. On a large scale, heat exchangers were the target of these studies [Khoshvaght et al. 2, Ali et al. 3]. Also due to the high usage of electronic devices, compact heat exchangers have been udder study to be developed and enhanced [Alahyari et al. 4]. Since the source of the electrical power is mainly using turbines [Jiang et al. 5] and nuclear power plants [Basu et al. 6], the concept of enhancing the performance of the exchangers became a crucial concern as to be researched and implemented in the industry.

Among all methods existing for heat transfer enhancement, some are based on the idea of generating a secondary flow, which is added to the main flow to intensify the fluid exchange between hot and cold regions in the system. One of these methods involves the use of vortex generators (VG). The VG are whether fixed on the wall or punched on it (Figure 1. 1) [Fiebig 7, Habchi et al. 8].

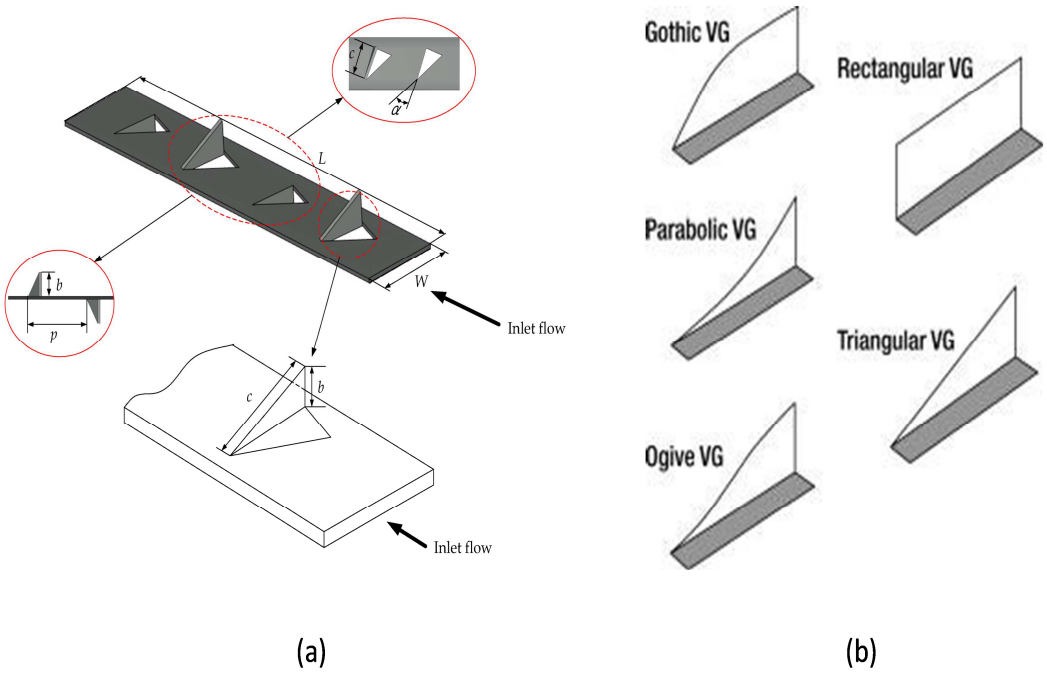

Figure 1. 1: Vortex generators (a) punched VG, (b) fixed VG [7]

In the open literature, most of the studies focus on the effect of the VG aspect ratio, its attack angle and flow rate on the heat transfer enhancement and pressure losses.

1.2 Objectives of this study

The objective of this thesis is to provide designs for different types of vortex generators,
and to analyze the effects of the pressure driven vortex generator where the tilt angle is being affected by the flow velocity and the effect of this deflection on the flow patterns, heat transfer and the enhancement of the thermal performance of the heat exchanger.

This study aims to study different geometries of VG placed in a rectangular channel. Starting with static VG and then with a further study of auto “adaptive VG”. The new concept of auto-adaptative (or self-adaptive) corresponds to a VG whose geometry is likely to be modified according to the changes in the operating modes of the heat exchanger. In our thesis work, the

shape of the vortex promoter can be modified according to the variations of the flow velocity at the entrance. For all the cases parametric studies are done to be able to evaluate the proposed design.
A numerical computation result of laminar convection heat transfer is taken into consideration for each case and their effect on the thermal enhancement of the system is analyzed.

A first geometry, a rectangular channel equipped with a rectangular winglet pair vortex generator located on the bottom wall of the channel, is taken into consideration. Different values of roll angle β in the range [20°–90°] are considered, while maintaining a constant angle of attack (α=30°) for all the cases. Reynolds number is set at two values, 456 and 911. Both local and global analyses are carried out using parameters such as the Nusselt number and the friction coefficient. In addition, the position and strength of the vortices being created in the duct are studied, highlighting their effect on the heat transfer rates. The streamwise variation of the dimensionless location of the main vortex is studied, as well as the streamwise variation of the average Nusselt number and of the friction factor. In order to study the influence of the roll angle β of the VG on the heat transfer enhancement, global values of the Nusselt number and friction factor are discussed, as well as the enhancement factor. This study is discussed in chapter 4 and the outcomes of the study is published as an article "Effect of rectangular winglet pair roll angle on the heat transfer enhancement in laminar channel flow", in International Journal of Thermal Sciences in 2017.

A second geometry is also taken into consideration, where the heat transfer enhancement is studied in a laminar parallel plate flow using rectangular wing VG. Three-dimensional numerical simulations are performed to study the effect of the angle of attack of the VG on the heat transfer and pressure drop. For this aim, Nusselt number and friction factor are studied on local and global perspectives. For all the values of angle of attacks the flow regime is kept laminar. The streamwise distribution of the span-averaged Nusselt number at the bottom wall is studied for values of attack angles α in the range [10°–30°] as well as for the case of the empty channel, simulated with the same operating conditions except the VG which is removed. Also, the streamwise variation of the friction factor is analyzed. To study the influence of the angle of

attack α of the VG on the heat transfer enhancement, global values of the Nusselt number and friction factor are discussed, as well as the enhancement factor which values are plotted versus α. This study is discussed in chapter 5 and the outcomes of the study is published as an article "Effect of the angle of attack of a rectangular wing on the heat transfer enhancement in channel flow at low Reynolds number", in Heat and Mass Transfer in 2017.

As a further study, a pressure driven auto adaptive VG is proposed in chapter 6. After investigating the effect of the incident angle of the VG on the performance of the heat transfer, it is crucial to propose a design where the angles of attack of the VG is auto adaptable with respect to the inlet velocity. To be able to study this phenomenon, a computational design is set where the Fluid Solid Interaction (FSI) is taken into consideration, where the angle of attack of the VG is auto adapted by the value of the inlet velocity. To do so, two different cases are studied for the validation of the design, one for the case of the 2D and the other for 3D. For the case of the 2D simulation, the computational domain proposed by Turek and Hron [8] is studied and the results are compared to that reported in Turek's study. In addition to this, an experimental study for a 3D case is performed with a rectangular wing vortex generator and the results are compared to that obtained from the simulation for a validation of the 3D case.

As a final step, the computational domain of the rectangular wing vortex generator is taken into consideration as a 2D domain and a flexible VG is set having the optimal angle obtained as mentioned in chapter five. For the same cases both static VG and auto adaptive VG simulations are performed, and their outcome are studied.

Chapter 7 presents the conclusion and perspectives. Since the auto adaptive vortex generators are still in their early stages of development in their effect on the thermal performance a heat exchanger, several future recommendations and suggestions are done.

CHAPTER 2

LITERATURE REVIEW

Throughout the history, many methods have been studied to enhance heat transfer in forced convection problems. Different methods of heat transfer enhancement methods have been introduced by Webb [9], and they have been classified as passive, active, or compound methods. Active methods require external power and involve electric, magnetic or acoustic fields. Passive methods involve surface modifications, fluid additives or introduction of protuberances in order to destabilize the flow. Compound method is the combination of both active and passive together. Active methods are more costly due to the need of and additional external energy to the system. On the other hand, the passive method is more common in several usages due to its effectiveness with an affordable cost. [3–6].

Results have shown that specific inserts in the heat exchangers, such as vortex generators, [Fiebig et al. 11] can enhance heat transfer significantly. On the other hand, as a result of this, it is required to add the pumping power due to the increase in the pressure drop. Since this type of vortex generators (VG) is usually fixed and offers limited control or system flexibility, actively controlled VGs at different amplitudes and frequencies of oscillations can solve this problem.

In the last decades, heat transfer enhancement with active flow control has been implemented due to the development of electro-mechanical systems. For example, Ma *et al.* [12] and Yu *et al.* [13] studied vibrating fins that are actuated with piezoelectric material to disrupt the growth of the thermal boundary layer, thus enhancing the convective heat transfer coefficient.

The results of vortex induced vibrations (VIV) have demonstrated that the vortex shedding frequency in some cases coincides with one of the natural frequencies of the structure and as a result of it the phenomena of the resonance occurs with a large displacement of the structure. This is referred by Williamson and Govardhan [14] to as lock-in where the flow in this case supplies energy to the structure instead of damping it, resulting in large amplitude oscillations. However, the effects of this passive fluid structure interaction (FSI) on heat transfer and mixing have not been studied deeply both theoretically and experimentally.

In this thesis, the effect of the pressure driven auto adaptive vortex generators on the heat transfer enactment is being investigated, where the only force used it the force due to the flow of the fluid without and additional external forces being added on the system.

The objective of this chapter is to provide information about the following:

- An overview of the different types of heat exchangers and their specific usages and applications.
- Heat transfer enhancement using flow perturbations with emphasis on passive vortex generators.
- An overview of flow perturbations having active vortex generators.
- Auto adaptive rigid vortex generators and their influence on the heat transfer.
- An overview of the elastic vortex generators driven by the pressure of the flow, which is the concern of this study.

2.1 Heat exchangers

Heat Exchangers are typically classified according to flow arrangement and type of construction. They can be found in many applications such as power systems, aerospace, automobile industry, chemical engineering, heating and air conditioning, electronic chip cooling, internal cooling of gas turbine blades etc.

2.1.1 Concentric tube heat exchangers

Figure 2.1 represents the concentric tube heat exchangers or double pipe heat exchangers, these are the simplest exchangers used in the domain of industries. The inner tube contains the fluid that must be either heated or cooled. The second fluid runs over the tubes that are being heated or cooled so that it can either provide the heat or absorb the heat required. The direction of the flow of the two fluids might be parallel flow or counter flow.

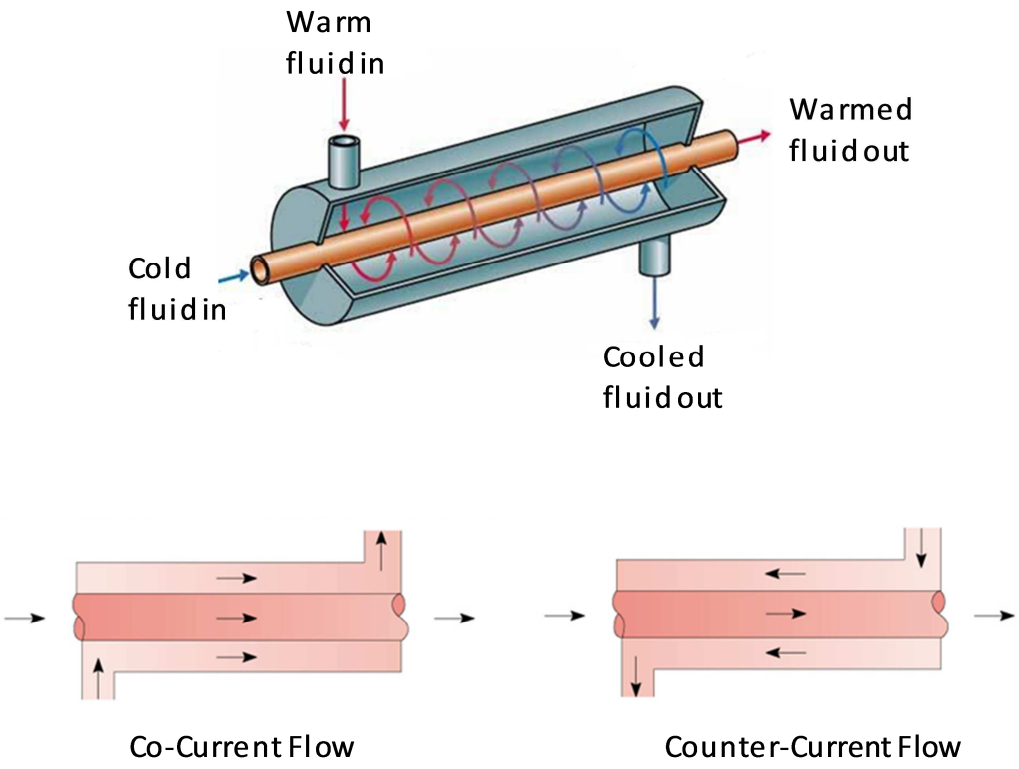

Figure 2.1: Concentric Tube Heat Exchangers [15]

2.1.2 Shell and tube heat exchangers

A shell and tube heat exchanger (Figure 2.2) is a type of heat exchanger mainly used in high pressure applications. This type of heat exchanger consists of a large pressurized shell with a set of tubes inside it. One fluid runs through the tubes, and another fluid flows over the tubes through the shell to transfer heat between the two fluids.

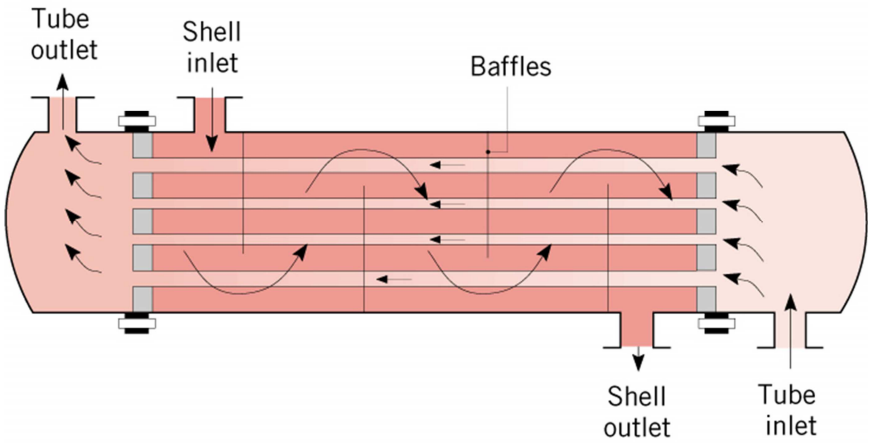

Figure 2.2: Shell and Tube Heat Exchangers [15]

2.1.3 Compact heat exchangers

Compact heat exchangers (Figure 2.3) are used to achieve a very large heat transfer surface area per unit volume. These exchangers have dense arrays of finned tubes or plates and are typically used when at least one of the fluids is a gas and is hence characterized by a small convection coefficient. The geometry of the tubes may be flat or circular; even the fins might be plate or circular. Parallel-plate heat exchangers may be finned or corrugated and may be used in single-pass or multi-pass modes of operation. The flow passages of the compact heat exchangers are small and the flow regime is mostly considered to be laminar flow or transitional.

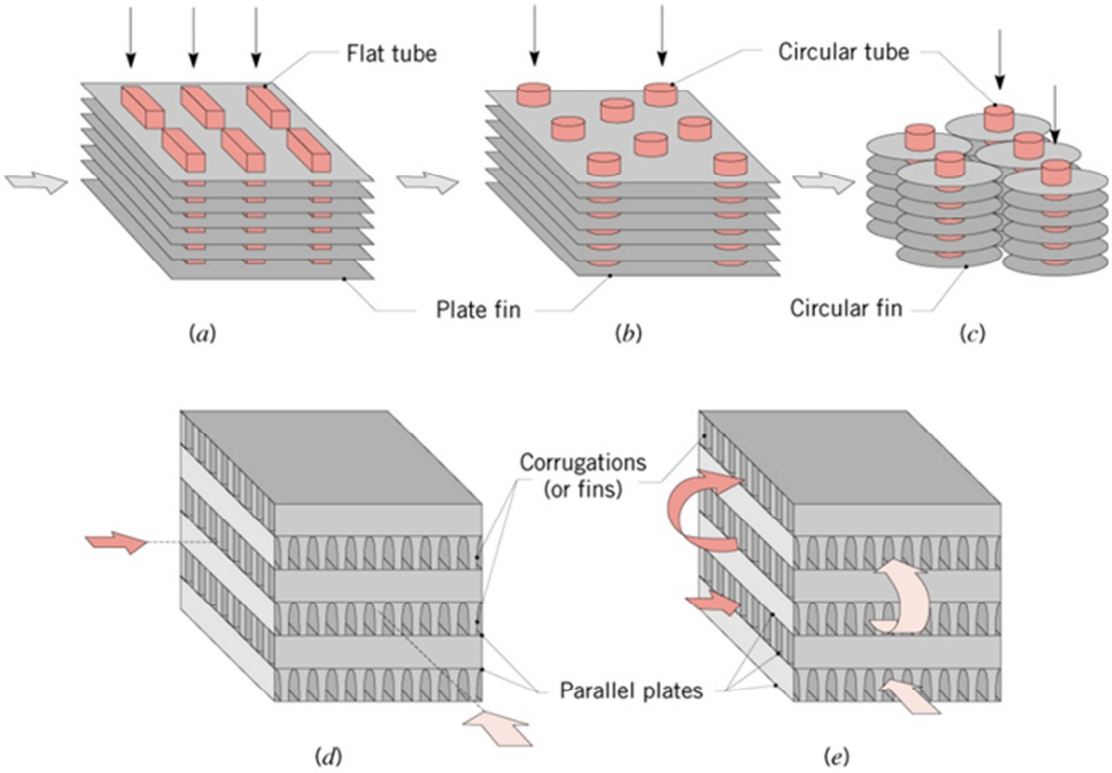

Figure 2.3: Compact Heat Exchangers [15]

2.2 Heat transfer enhancement methods

The passive heat transfer augmentation method does not need any external power input. In the convective heat transfer cases, one of the ways to enhance the heat transfer is by increasing the effective contact surface area. By doing so, the fluid in contact with the exchanger will stay a longer duration in contact with it, increasing the effective heat transfer area, because of this; the heat transfer will be increased.

Another method of heat transfer enhancement is the application of the inserts in the flow. Inserts require additional arrangements to make to fluid flow which enhance and augment the heat transfer. There are different types of inserts such as: Twisted tape, wire coils, ribs, plates…etc.
Among all methods existing for heat transfer enhancement, some are based on the idea of generating a secondary flow, which is added to the main flow to intensify the fluid exchange between hot and cold regions in the system. One of these methods involves the use of vortex

generators (VG). A Vortex Generator (VG) is considered as a passive flow control device which modifies the boundary layer fluid motion bringing momentum from the outer region into the inner region. Due this transfer of energy, the velocity of the inner region is increased at the same time as the boundary layer thickness is decreased, which in turn causes the separation of the flow to be delayed.

2.3 Vortex generators (VG)

2.3.1 The concept of the vortex generators

Compact heat exchangers are used in many different applications, so their performance improvement with respect to the reduction of manufacturing costs by using less material or with respect to the reduction of operating costs by reducing energy losses is of great technical, economical, and, not least, of ecological importance.

The concept of VG was first introduced in order to improve heat transfer with a relatively minor increase in pressure losses [7, 14-17]. Four basic configurations of vortex generators (VG) are widely discussed in the open literature: delta wings (DW), rectangular wings (RW), delta-winglet pair (DWP), and rectangular winglet pair (RWP) [Figure 2.4]. When the trailing edge is attached to the plate, the VG is a wing, when the chord length is attached to the plate; it is called a winglet [7]. Other shapes of VG may also be found in recent papers like trapezoidal VG in the high efficiency vortex (HEV) static mixer [18-21]. There are other geometries for the VG, Zhou and Feng [22] studied the heat transfer enhancement due to linear and curved VG having a punched hole on them, whereas Wang et al. [23] investigated the semi dimple VG.

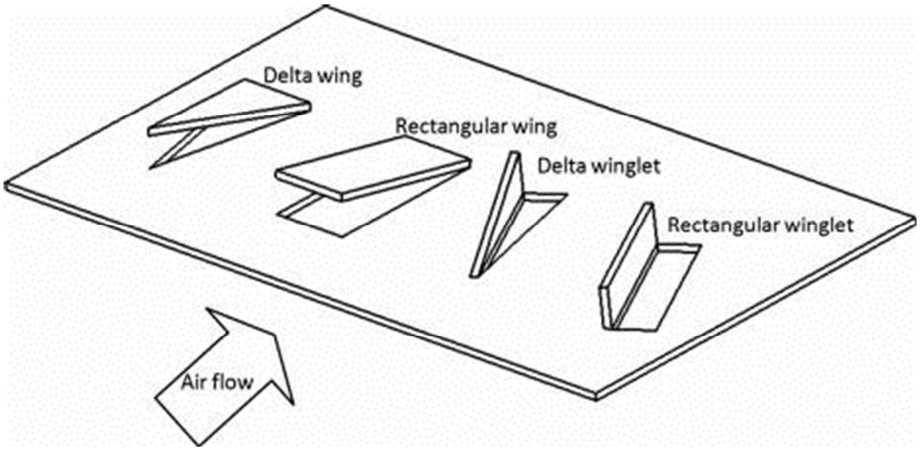

Figure 2.4: Vortex Generators [17]

There are two major types of vortices generated by VG: transverse vortices (TV) and longitudinal vortices (LV). Transverse vortices are mainly recirculation regions in the wake of the VG and affect unfavorably the heat transfer locally in that region. These vortices may induce local overheated regions which may be critical in case of exothermal chemical reactions for example [19]. Meanwhile, longitudinal vortices positively act upon heat transfer through three mechanisms: developing boundary layers, vortices and flow destabilization. New boundary layers are generated around the surface of the VG, vortices are generated as a result of the VG and flow is less stable due to the reversed flows created because of the VG. LV is 3D swirling motion and persist over a long distance downstream the VG in the flow direction.
Several experimental and numerical investigations were conducted to study the heat transfer enhancement downstream from VG.

Wu and Tao [24,25] studied the influences of main parameters of longitudinal vortex generator (LVG) on the heat transfer enhancement and flow resistance in a rectangular channel. Among the studied parameters are the locations of the LVG in the channel, the geometry and the shape of the LVG. The effects of Reynolds number (from 800 to 3000), the attack angle of vortex generator (15°, 30°, 45°, 60° and 90°) were examined. The numerical results were analyzed from the viewpoint of field synergy principle. It was found that the essence of heat transfer enhancement by longitudinal vortex can be explained very well by the field synergy principle.

Longitudinal vortices (LVs) improve the synergy between velocity and temperature field not only in the region near LVG but also in the large downstream region of longitudinal vortex generator. So LVs enable to enhance the global heat transfer of channel. On the other hand, transverse vortices (TVs) only improve the synergy in the region near VG. So TVs can only enhance the local heat transfer of channel.

2.3.2 Types of vortex generators

There are different categories of Vortex Generators each classified based on its behavior and effect on the flow topology. The following categories are the most common: passive, active and the compound type. In the following sections a detailed literature will be presented for each case.

2.3.3 Passive vortex generator:

Edwards and Alker [26] presented experimental results from a study of cubes and delta winglet vortex generators placed in a fully developed flow (Figure 2.5). Their main interest was the size and the spacing of the cubes and generators.

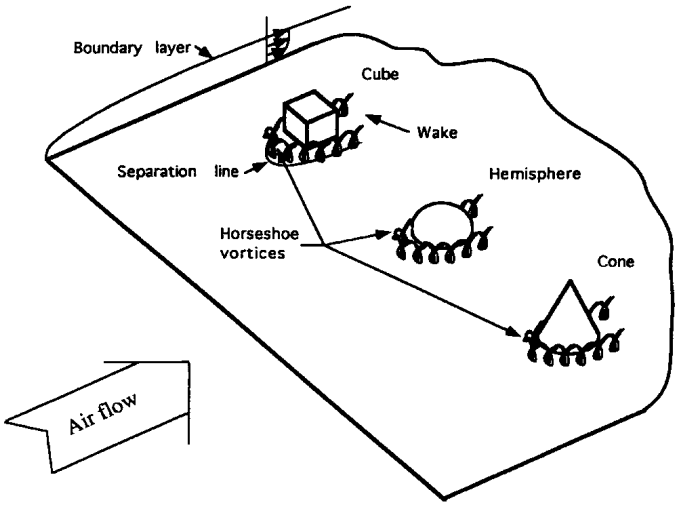

Figure 2.5: Several surface protuberances are shown: cubes, hemispheres, and cones. [26]

Tiggelbeck et al. [27] expanded the previously done studies by adding two pairs of vortices with common inflow (Figure 2. 6). The purpose of the present study is an experimental investigation of flow structure and heat transfer in a channel built by parallel plates with two rows of

longitudinal vortex generators with aligned or staggered arrangement. The comparison of the results of aligned and staggered rows will reveal the changing interaction of the vortex generators and the influence of inhomogeneous oncoming flow.

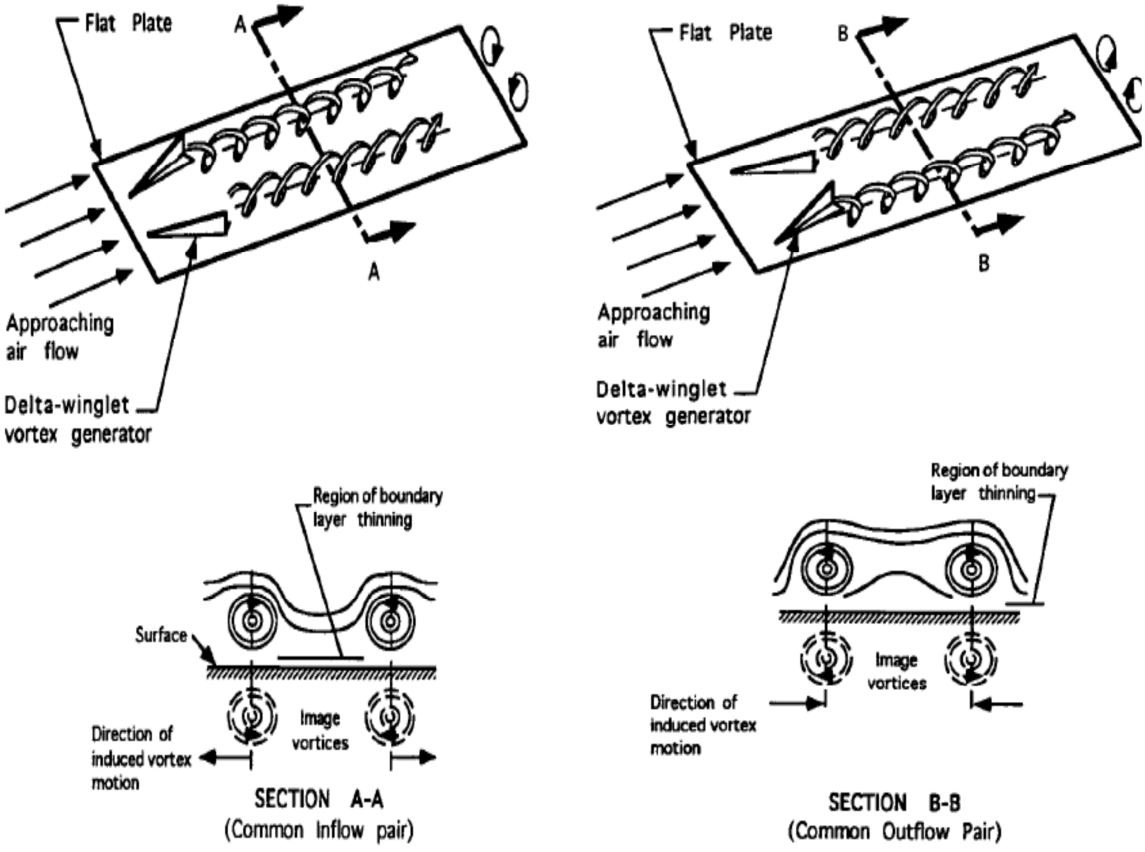

Figure 2. 6: Delta Winglet Vortex Generators [26]

For a deeper study they took the both geometries: up stream pair with common inflow (aligned rows) and downstream pair with common out flow (staggered). For a Re = 4600, they have found out that for the case of aligned geometry [Figure 2. 7] there is an increase in the heat transfer by 60% and an approximate increase of the pressure drop by 145%. On the other hand, the staggered geometry enhanced the heat transfer by 52% and increased the pressure drop by 129%.

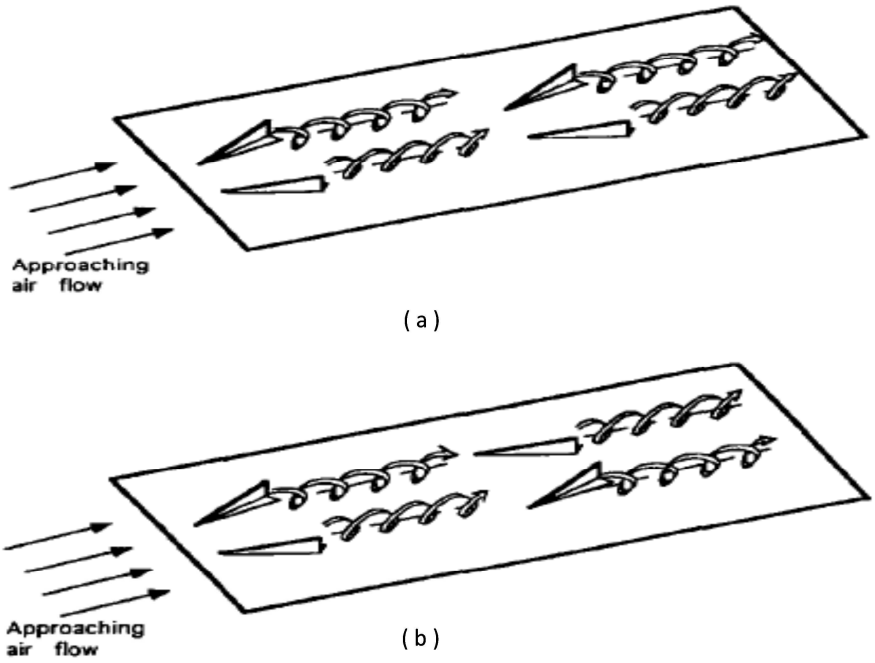

Figure 2. 7: Two delta winglet pairs producing counter rotating vortices: (a) an aligned configuration, (b) a staggered configuration. [26]

In Table 2.1, a summary of the obtained results is represented. For different Reynolds number values the ratio of normalized Nusselt number and that of the drag coefficient for single and double delta winglet row are calculated. The table shows that the ratio is higher for high Reynolds numbers; there the winglets are more effective.

Table 2.1: Ratio of normalized Nusselt number and drag coefficient for single and double delta winglet row [26]

$\left(\frac{Nu}{Nu_0}\right)/\left(\frac{C_f}{C_{f0}}\right)$		
Re	Single	Aligned double row
2000	0.60	0.62
4000	0.64	0.64
6000	0.66	0.67
8000	0.66	0.67

Yakut *et al*. [28] analyzed various kinds of design parameters on heat transfer and flow characteristics of the delta winglet vortex generators. Based on their studies, the main parameter that affects the heat transfer enhancement was the Reynolds number. By increasing the Reynolds number definitely the heat transfer will increase but the increase of the pressure drop should be taken into consideration too. The most effective parameter that plays a major role in the increase of the pressure drop is the winglet height. As the height of the winglet increases the flow will be blocked and as a result of this block the flow will lose its momentum ending at the end of the channel with a drop in its pressure.

Min *et al*. [29] studied the effect of a modified shape of a rectangular shape vortex generator. Their proposal was by cutting the four edges of a rectangular winglet as shown inFigure 2.8: Schematic view of modified vortex generator: (a) common flow down (CFD) wing (b) modified rectangular wing (c) different geometries tabulated [29]. Figure 2.8. For this geometry experimental investigations are done, the vortex generators were mounted in a rectangular channel. The thermal and the flow characteristics were studied and compared to that of the original rectangular vortex generators. Results showed that the modified vortex generators have better flow and heat transfer characteristics, and also a lower friction factors than those of the rectangular pair vortex generators.

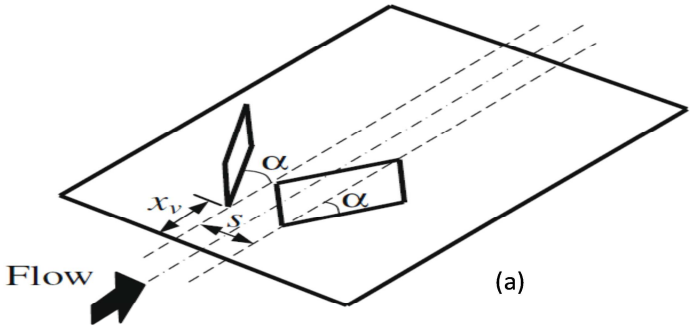

(a)

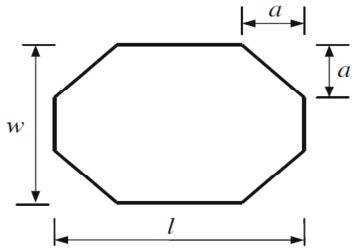

(b)

Type	Length l (mm)	Width W (mm)	Chamfer a (mm)	Thickness t (mm)
RWP	40	30	0	1.2
MRWP1	40	30	10	1.2
MRWP2	47	30	10	1.2
MRWP3	40	35	10	1.2

(c)

Figure 2.8: Schematic view of modified vortex generator: (a) common flow down (CFD) wing (b) modified rectangular wing (c) different geometries tabulated [29].

Figure 2.9 shows the flow characteristics of the four different geometries studied. It can be seen that the values of f have the identical trends with the average Nusselt number. Higher average Nusselt number leads to larger friction factor. MRWPs have lower friction factor in comparison with RWP. The main reason is that the MRWPs area decreases due to the two cutting corners in the main flow, and the flow disturbance by the MRWPs decreases. Furthermore, the friction factor of MRWP1 is significantly lower than that of RWP and the friction factor of the 65° attack angle is lower than that of the 55° attack angle which is different to the other MRWPs. Hence, it can be concluded that all of the three MRWPs have better integrated flow and heat transfer characteristics than those of RWP. It is important to mention that the fluid properties are assumed to be constant and the experimental uncertainties for Re, Nu and ζ are estimated using a random uncertainty technique proposed by Kline and McClintock [30]

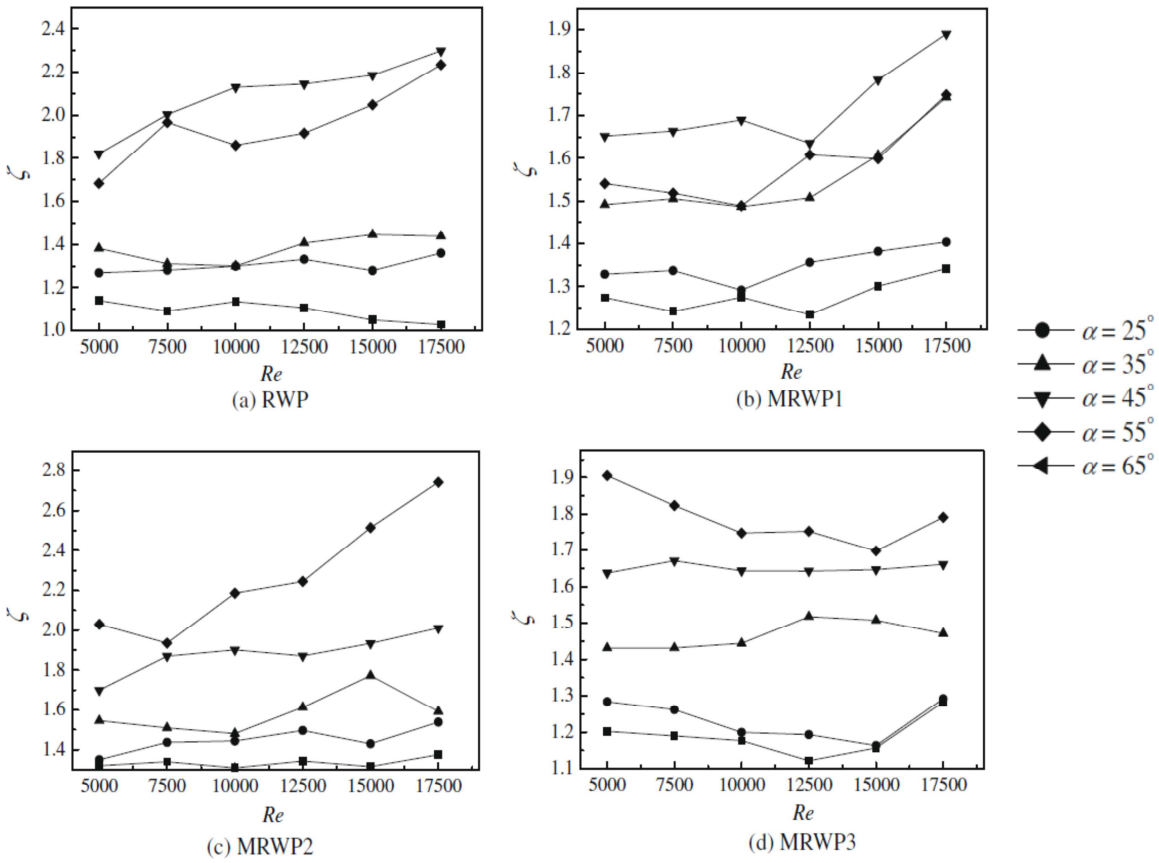

Figure 2.9: Variation of friction factor ratio ζ with respect to Reynolds number for different values of α. [30]

Numerically, Habchi *et al.* [31] performed three dimensional simulations to study the heat transfer in turbulent flows. Where pressure driven longitudinal vortices are generated in a turbulent flow using various configurations of vortex generators inserted in a circular tube. These vortex generators are based on the trapezoidal mixing tabs used in High efficiency vortex static mixer as shown in Figure 2.10.

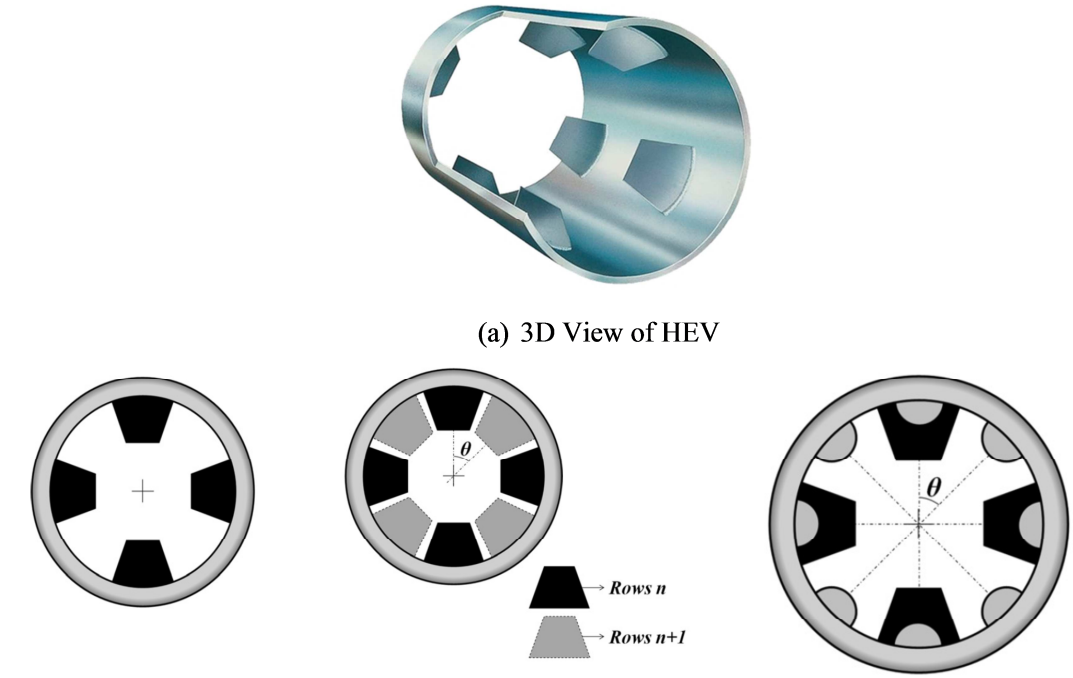

(a) 3D View of HEV

(b) Aligned (Alg)

(c) Alternating (Alt) arrays arrangements

(d) Distribution of the protrusions downstream from the tabs array.

Figure 2.10: Three-dimensional view of the HEV mixer and front view of the different configurations [31]

As an outcome of their study, the effect of the protrusion is clearly highlighted compared to that of without the protrusions. As shown Figure 2.11, the Nusselt number at the leading edge of the protrusion is 130% higher than that of the aligned –inverse flow without protrusions.

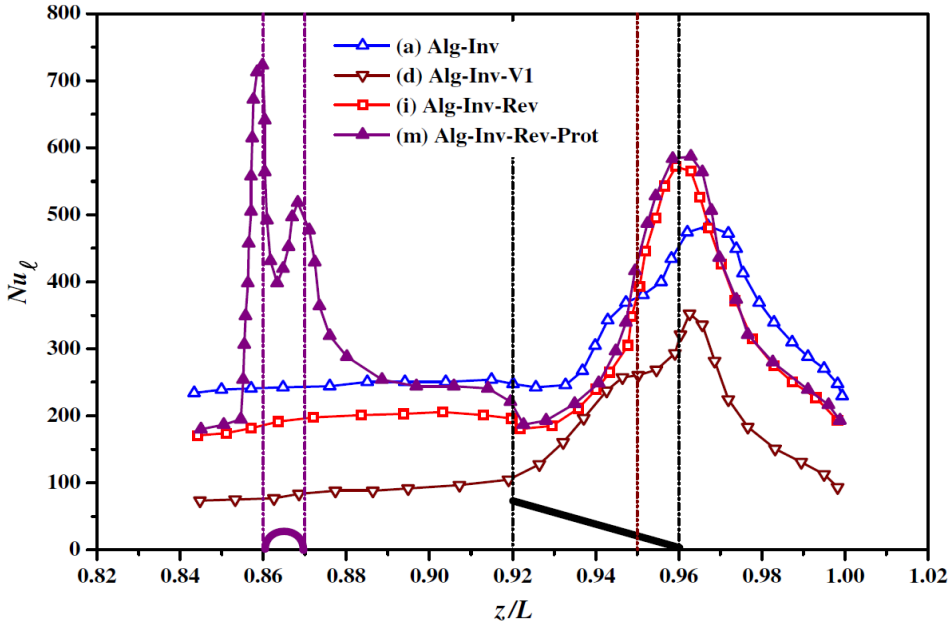

Figure 2.11: Longitudinal variation of the Nusselt number for Re = 15000 [30].

Sanders and Thole [32] tested the effect of attack angle, aspect ratio, direction and the shape of a winglet vortex generator in a laminar regime flow. Based on their studies, the best heat transfer enhancement was using the rectangular winglet pair vortex generators. For Reynolds numbers of 230, 615 and 1016 the heat transfer enhancement percentage was 3%, 36% and 38% respectively. Three different orientations and directions were tested as represented in Figure 2.12: winglet vortex generators all aimed toward the wall of (VG-F), winglets with alternating direction and orientation (VG-F/B) and winglet only in the backward orientation but alternating in direction (VG-B). For every configuration the average heat transfer was studied. For the case of VG-F the average heat transfer augmentations were very low. When the winglet direction and orientation were alternated on every other louver, results were significantly improved with a maximum increase of 25%. When all the winglets were placed in VG-B with alternating direction, results improved further reaching to a value of 33%.

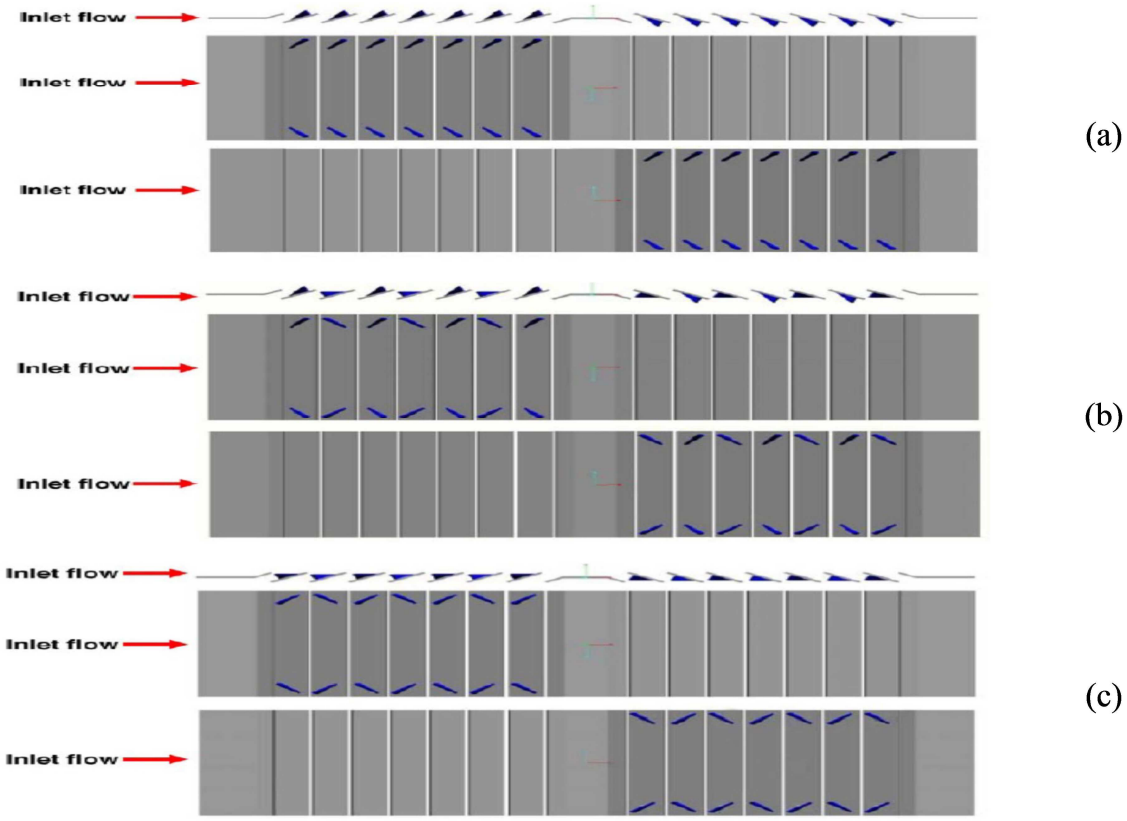

Figure 2.12: Side, top, bottom view of VG: (a) VG-F winglets all aimed toward the wall; (b) VG-F/b alternating wings; (c) VG-B winglets with alternating direction [32]

2.3.4 Active vortex generators

As in other active heat transfer enhancement methods, the advantages of active secondary flow methods are associated with control. Active vortex generation affords control over the heat transfer and pressure drop behavior. When there is a demand for heat transfer performance, vortices are introduced, along with the expense of the power to produce them and the added pressure drop. When the demand is less, the vortex generation will fade and pressure drop and the power consumption will be reduced too.

There are different methods to achieve this control; there has been very little work in the domain of active vortex generators due to the high cost. There are three possible ways to actively

introduce a secondary flow in the form of a longitudinal vortex: Skewed and pitched wall jets [33, 34], electro hydrodynamics (EHD) [35-37], and acoustic excitation [38-42].

Another method used as active method for enhancement of heat transfer is use of jet in between fluid flow. It uses principle that increase in projection of fluid at high velocity increases heat transfer coefficient. Jets are used in many industrial applications thermal control of high flux devices such as electronic devices, gas turbines, internal combustions engines.

Figure 2.13 represent the single steady impinging jet where the different zones are indicated. Zone 1 represents the flow development region. This zone is made up of free jet region and a core region. The region core is where the velocity is approximately equal to the nozzle exit bulk velocity. Zone 2 represents the fully developed region, in this region the axial jet velocity is reduced as the distance from the nozzle increases. Zone 3 represents the location at the rear of the wall where the static pressure increases and there is a sharp decrease in the axial velocity. Finally Zone 4 represents the wall jet region where there is an increase in the transverse velocity reaching to its maximum value.

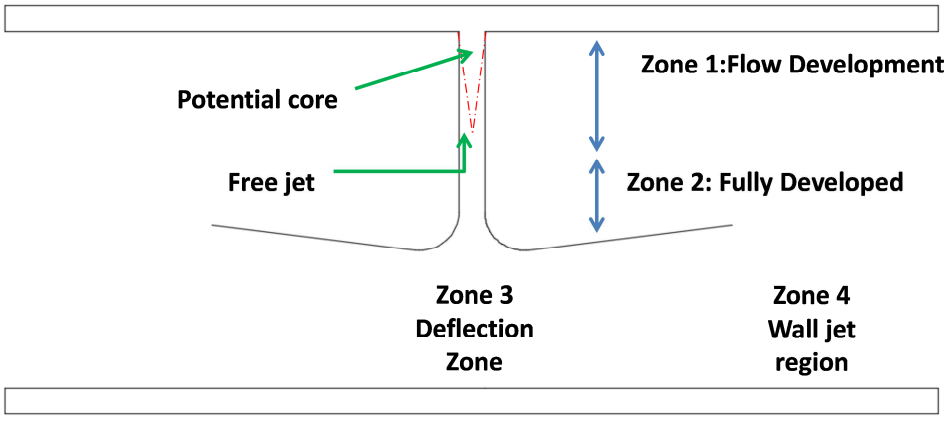

Figure 2.13: Representation of different flow zones in an impinging jet [33, 34]

Figure 2.14 represents the Jet-induced vortices actively controlled. As a result of the injected air into the system, the flow is being agitated and longitudinal vortices are generated. Due to these vortices that are developed along the outlet of the channel the heat transfer is enhanced.

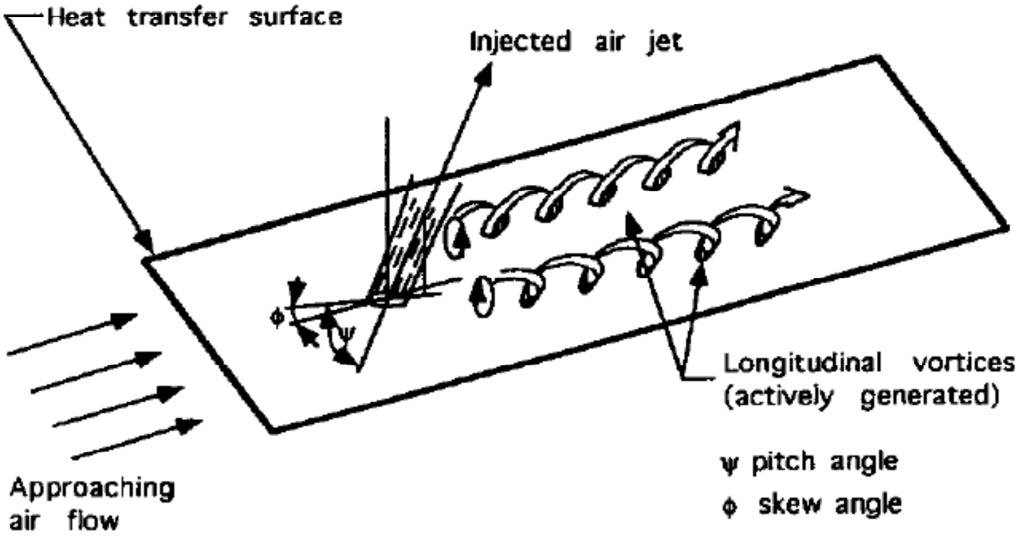

Figure 2.14: Jet-induced vortices actively controlled. [31, 32]

On the other hand, Electro hydrodynamic heat transfer enhancement is a technique using high voltage and current being applied to the fluid flow. One of the main aims of this technique is to convert electrical energy into kinetic energy. The mechanism of EHD-enhanced heat transfer is attributed to the secondary flow issued from the emitting electrode to the collecting plate. This induced secondary flow serves as a corona jet adding momentum to the bulk flow and disrupting the thermal boundary layer on the heated wall, and therefore causes a substantially increase in heat transfer coefficient. [43-46]. This method is usually efficient for cases where the material has electrical properties. Figure 2.15 represents the schematic diagram of a case where two electrodes are added in the flow regime and due to the induced electricity vortices are generated in the flow leading to an enhancement in the heat transfer. [33-34]

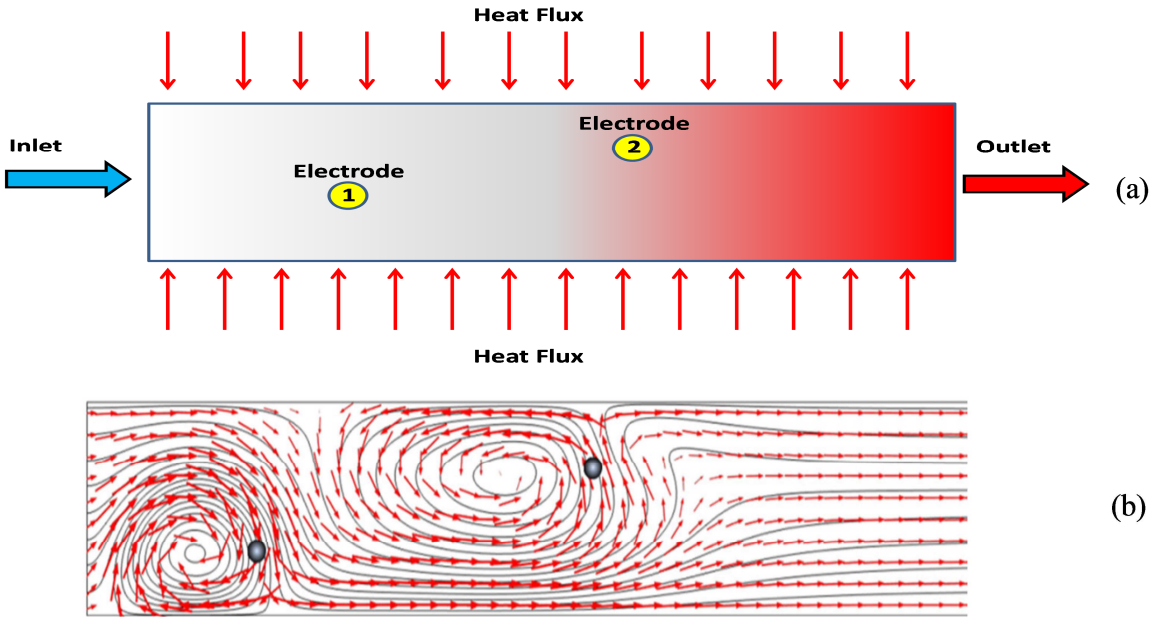

Figure 2.15: Electro hydrodynamic heat transfer technique (a) Schematic diagram, (b) Flow field [35-37]

Another method of an active method is the acoustic excitation, Figure 2.16 represents an acoustically exciting an impinging air jet to enhance the cooling capacity. Where by using acoustic speaker the supply air entering the nozzle will be excited to live the chamber because of this acoustic waves applied to the air, the cooling of the heated plate will be enhanced. [42]

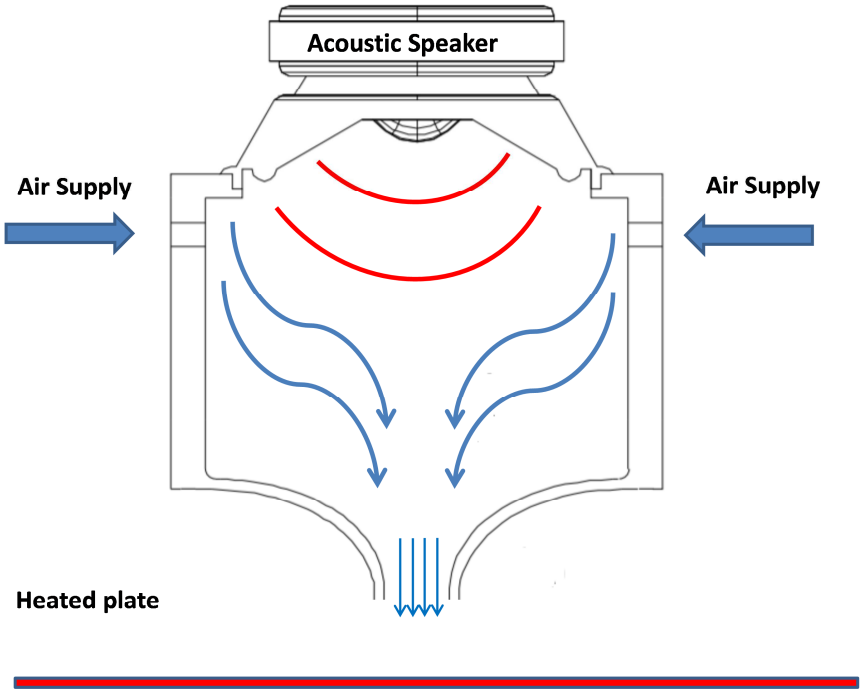

Figure 2.16: The schematic diagram of the acoustic excitation technique [42]

2.3.5 Auto adaptive vortex generators

All the above mentioned techniques aim to generate a secondary flow in order to enhance the heat transfer in a heat exchanger using a static vortex generator. The main objective of this study is to design a vortex generator that under goes deflection by modifying the angle of the VG.

Recent investigations done by Aris et al. [47, 48], explored the development of adaptive heat transfer devices manufactured from shape memory alloys for the cooling of an exposed heated surface. Further investigations and experiment were carried out to determine the heat transfer enhancement and flow pressure losses due to the presence of adaptive VG manufactured from shape memory alloy, on a heated rectangular channel surface. Delta wings were chosen as the adaptive VG design.

Shape memory alloys are commercially available in the form of thin sheets of various sizes. The fabricated samples were later two-way trained; using the martensite deformation technique

recommended by Lahoz et al [49], between high and low temperature set points as shown in Figure 2.17.

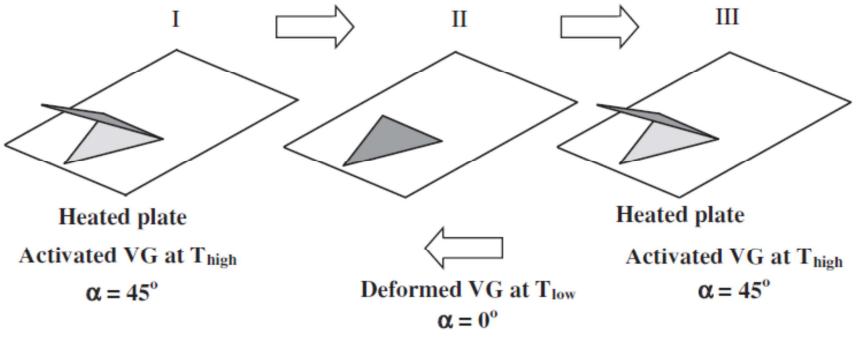

Figure 2.17: Thermal training: cycle for two ways shape memory affect between high and low temperature set points. [49]

The experimental work done to investigate the heat transfer enhancement due to the adaptive delta wing VG in a small air flow of a test section is represented in Figure 2.18. All the sensors are represented in the figure to read the temperature values along the experiment.

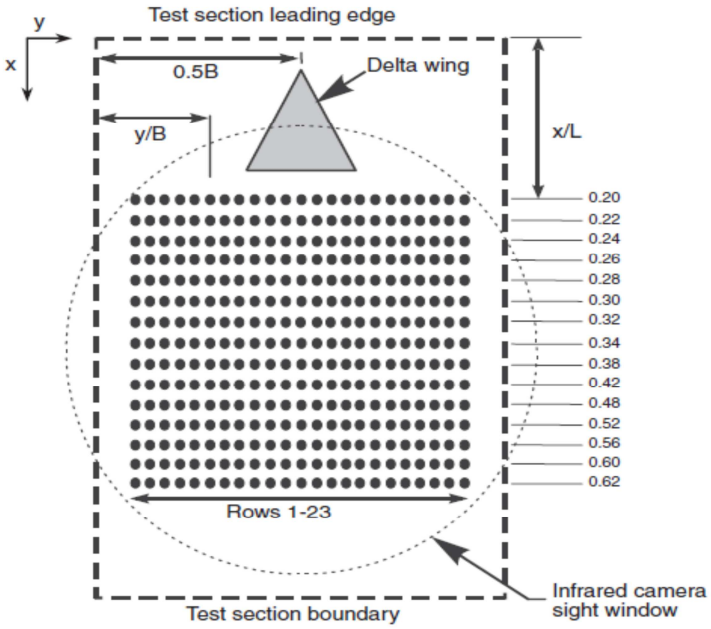

Figure 2.18: Temperature measurements on the test surface. [49]

As the vortex generators were in their adaptive position, the maximum heat transfer improvement was 90% along the downstream direction. On the other hand, when the wing was activated the pressure losses were increased by 7%. Both the heat transfers and the pressure loss results from the experiment have demonstrated the ability of adaptive vortex generators as heat transfer enhancers.

A comparison of the average heat transfer at each streamwise location for the VG pair and the single VG arrangement is shown in Figure 2.19. The average heat transfer enhancement, $Nu_{avg}/Nu_{avg,0}$ at Re =3721, for the single VG and that of the VG pair arrangements were found to be 17% and 133% respectively. The advantage of having adaptive vortex generators is their ability to maintain a low flow pressure loss when they are deactivated, taking advantage of the high angles of attack only when it is necessary to enhance cooling at high temperatures.

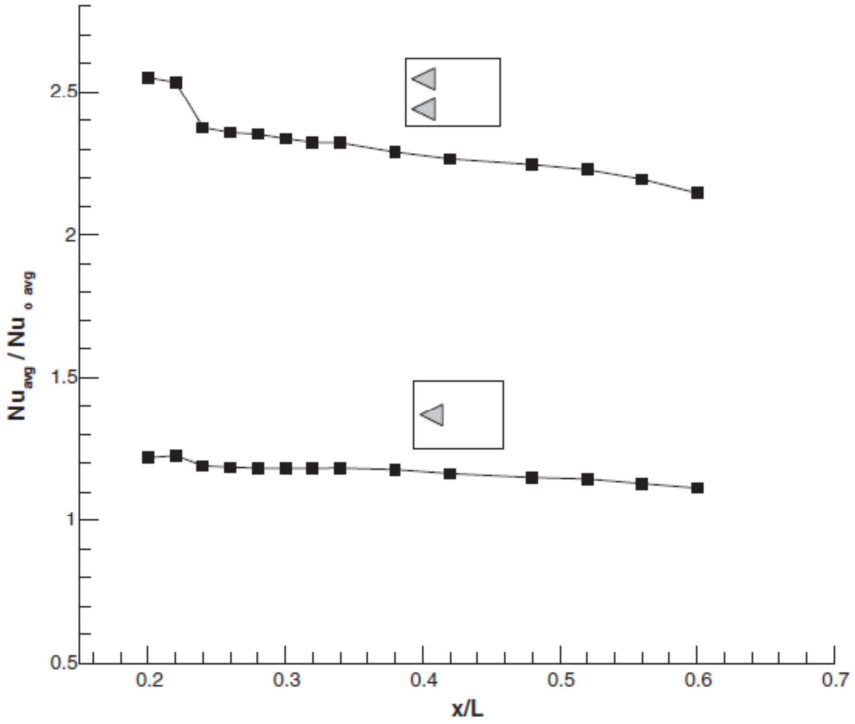

Figure 2.19: Span wise average Nusselt number for both single VG and a pair VG. [49]

Zheng et al. [50], studied the effect of the flexible VG and their influence on the generated vortices. For Re = 2524, three different materials have been studied having the following modulus of elasticities, E = 0.40 MPa, 1 MPa and 4 MPa are considered with the same density of 125 kg/m3. Different motions cause various vortex generating processes. Vortices location and strength can be evaluated with the vorticity field. Figure 2.20 shows the vorticity. In all the conditions, a counterclockwise vortex continuously generates at the tip of agitator while a clockwise vortex generates between it and the bottom boundary. Then, this pair of vortices transfers to the downstream direction. With the same contour legend range, we can find vortices in the conditions with E = 0.40 MPa and 1 MPa are stronger than the other two cases.

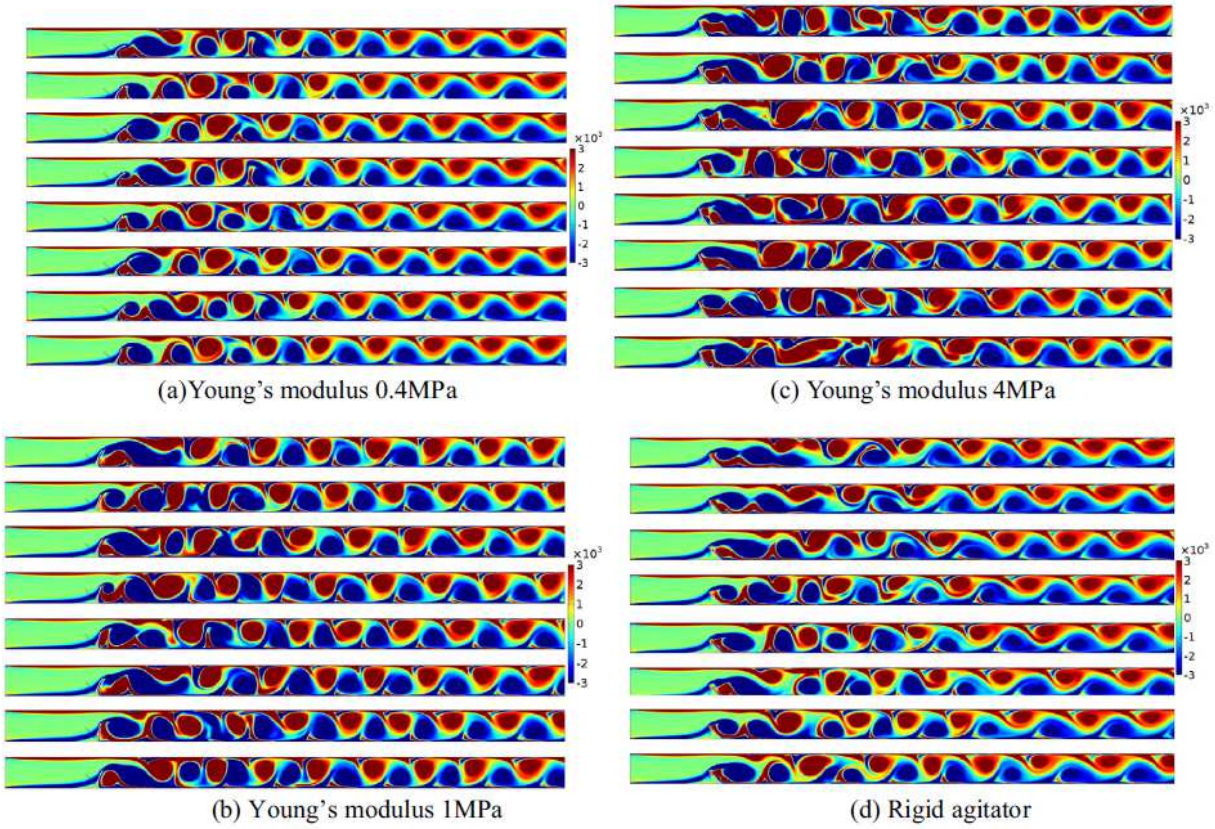

Figure 2.20: Vorticity field in test case for Re=2524. [50]

Figure 2.21 shows the local rejected heat comparison between instantaneous simulation result and corresponding steady mode for different vortex generators. Several peaks exist in the instantaneous simulation results where the vortices locate. These peaks will change locations as

the vortices transfer to downstream direction. On the other hand, the local rejected heat will not change with time in the steady mode. Table 2.2 shows the average rejected heat comparison between simulation and corresponding steady mode for different vortex generators. We can find that the results from steady mode are very close to the average rejected heat calculated from simulation directly. In the meantime, better performance case has higher rejected heat in steady mode. It is necessary to point out the results from steady mode are all lower those from instantaneous simulation results. [50]

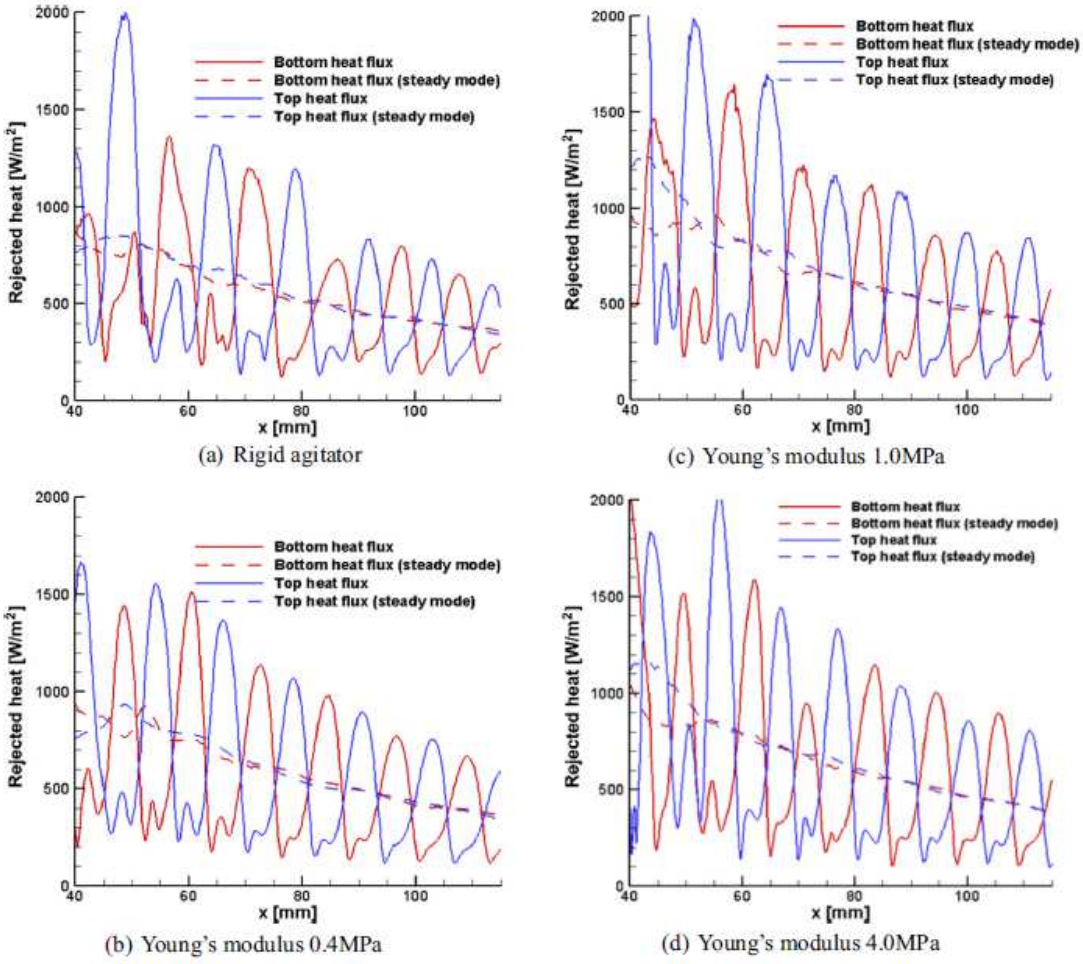

Figure 2.21: Loc al rejected heat comparison between instantaneous simulation result and corresponding steady mode for different vortex generators [50]

Table 2.2: Average rejected heat comparison between simulation and corresponding steady mode for different vortex generators. [50]

	Average rejected heat from steady mode (W/m^2)	Average rejected heat from simulation (W/m^2)
Rigid agitator	558	581
Young's modulus 0.4 MPa	588	618
Young's modulus 1.0 MPa	660	676
Young's modulus 4.0 MPa	641	651

2.4 Conclusions

The presence of a vortex generator in all the above-mentioned methods and techniques is found to be crucial and effective in the heat transfer performance of any heat exchanger. Weather it is a passive, active or even auto adapting vortex generators, their usage is being developed in the industry and engineering applications starting from the large heat exchangers to even on micro-electric chips and their cooling systems.

After analyzing the existing work, it is obvious that there is a wide study in the concept of the static VG and their influence in heat exchangers. Also, different geometries are studied in various range of Reynold's numbers. However, the concept of the flexible VG is under development and study. Until now all the flexible VG that are investigated have nonrealistic modulus of elasticity. Having low values of modulus of elasticity will help to increase the deflection of the VG and enhance the mixing, but on the other hand it will affect negatively on the stability of the VG. The main concern of this study is to have a real material with acceptable value of modulus of elasticity so that there will not be any physical failures of the VG. To do so, the strategy adopted is to start with static vortex generators by studying the local and global effect on the flow topology and the heat transfer, after which the pressure driven auto adaptive vortex generator will be demonstrated and studied.

To be able to build solid and coherent steps in the studied parameters, it was crucial to start with a static VG and perform different case studies with different angle of attacks. By doing so, the effect of the angle is mainly studied and its influence on the thermal enhancement is highlighted. Having in mind that the final target of the thesis is design a pressure driven auto adaptive VG made of a real material with real mechanical and physical properties.

In chapter 4 and 5, rectangular pair winglet vortex generators and rectangular wing vortex generators are studied respectively with different values of Reynolds numbers. For both cases the global and local parameters are studied for different angle of attacks. As a deeper study of the auto adaptive VG, chapter 6 contains a case study of rectangular wing vortex generator which is auto adaptive to the fluid flow. Validations are done for both 2D and 3D simulations with experimental results. Chapter 7 contains a conclusion of the main objectives proposed and since the domain of auto adaptive VG is newly concerned some suggestions and recommendations are done for a various study.

CHAPTER 3

Numerical modeling

The present work is carried out to evaluate the performance of the vortex generators (VG), used to enhance the heat transfer in heat exchangers. Different cases of geometries are studied, starting with a rectangular winglet pair VG (RWPVG) located in a parallel plate channel, a rectangular wing VG (RWVG) located on the bottom wall of a channel and finally an elastic VG located in a rectangular duct.

The first part of this chapter will cover the governing equations and a brief definition for the parameters of static vortex generator simulations using STAR-CCM+ in a laminar flow regime. The second part will be discussing the auto adaptive vortex generators, where a fluid solid interaction (FSI) multi physics simulations are carried out using ANSYS 15.0 for the case of fluid solid interaction in a turbulent regime.

To perform fluid solid interaction simulations with large deformations, ANSYS15.0 is used since STAR-CCM+ v8.04 is designed to run fluid solid interaction simulations with small deformation.

3.1 Flow, heat and turbulence modeling (static VGs)

3.1.1 Laminar flow governing equations

For the two cases of static vortex generators (RWPVG and RWVG), the flow field is governed by three-dimensional (3D) steady-state continuity and momentum equations. The fluid is considered to be incompressible Newtonian with constant properties. The flow is considered as to laminar flow and the governing equations can be expressed as follows:

Continuity equation: $$\nabla . \vec{u} = 0 \tag{3.1}$$

Momentum equation: $$\rho(\vec{u} . \nabla)\vec{u} = -\nabla p + \mu \nabla^2 \vec{u} \tag{3.2}$$

Energy equation: $$\rho C_p \nabla.(\vec{u}T) = k_f \nabla.(\nabla T) \quad (3.3)$$

where $\vec{u}$ is the velocity vector, C_p is the specific heat at constant pressure, p the pressure, μ the fluid viscosity, T the temperature, ρ the density of the fluid and k_f the fluid thermal conductivity.

3.1.2 Star CCM+ numerical procedure

The computational fluid dynamics (CFD) software used to compute the Navier-Stokes and energy equations is STAR-CCM+ v. 8.04 [51], which is based on the finite volume method. The segregated flow solver is used when the equations are computed in a segregated manner, i.e. one for each component of velocity, and one for pressure. The coupling between the momentum and continuity equations is achieved with a predictor-corrector approach. The pressure-velocity coupling is performed with the SIMPLE algorithm. The convective terms in the governing equations for momentum and energy are discretized with the second-order up-wind scheme and second-order central scheme for diffusion terms. The algebraic multi-grid (AMG) linear solver is used to solve the velocity, pressure and temperature with Gauss-Seidel relaxation scheme.

The residual value 10^{-14} [52] is considered as the convergence criterion for the solutions of the flow and the energy equations. Beyond this value, the equations are solved with no significant changes in the values for velocity, temperature also the heat balance and the mass flow balance are maintained.

One of the main goals of this study is to find out a real physical material with known properties and relatively acceptable dimensions. To come out with a conclusion, the study started with a laminar flow with low Reynolds number (Re = 456) and then doubled the Reynolds number for both cases the tilt deflection angle of the vortex generator was negligible. In order to have a higher deflection tilt angle the regime was changed from laminar to turbulent.

3.1.3 Turbulent flow governing equations

By changing the regime from laminar to turbulent, the momentum equation will be modified as represented in Eq. (3.4)

Turbulent regime momentum equation:

$$\rho \frac{\partial}{\partial x_i}(u_i u_k) = -\frac{\partial P}{\partial x_k} + \frac{\partial}{\partial x_i}\left(\mu(\frac{\partial u_i}{\partial x_k} + \frac{\partial u_k}{\partial x_i} - \frac{2}{3}\delta_{ik}\frac{\partial u_j}{\partial x_j}\right) + \frac{\partial}{\partial x_i}(-\rho\overline{u_i' u_k'}) \quad (3.4)$$

The last term in the right in Eq. (3.4) is the Reynolds stress tensor resulting from the averaging procedure of the non-linear convective terms in the momentum equations.

The standard k- ω model is based on the Wilcox k- ω [53], which incorporates modifications for low Reynolds number effects, compressibility, and shear flow spreading. The Wilcox model predicts free shear flow spreading rates that are in close agreement with measurements for far wakes, mixing layers, and plane, it is applicable to wall bounded flows and free shear flows. A variation of the standard k- ω called the SST k- ω (shear stress transport) which was developed by Menter [53] to effectively blend the robust and accurate formulation of k- ω model in the near wall region with the free stream independence. The SST k- ω model is similar to the standard k- ω model, but includes the following modifications:

- The SST model incorporates a damped cross diffusion derivative term in the ω equation.
- The definition of the turbulent viscosity is modified to account for the transport of the turbulent shear stress.
- The modeling constants are different.

As the k-ω model has been modified over the years, production terms have been added to both the k and ω equations, which have improved the accuracy of the model for predicting free shear flows. The following version of the k − ω model is presented

$$\nu_T = {}^{k}/_{w} \quad (3.5)$$

The turbulence kinetic energy and the dissipation ratio ω are obtained from the following kinetic energy equation (Eq. (3.6)) and the dissipation equation (Eq. (3.7)).

$$\frac{\partial k}{\partial t} + U_j \frac{\partial k}{\partial x_j} = \tau_{ij} \frac{\partial U_i}{\partial x_j} - \beta^* k\omega + \frac{\partial}{\partial x_j}\left[(\nu + \sigma^* \nu_T)\frac{\partial k}{\partial x_j}\right] \quad (3.6)$$

$$\frac{\partial \omega}{\partial t} + U_j \frac{\partial \omega}{\partial x_j} = \alpha \frac{\omega}{k} \tau_{ij} \frac{\partial U_i}{\partial x_j} - \beta \omega^2 + \frac{\partial}{\partial x_j}\left[(\nu + \sigma \nu_T)\frac{\partial \omega}{\partial x_j}\right] \tag{3.7}$$

Where the closure coefficient and relations are represented in the following equation:

$$\alpha = \frac{13}{25} \; ; \beta = \beta_o f_\beta \; ; \beta^* = \beta_o^* f_{\beta^*} \; ; \; \sigma = \frac{1}{2} \; ; \; \sigma^* = \frac{1}{2} \tag{3.8}$$

$$\beta_o = \frac{9}{125} \; ; \; f_\beta = \frac{1 + 70X_\omega}{1 + 80X_\omega} \; ; \; X_\omega = \left|\frac{\Omega_{ij}\Omega_{jk}\Omega_{ki}}{(\beta_o^* \omega)^3}\right| \tag{3.9}$$

$$\beta_o^* = \frac{9}{100} \; ; \; f_{\beta^*} = \begin{cases} 1 & X_k \leq 0 \\ \frac{1+680X_k^2}{1+400X_k^2} & X_k > 0 \end{cases}, \; X_k = \frac{1}{\omega^3}\frac{\partial k}{\partial x_j}\frac{\partial \omega}{\partial x_j} \tag{3.10}$$

$$\epsilon = \beta^* \omega k \; ; \; l = \sqrt{k}/\omega \tag{3.11}$$

3.2 Structural Solver

3.2.1 Presentation

The structural solver is designed with a Lagrangian frame of reference, which means that the mesh velocity is equal to the material velocity $u_m = u$, thus the momentum equation becomes:

$$\rho_s \frac{\partial \boldsymbol{d_s}^2}{\partial t^2} = \nabla . \sigma + \rho_s \boldsymbol{b} \tag{3.12}$$

Where $\boldsymbol{d_s}$ is the structural displacement and **s** subscript represents the structural domain.

In the presented work, all the studied cases the structure undergoes a large deformation, only the relations for the large deformations will be presented. When the strain percentage is above few percent, that deformation cannot be neglected. The applied force on a body will make the body move from one position to another as shown in the “undeformed” and “deformed” positions in Figure 3.1. The position vectors of both configurations are denoted $\boldsymbol{d_x}$ and $\boldsymbol{d_X}$.

$$\boldsymbol{d_s} = \boldsymbol{d_x} - \boldsymbol{d_X} \tag{3.13}$$

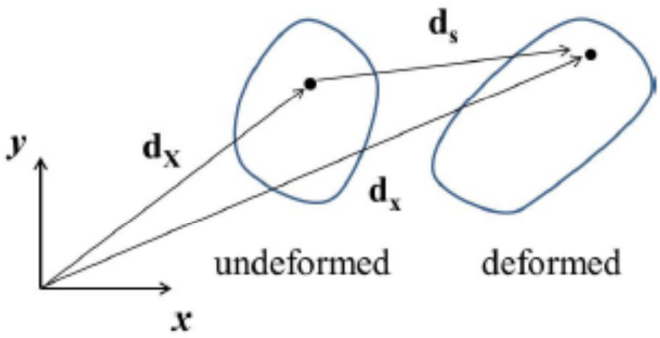

Figure 3.1: Motion of a deforming body [53]

As a result of this, the deformation gradient can be represented as:

$$\boldsymbol{F} = \frac{\partial \boldsymbol{d_x}}{\partial \boldsymbol{d_X}} \tag{3.14}$$

The above equation can be represented also as followed:

$$\boldsymbol{F} = \mathbf{I} + \frac{\partial \boldsymbol{d_x}}{\partial \boldsymbol{d_X}} \tag{3.15}$$

where $\mathbf{I}$ is the identity matrix.

The Green-Lagrange strain, referred usually as the Green Strain, is defined as:

$$\boldsymbol{G} = (\boldsymbol{F}^T \boldsymbol{F} - \mathbf{I}) \tag{3.16}$$

which also can be represented as followed:

$$\boldsymbol{G} = \frac{1}{2} [\nabla \boldsymbol{d_s} + (\nabla \boldsymbol{d_s})^T + \nabla \boldsymbol{d_s}.(\nabla \boldsymbol{d_s})^T] \tag{3.17}$$

To show the nonlinearity of the Green tensor it is compared to its equivalent in small strain linear analysis:

$$\boldsymbol{G} \approx \frac{1}{2}\left[\nabla \boldsymbol{d_s} + (\nabla \boldsymbol{d_s})^{\boldsymbol{T}}\right] \tag{3.18}$$

In order to measure the stress component in a suitable way for large deformation cases, it must be a conjugate of the strain measure. Thus, when interpreting the Cauchy stress σ, it must be transformed in terms of second Piola-Kirchhoff stress tensor Σ by:

$$\sigma = J_F \boldsymbol{F}\, \Sigma \boldsymbol{F^T} \tag{3.19}$$

where J_F is the Jacobian of the deformation gradient:

$$J_F = \det(\boldsymbol{F}) \tag{3.20}$$

The finite element residual equation for large deformation formulation uses nonlinear strain-displacement matrix B_{nl} and the second Piola-Kirchhoff stress tensor Σ by:

$$\boldsymbol{R}(\boldsymbol{d_s}) = \sum_{V}[B_{nl}^{T}\, \Sigma - N^{T} b]\omega J - \sum_{A} N^{T} t^{p} \omega j \tag{3.21}$$

where **R** is the element force residual which represents the imbalance between the external applied forces and the internal element reaction forces, B_{nl} is the non-linear strain displacement matrix, t^p is the applied traction force, ω is the Gauss-point weight for the Gaussian quadrature, J is volume to volume Jacobian between the reference and physical volume elements, j is the face to face Jacobian and N is a shape function matrix that enables interpolation of the nodal values to a location within the element. The non-linear strain is composed of a linear and nonlinear component as:

$$B_{nl} = B_l + B_n \tag{3.22}$$

where the Green tensor **G** can be represented as:

$$G = B_l d_s + \frac{1}{2} B_n d_s \tag{3.23}$$

Furthermore, the global residual **R** is determined by summing the force residual for all the elements using the direct stiffness method [54]:

$$\boldsymbol{R}(\boldsymbol{D_s}) = \sum_{elements} \boldsymbol{R}\,(\boldsymbol{d_s}) \tag{3.24}$$

where $\mathbf{D_s}$ is the global displacement vector. In order to solve the system of equations, a Newton Raphson method is employed by taking an initial guess of solution vector $\boldsymbol{D_s^i}$ for i =0 and a tangent to evaluate the next guess as:

$$\delta \boldsymbol{D_s} = -\left[\frac{d\boldsymbol{R}}{d\boldsymbol{D_s}}\Big|_{D_s^i}\right]^{-1} \boldsymbol{R}(\boldsymbol{D_s^i}) \tag{3.25}$$

Hence, the next guess solution will be in the following form:

$$\boldsymbol{D_S^{i+1}} = \boldsymbol{D_s^i} + \delta \boldsymbol{D_s} \tag{3.26}$$

The iterative procedure continues until the global displacement residual is sufficiently small based on convergence criteria for the norm of **R** to be less than 10^{-5} times the applied load magnitude as used in all the studied configurations.

3.2.2 Dynamic layering

The dynamic layering method allows adding or removing layers of cells adjacent to a deforming zone. Cells are added or removed based on whether the zone is growing or shrinking. This method is applicable for quad, hex and wedge mesh elements and is used for linear and rotational motion. The layer cells adjacent to the moving boundaries (layer *j*) are split or merged with the layers of the cells next to it (layer *i*) as represented in Figure 3.2 based on the height of the cells in layer *j*.

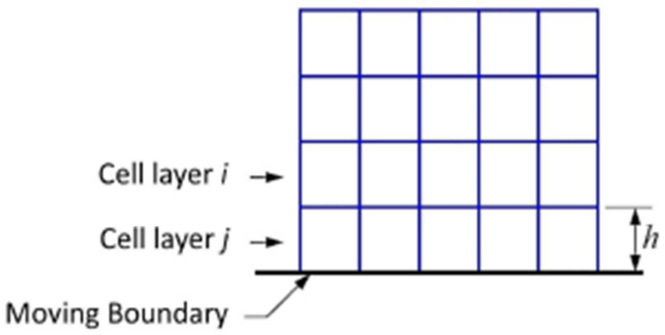

Figure 3.2: Dynamic layering [53].

Splitting and merging of the cell layers is dependent upon the split factor α_s and the collapse factor α_c. If the cells in layer *j* are expanding, splitting will occur if the following condition is satisfied:

$$h > (1 + \alpha_s)h_{ideal} \tag{3.26}$$

where h_{ideal} is the ideal height of the cell and generally is taken to be the same as the as the initial height in the layer near the moving boundary. When this condition is met, the cells are split to create a new layer cell of height equal to h_{ideal}. However, if the cells in layer *j* are being compresses, the cell heights are allowed to decrease until:

$$h < \alpha_c h_{ideal} \tag{3.27}$$

When the above condition is satisfied, the cells in layer j are merged with those in layer i.

3.2.3 Remeshing methods

In order to avoid the divergence problems due to negative volume cells as a result of the large deformation, the mesh solver supports several re-meshing methods. Re-meshing allows then simulating problems with large relative motion of boundaries where the cells and faces are remeshed when skewness or size exceeds specified limits as shown in Figure 3.3. The mesh solver can report negative volume cell if the mesh contains inacceptable elements. The skewness of a cell is usually calculated by the equilateral deviation method [55] as follows:

$$Skewness = \frac{optimal\ cell\ size - actual\ cell\ size}{optimal\ cell\ size} \tag{3.28}$$

If the new cells satisfy he skewness criterion, the mesh is updated with the new cells. In these methods, the number of nodes and connectivity changes as cells/faces are added or deleted.

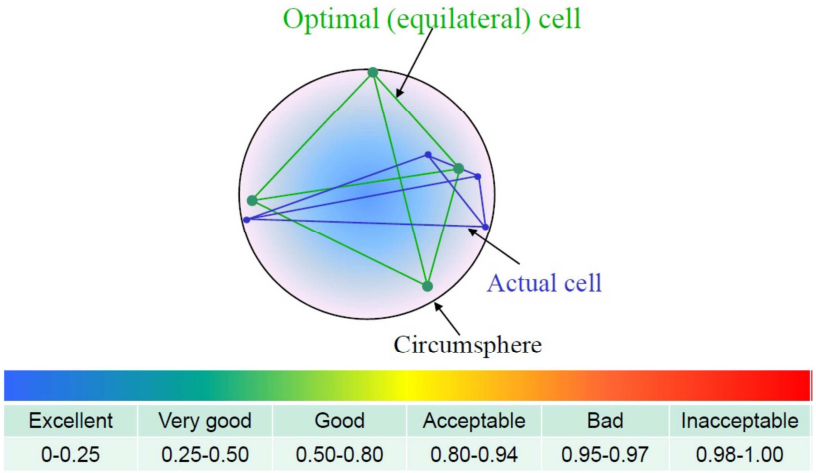

Figure 3.3: Skewness mesh metrics spectrum [55].

The available Remeshing methods in ANSYS Fluent are summarized below according to their supported mesh types:

- Local cell: remesh interior cells (2D and 3D). It only affects triangular and tetrahedral cell types in the mesh.
- Zone remeshing: remesh the complete cell zone if local cell remeshing fails. Usually, the zone remeshing type will be used if skewness is greater than 0.98 after local cell Remeshing.
- Local face: remesh triangular faces on deforming boundaries (only in 3D).
- Region face: remesh faces adjacent to a moving boundary (2D and 3D). It is applied to triangular faces in 2D and tetrahedral faces in 3D and it remeshed the faces based on skewness only.
- 2.5D: remesh prism elements in 3D zones (prisms from extruded triangular elements).

3.3 Fluid Solid Interaction (FSI) Coupling

Fluid-structure interaction problems can be modeled using different approaches mainly divided into partitioned and monolithic [56-60]. Monolithic approaches are considered as strongly coupled since the fluid and structural equations are solved separately and boundary conditions are exchanged between the two solvers at the solid-fluid interface.

Partitioned approaches are divided into one-way (uncoupled) or two-way coupled methods. Depending on the degree of numerical coupling, also the two-way coupling methods are even divided into weakly and strongly coupled as shown in Figure 3.4. The monolithic approach formulates the governing equations for both the fluid and the structure domains in term of the same variables and discretizes the entire domain with the same numerical scheme. The main advantage of using a monolithic approach is that the algorithm of the coupling between the fluid and the solid domains is achieved perfectly. This improves the stability of the numerical methods. However, this method has some negative aspects also:

- The system of algebraic equations obtained after discretization is not linear, this will lead into complex software developments especially for large scale problems.
- The resulting system of equations requires a lot of CPU memory in order to store the simultaneously the unknown variables for both the fluid and the solid domains.
- A common time step is used for all the domains, which may be inefficient especially when different time scales are present [61].
- A single mesh is usually generated for both the fluid and solid domains which create difficulties to provide a high-quality mesh [62].

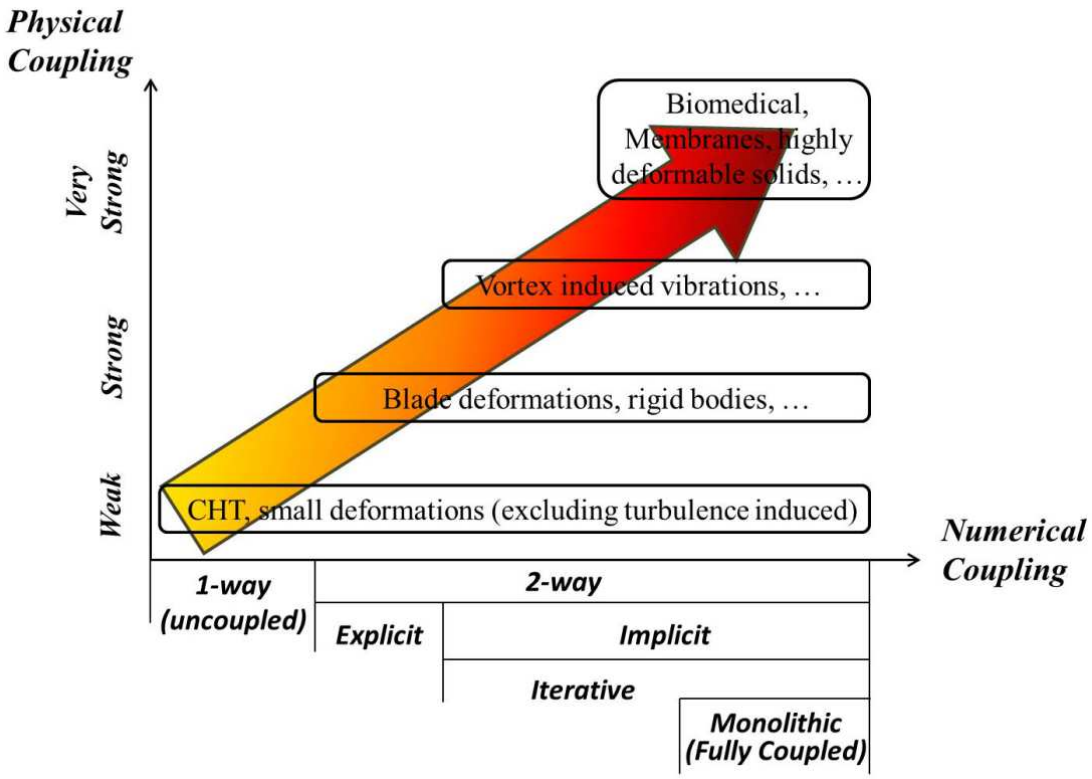

Figure 3.4: Modeling approach of FSI problems [61].

Regardless of whether the solution is one-way or two-way, the partitioned method will approach to separate solutions for the different physical equations. With this approach, each solver can be based on different discretization techniques such as the finite volume method for the fluid solver and the finite element method for the structural solver. At the fluid-solid boundary, information is shared between the two solvers both the fluid and the solid. The exchange of the information within the two is based on the coupling method as either weakly or strongly coupled. For one-way coupling method, a converged solution is obtained for one field, then this solution is considered as a boundary condition for the second field. For a case of fluid solid interaction simulation having a rigid solid structure (metals) moving and a light density fluid (air), because of the motion of the rigid body, the fluid will be affected by this motion. On the other hand, the fluid will not cause any significant forces on the moving body. This kind of problem can be solved using one-way fluid solid interaction problem. The movement of the structure controls that of the fluid without being affected by the fluid.

In Figure 3.5 the one-way fluid solid interaction algorithm is presented. Unfortunately, the fluid solid interaction in our case is mostly concerned by the two-way coupled. If we consider a solid structure having properties as that of polymers, the flow acting on the structure will make it deform. As a result of this deformation the fluid flow will be influenced. The coupling method for these types of problems should be two-way since both fluid and solid are affected from each other.

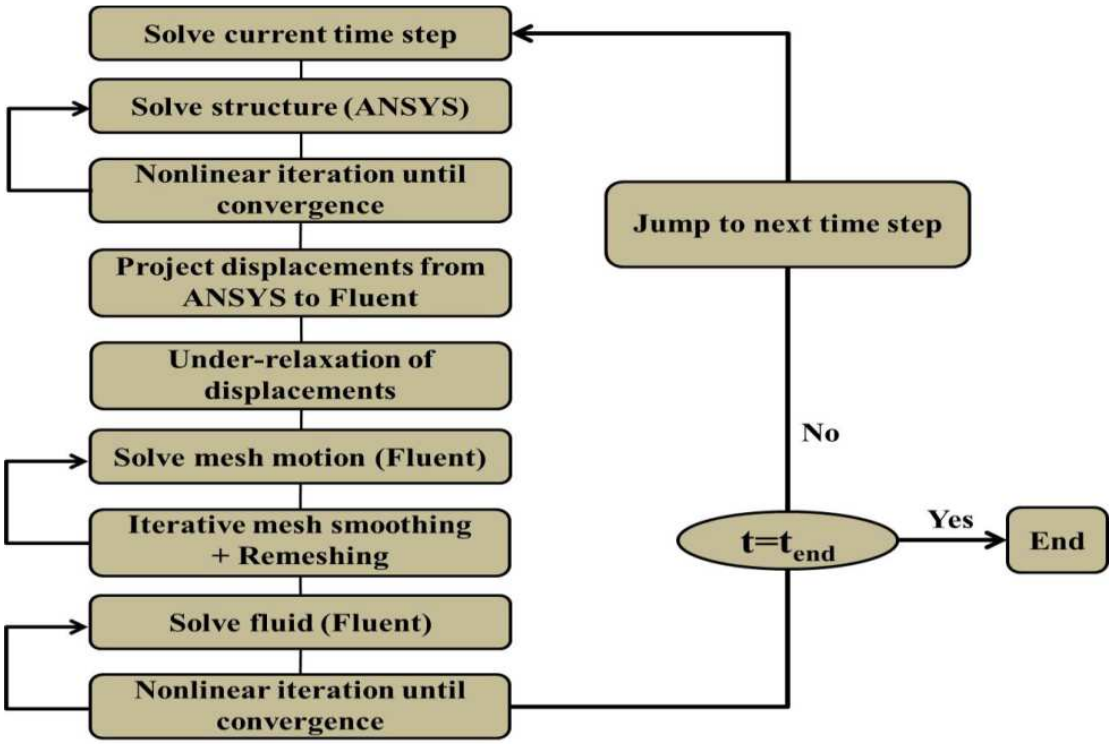

Figure 3.5: One way coupling algorithm of FSI problem [62].

Figure 3.6 shows the algorithm of the two-way fluid solid interaction coupling. During a time step of two way coupling method, the response of the structure to the acting loads represents a displacement of the structural grid nodes in ANSYS mechanical. The displacement of the boundary at the fluid-solid interface is further interpolated to the fluid mesh which will cause its deformation where the appropriate smoothing and remeshing methods are applied to ensure the high quality of the mesh. Finally, inner iterations of the flow solver ANSYS Fluent are

performed until convergence criteria are reached where the convergence solution of the flow field is required to transfer the acting forces on the solid body. Figure (3.6) classifies the two-way coupling algorithm into weekly (explicit) or strongly coupled (implicit) respectively in Figure 3.6 (a) and Figure 3.6 (b).

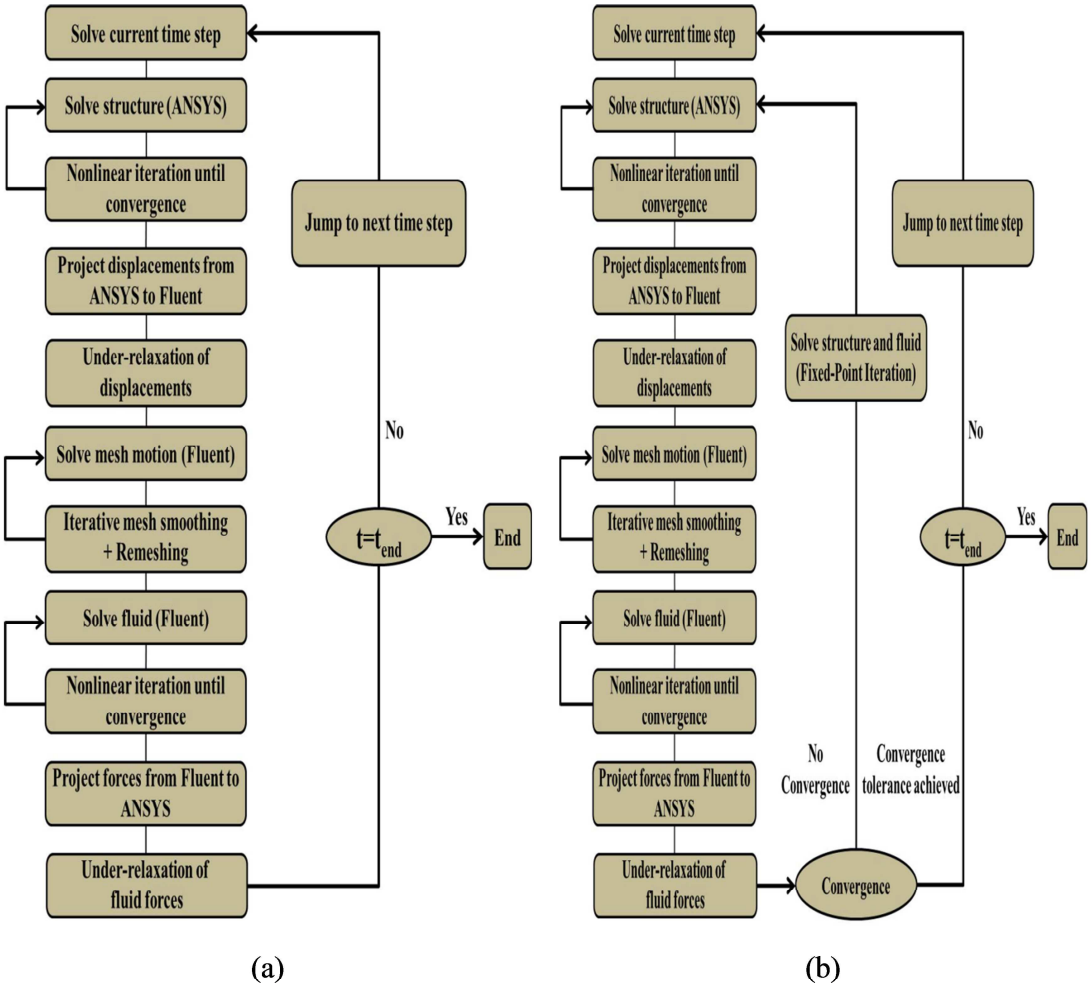

Figure 3.6: Two way coupling algorithm of FSI problem: (a) Weakly coupled and (b) Strongly coupled [62].

In order to have equilibrium in the fluid-solid interface, some restrictions should be taken into consideration. The boundary conditions for displacement **d**, mesh velocity $\boldsymbol{U_s}$ and equilibrium stress **σ** should satisfy the following relations:

$$Skewness = \frac{optimal\ cell\ size - actual\ cell\ size}{optimal\ cell\ size} \tag{3.29}$$

$$\boldsymbol{d_s^{\Gamma}}^{F}/_{S} = \boldsymbol{d_f^{\Gamma}}^{F}/_{S} \tag{3.30}$$

$$\boldsymbol{U}_{\boldsymbol{s}}^{\Gamma}{}^{F}/_{S} = \boldsymbol{U}_{\boldsymbol{f}}^{\Gamma}{}^{F}/_{S} \tag{3.31}$$

$$\boldsymbol{\sigma}_{\boldsymbol{s}}^{\Gamma}{}^{F}/_{S} \,.\boldsymbol{n} = \boldsymbol{\sigma}_{\boldsymbol{f}}^{\Gamma}{}^{F}/_{S} \,.\boldsymbol{n} \tag{3.32}$$

where **n** is the unit normal on the fluid solid interface. The flow chart defining the solution procedure in this study as in Figure 3.6 (b) involves the use of under-relaxation of displacements and forces when projecting them to the destination solver at the interface. The use of under-relaxation in these iterations is mainly to control the amount of the structure's displacement of fluid forces that is projected on either the fluid or solid domain with the aim of improving the convergence. The following equation is applied in order to limit potentially large variations of the target-side data between the two successive coupling iterations:

$$\phi_{Relaxed} = \phi_{Reference} + \omega(\phi_{Raw} - \phi_{Reference}) \tag{3.33}$$

where ω is under-relaxation factor, ϕ_{Relaxed} is the relaxed target-side value, $\phi_{\text{Reference}}$ is the reference target-side value which is the final value obtained from the last coupling iteration. ϕ_{Raw} is the raw value obtained from interpolation of the solution obtained at the current coupling iteration from the source grid node to the target grid node.

3.4 Conclusion

In this chapter, the governing equations for the fluid, solid and mesh motion solvers have been presented. Smoothing capabilities were highlighted where the diffusion-based smoothing is favored in all the fluid solid interaction simulations investigated in this study since it performs and preserves the mesh quality much better when compared to other mesh smoothing methods. Alongside with the smoothing, remeshing is applied also to avoid negative cell volumes when large displacement motions are studied which is important to our objective since we deal with highly deformable elastic bodies. Moreover, the numerical coupling used in all the simulations is considered two-way with strong coupling at the fluid-structure interface which is necessary to

resolve the feedback between the fluid flow and the structural deformations thus maintaining numerical stability.

CHAPTER 4

Rectangular Winglet Pair Vortex Generator

(The study of this chapter is published as an article "Effect of rectangular winglet pair roll angle on the heat transfer enhancement in laminar channel flow", in International Journal of Thermal Sciences in 2017.)

4.1 Introduction

In the open literature, most of the studies focus on the effect of the VG aspect ratio, its attack angle and flow rate on the heat transfer enhancement and pressure losses. To our knowledge, there is no study detailing the effect of the roll-angle β on the heat transfer process. Thus, in the present study, numerical investigation is performed on the effect of the roll-angle of RWP on the thermal performance in laminar viscous flow between two parallel plates.

Different values of roll-angle β in the range [20°–90°] are considered, while maintaining constant angle of attack (α=30°) strikethrough. This value for α is proposed based on the results obtained by the experimental study of the Tiggelbeck *et al*. [26].

Local and global parameters of the Nusselt number and the friction coefficient are studied. In addition, the position and strength of the vortices being created in the duct are studied highlighting their effect on the heat transfer performance.

The roll angle is also extremely interesting for the concept of auto-adaptive. Depending on the variation of the dynamic pressure with the velocity of the flow which will be exerted on the face of the VGs, the roll angle will vary thereby influencing the performance of the exchanger.

4.2 Geometry, computational domain and boundary conditions

The whole geometry of our study consists of one row of RWP placed in between two parallel plates as seen in Figure 4.7 (a).

The computational domain consists of a rectangular duct of height $H = 38.6$ mm, width W=1.6H and a length L=13H in which a RWP is inserted near the entrance on the bottom wall at

a distance R=1.55H away from the inlet as shown in Figure 4.7. The origin of the coordinate system is located on the computational domain as shown in Figure 4.7 (c). As stated in the introduction, the attack angle α, which is the angle between the VG reference line and the incoming flow in the Z direction, is fixed to 30° (see Figure 4.7(b)) based on the experimental results [26], while the roll-angle β which is the angle between the plane of the VG measured with respect to the bottom wall and it varies between 20° and 90° (see Figure 4.7(c)). The rest of the dimensions are given in Table 4.1 in term of the channel height H.

Taking into account that both sides are considered to be symmetry relative to the plan (x, z), only half of the domain is computed. Flow and heat transfer simulations are carried out for Reynolds numbers 456 and 911, with uniform inlet temperature set to $T_{in} = 293\ K$ and wall surface temperature $T_w = 333\ K$ set for all the both bottom and top walls. In addition, the temperature of the VG is set to be as $T_w = 333\ K$.

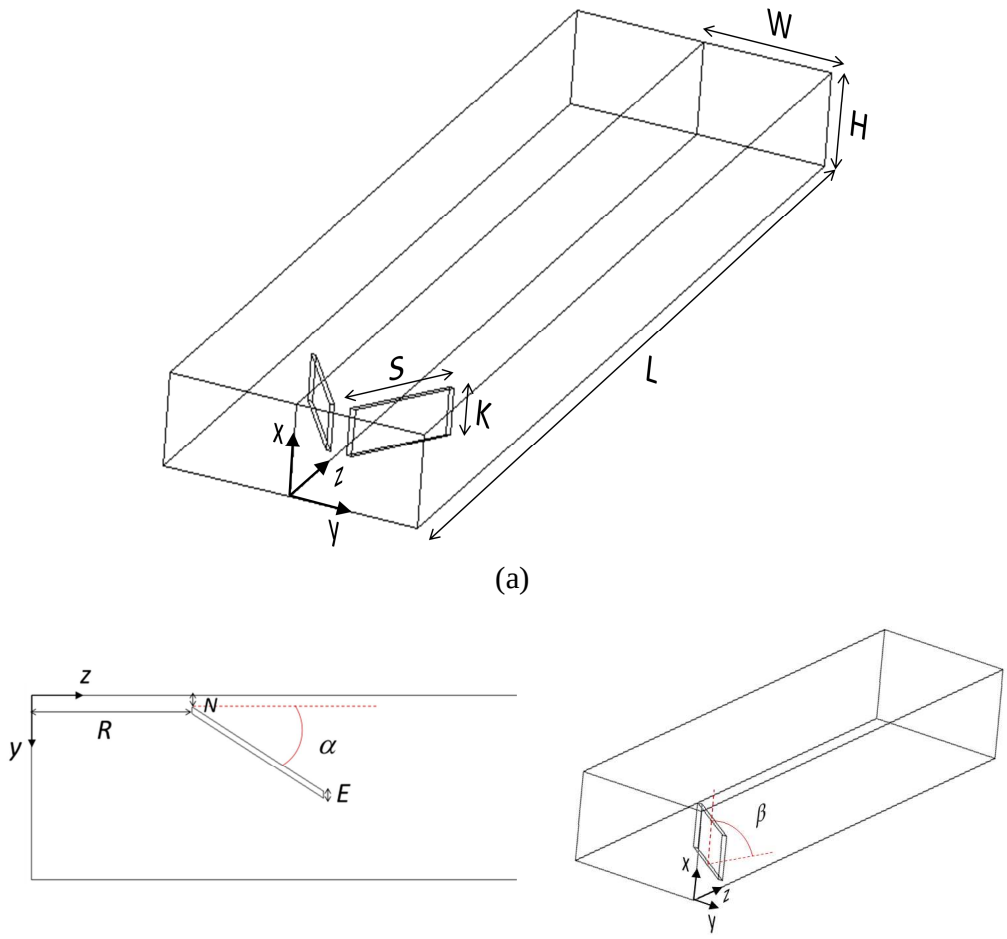

Figure 4.7:(a) Isometric view of the computational domain, (b) top view showing the attack angle α and (c) the isometric view where angle β is represented.

Channel height	*H*	38.6 mm
Channel width	*W*	1.6*H*
Channel length	*L*	13*H*
Angle of attack	α	30^{o}
Roll-angle	β	20° – 90°
VG length	*S*	1.5*H*
VG height	*K*	0.5*H*

Distance from the inlet to VG	*R*	1.55*H*
VG thickness	*E*	0.052*H*
Distance from the symmetry wall to VG	*N*	0.1*H*

Table 4.1. Dimensions of the computational domain and VG.

4.3 Mesh study

A non-uniform polyhedral mesh is generated in the core of the computational domain. Near the wall and VG surfaces, a prism-layer refinement mesh is preferred due to the presence of high velocity, temperature and pressure gradients in these regions. An example of the mesh on a flow cross section is shown in Figure 4.8.

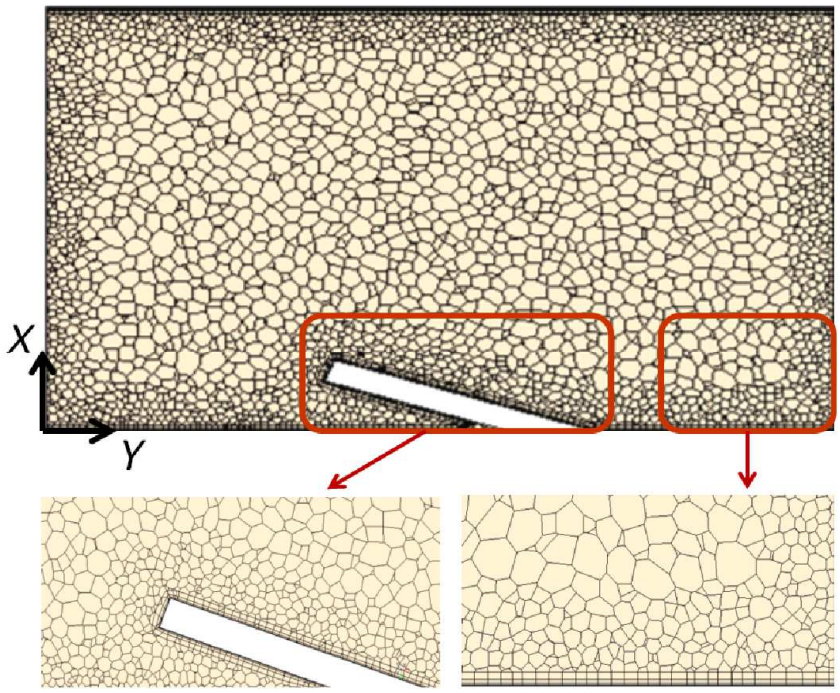

Figure 4.8: Example of the mesh on a cross section showing the refinements around the VG and near the walls for β=20°.

To determine the appropriate mesh density, the solver is run with increasing mesh densities until no significant effect on the results is detected. When the solution is reached to a grid independent solution for which the results change so little with a denser or looser grid where the errors can be neglected in numerical simulation. The mesh validity verification is performed first by using the method proposed by Celik *et al.* [51] where the grid convergence index (*GCI*) and the apparent order of convergence (*c*) can be obtained. In the present study the mesh refinement is assessed by means of the global Nusselt number which is a major interest in our study. This dimensionless number represents the ratio of convective to conductive transfer defined as:

$$Nu = \frac{hD_h}{k_f} \tag{4.1}$$

where h is the heat transfer coefficient (W/m^2.K), D_h is the hydraulic diameter equal to 2H (m) and k_f is the thermal conductivity of the working fluid (air) (W/m.K).

In this equation, the global heat transfer coefficient is obtained from the logarithmic mean temperature difference:

$$h = \frac{\dot{q}}{A\Delta T_{lm}} \tag{4.2}$$

where $\dot{q}$ is the global rate of heat transfer (W) defined in equation (4.3), A is the heat transfer surface area (m^2) and ΔT_{lm} is the logarithmic mean temperature difference defined in equation (7).

$$\dot{q} = \dot{m}\, C_p \Delta T \tag{4.3}$$

where $\dot{m}$ is the mass flow rate (kg/s), C_p is the specific heat (J/kg.K) and ΔT is the temperature difference between the flow inlet and outlet ($\Delta T = (T_{out} - T_{in})$).

$$\Delta T_{lm} = \frac{(T_{in} - T_w) - (T_{out} - T_w)}{\ln\left(\frac{T_{out} - T_w}{T_{in} - T_w}\right)} \tag{4.4}$$

where T_{in} is the inlet bulk temperature, T_{out} is the outlet bulk temperature and T_w is the wall temperature.

The different mesh densities and their features are represented in Table 4.2. The mesh size is obtained by a relation of the cell volume and the total number of cells as mentioned in Table 4.2. It is desirable that the grid refinement factor be greater than 1.3 as proposed by Celik *et al.* [51]. Based on equations (4.1) to (4.3), the Nusselt number is calculated for each mesh density then the convergence order *c* and *GCI* are computed based on the method proposed by Celik *et al.* [51].

Hence, it is found that the uncertainty in the fine-grid solution is $GCI = 1.25\%$ and the convergence order is $c = 5.97$, which are both accepted values for which the results are considered to be grid independent. For more details about the calculation of *c* and *GCI* the reader can refer to Celik *et al.* [51]. It should be noted that the mesh study presented here is done on the highest Reynolds number (*Re*=911).

Mesh	M0	M1	M2
Number of cells	621,424	1,251,620	2,711,600
Mesh size	0.369	0.293	0.226
Refinement factor	-	1.3	1.3

Table 4.2. Mesh characteristics.

Additionally, local mesh study is also performed by considering a transversal probe line located at a distance *S* downstream from the winglet (see Figure 4.9) on both bottom and the top walls of the duct, where the wall heat fluxes transversal profiles can be analyzed. Another probe line is created in the core flow, at the center of the duct (*H*/2) and at the same distance downstream from the winglet, to enable the velocity and temperature transversal profiles analysis for each mesh density considered.

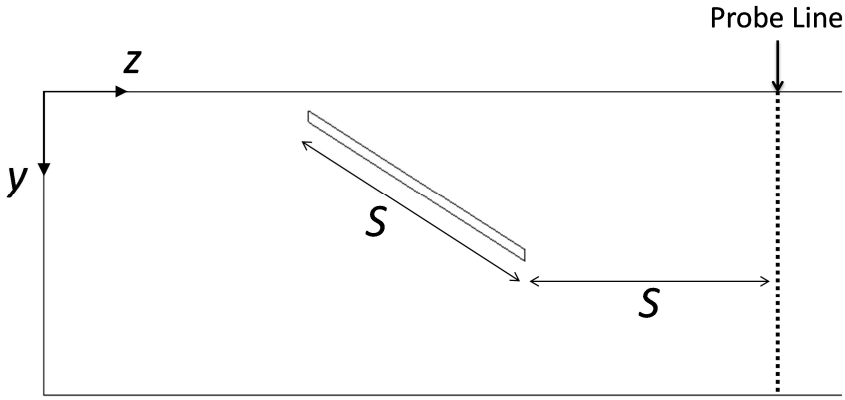

Figure 4.9: Top view of the computational domain showing the probe line created downstream the VG for local mesh analysis.

The local relative errors between mesh densities M1 and M2 are calculated for various variables using the following equations:

- for heat flux on the top and bottom walls:

$$\varepsilon_q = \left| \frac{q_{M1} - q_{M2}}{q_{M2}} \right| \tag{4.5}$$

- for velocity in the core flow (*H/2*):

$$\varepsilon_v = \left|\frac{v_{M1} - v_{M2}}{v_{M2}}\right| \tag{4.6}$$

- for dimensionless temperature Θ at mid-channel height:

$$\Theta = \frac{T - T_w}{T_{in} - T_w} \tag{4.7}$$

$$\varepsilon_\Theta = \left|\frac{\Theta_{M1} - \Theta_{M2}}{\Theta_{M2}}\right| \tag{4.8}$$

Based on the results presented in Figure 4.10, it can be seen that the relative errors between the M1 and M2 mesh densities always do not exceed 2.5%.

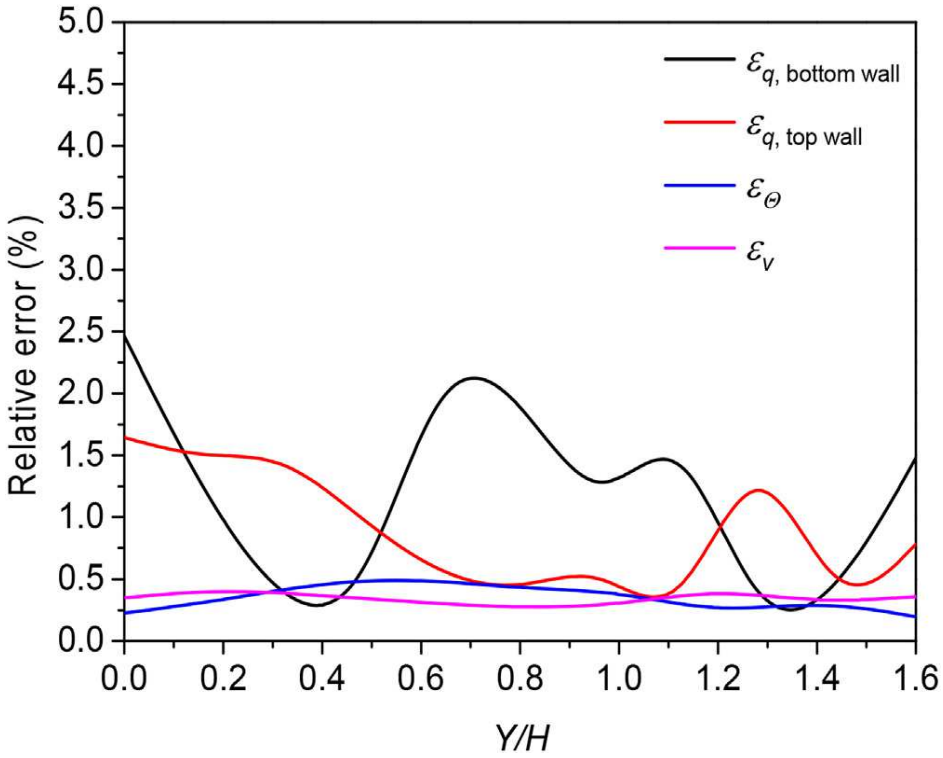

Figure 4.10: Relative local error for bottom and top wall heat fluxes, velocity and dimensionless temperature between the meshes M1 and M2.

To verify the unsteadiness of the flow, numerical simulations where run using the unsteady laminar solver. After observing the temporal variation of the velocity and temperature fields, it was concluded that there is no unsteadiness. The time variation of the rate of heat

transfer was of the order of 10^{-4}W which is negligible. The steady laminar flow assumption was also made in several studies from the open literature such as Lu and Zhou [62] and Dezan et al. [63].

Moreover, additional numerical simulations were run for the empty channel computational domain for both Reynolds numbers and for two different cases: in the first the density is kept constant and there are no gravity effects, whereas in the second case we use the Boussinesq approximation for the air properties and including gravity effects. It is found that the relative error on the Nusselt number did not exceed 5.5%. Thus, we neglect the buoyancy effects in all the simulations. Therefore, the effect of the temperature variation on the density of the fluid and thus its incompressibility constraints are unknown.

4.4 Results and discussions

The major purpose of the present study is to represent the effect of the roll angle on the heat transfer performance. To do so, the flow topology and the temperature distribution are studied along the duct. In addition, investigations are done on the local and global level parameters to check the effect of the roll-angle on the enhancement of the heat transfer.

Since the velocity and the temperature are set to be uniformed at the inlet of the computational domain, it is considered that the flow is a developing flow. For thermally and hydraulically developing laminar air flow, the results are validated for global Nusselt number using Stephan correlation [62]. The local Nusselt number is represented as followed:

$$Nu_x = 7.55 + \frac{0.024x_*^{-1.14}(0.0179Pr^{0.17}x_*^{-0.64} - 0.14)}{(1 + 0.0358Pr^{0.17}x_*^{-0.64})^2} \tag{4.9}$$

with

$$x_* = \frac{x}{D_h RePr} \tag{4.10}$$

This correlation is valid in the $0.1 \leq Pr \leq 1000$ for parallel plate channels in case of uniform wall temperature. Based on equations (4.9) and (4.10) the local Nusselt number is calculated and compared with computational results obtained for the empty channel case. Figure

4.11 represents the comparison between the correlation of equation (4.9) and the simulation results: the maximum percentage error is lower than 8% and the average error is 3.1% all along the duct, which is a very accurate result compared to commonly encountered values.

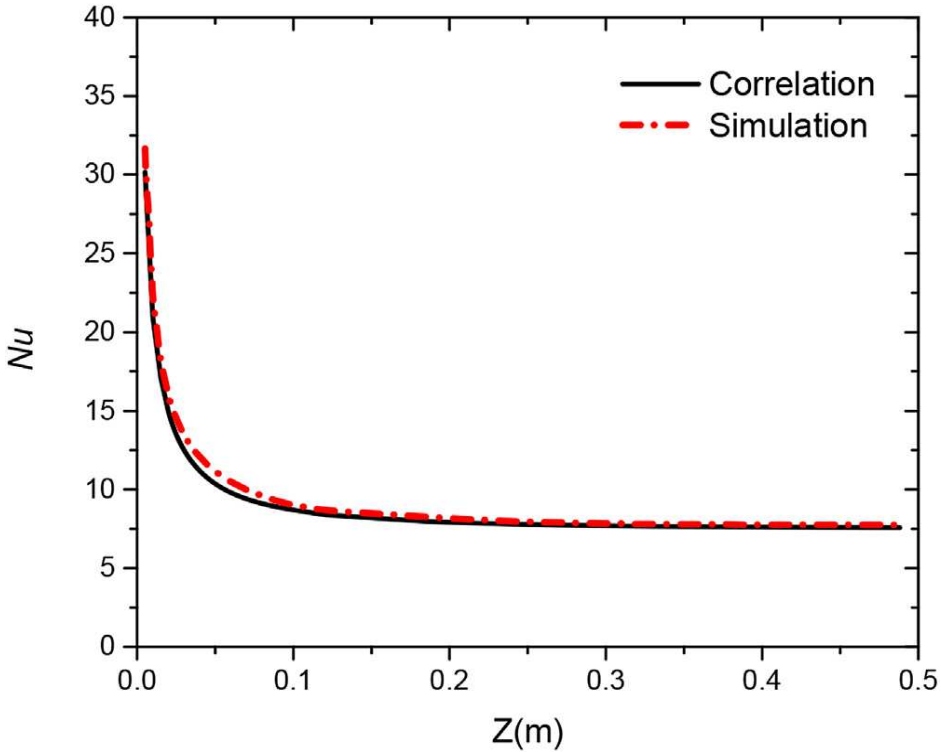

Figure 4.11: Local Nusselt number validation for the empty channel case.

4.4.1Flow structure and temperature distribution

In order to understand the behavior of the flow, the flow structure is first studied for two values of the roll-angle: β=20° and β=90°, and both Reynolds numbers, i.e. *Re*=456 and 911.

Figure 4.12 represents the helicity distribution along the duct for different cross sections located downstream the VG for the computational domain, for both β and *Re* values. Where the helicity is defined as followed:

$$\lambda = \frac{\vec{v} \,.\, \vec{\omega}}{|\vec{v} \,.\, \vec{\omega}|} \tag{4.11}$$

where $\vec{v}$ is the spin vector and the $\vec{\omega}$ is the momentum vector.

At Z=1.3H the location is just before the leading edge of the VG, whereas at Z=3.8H the plan is located just after the VG. As shown in Figure 4.12, rotating vortices are generated downstream from the VG. For the same Reynolds number, if we compare β=20° and β=90°, it is clear that how the roll-angle β effects on the generation of the vortices and their effect on the flow topology along the duct. For both Reynolds number, at Z=3.8H the helicity values drop to negative, this is due to the reverse vortices generated by the VG. As the roll-angle β increases, it is clear that the effect of the vortices generated will last longer along the duct until Z=11.6H which represents almost the outlet of the duct.

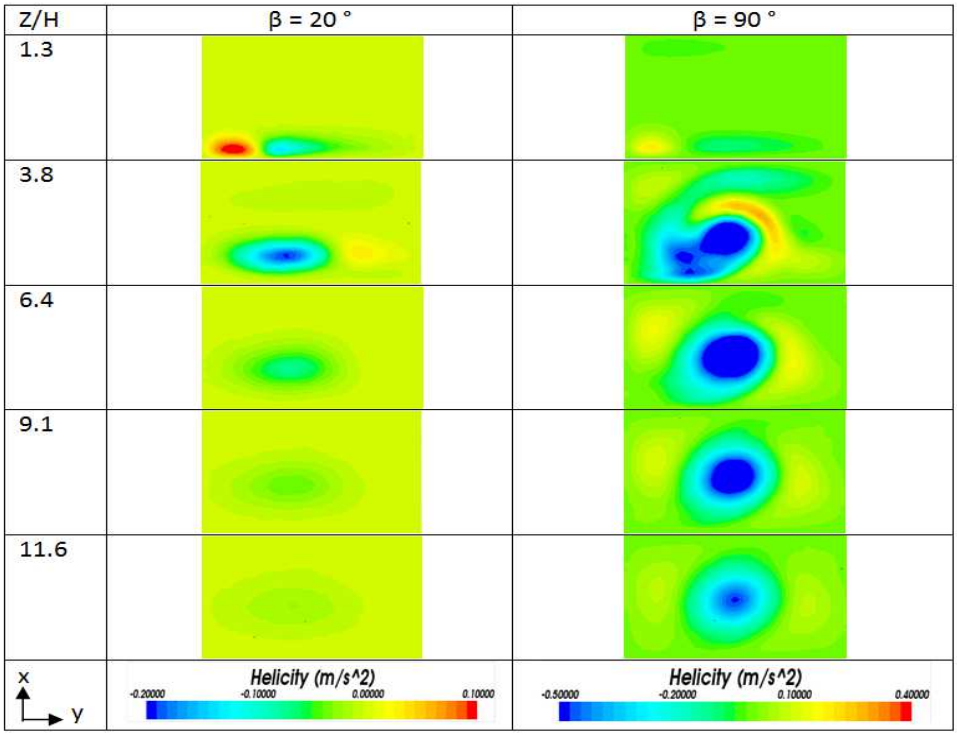

(a)

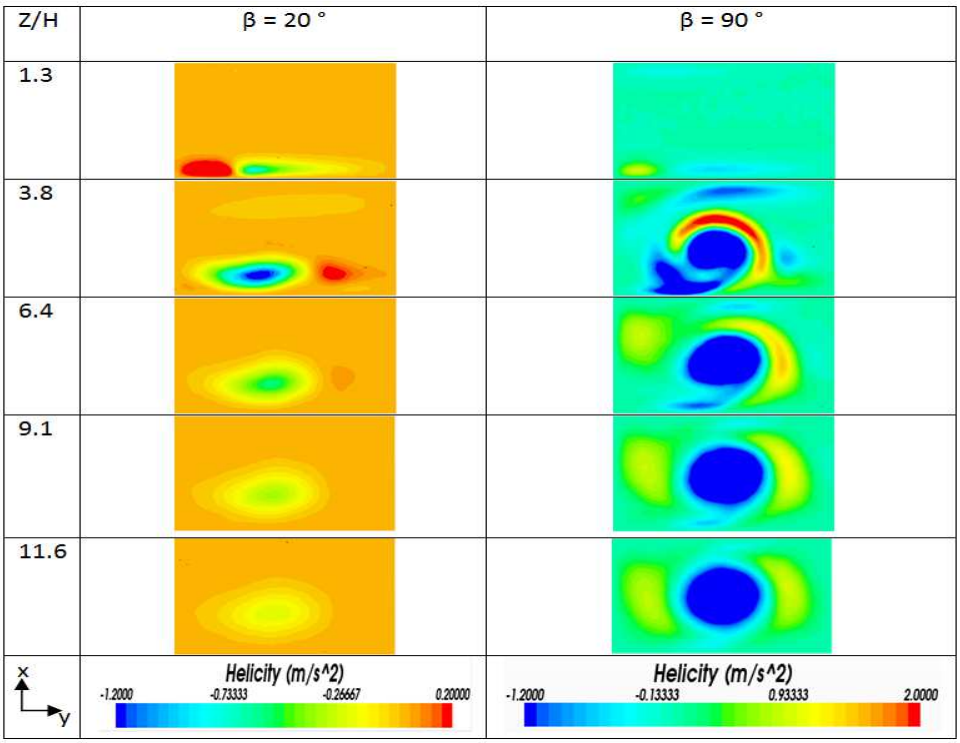

(b)

Figure 4.12: Helicity distribution for (a) *Re*=456 and (b) *Re*=911 on different flow cross sections.

In Figure 4.13 the temperature distribution is represented for both Reynolds number values and roll-angles. From this figure, it is clearly shown that the streamwise vortices previously mentioned affect the temperature distribution downstream the VG, especially for the highest angle. Indeed, in the common flow down region, between the two main vortices (i.e. in the symmetry plane of the RWP), hot fluid particles are ejected from the top wall towards the flow core due to upwash effect, while the thickness of the thermal boundary layer on the bottom wall is found to decrease due to downwash effect. In the common flow up region (i.e. between two neighboring vortex pairs) the upwash effect ejects near-wall hot fluid from the bottom wall towards the flow core. This mixing process and thermal boundary thinning are clearly seen for the highest roll-angle value, due to the fact that the vortices are more energetic and cover larger area in the flow cross section. So, the heat transfer enhancement seems to be dependent of the roll-angle value. This will be assessed and discussed in the next paragraphs by representing the Nusselt number distribution and the vorticity strength streamwise development.

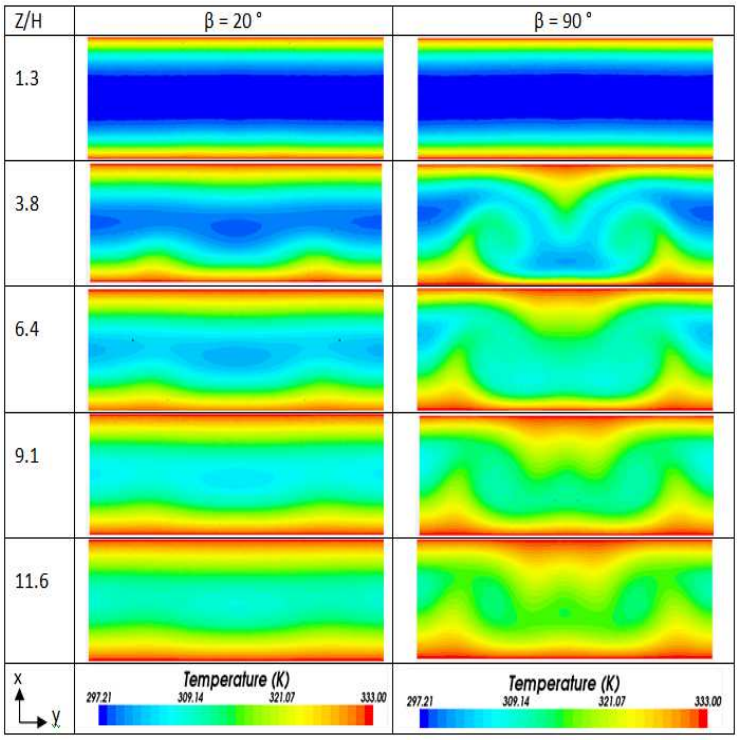

(a)

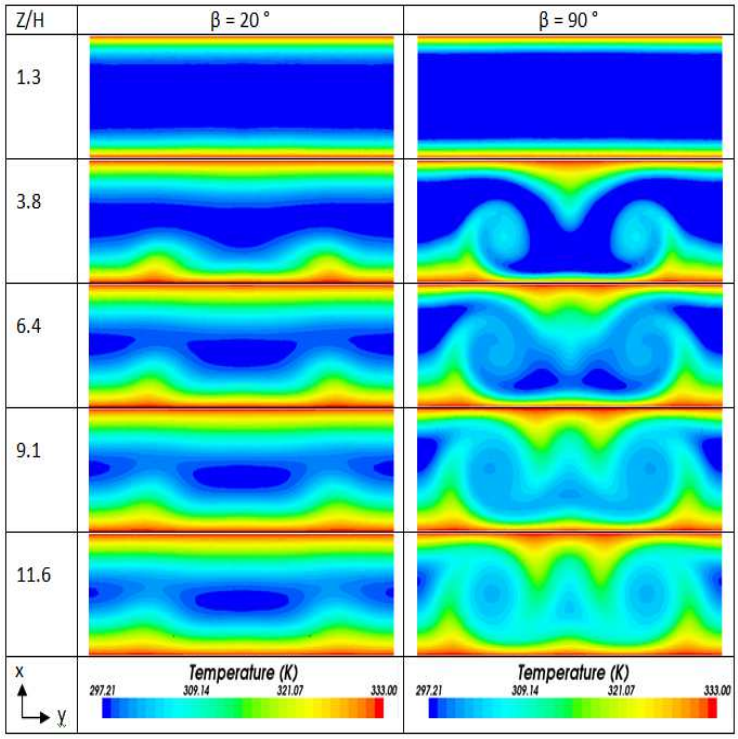

(b)

Figure 4.13: Temperature distribution for (a) *Re*=456 and (b) *Re*=911 on different flow cross sections.

The streamwise variation of the area-weighted average of the helicity is represented in Figure 4.14 for all the cases. The locations of the leading and trailing edges of the VG are represented by vertical dashed lines for each case. It is observed that the helicity values start to decrease in the beginning of the curve reaching even to negative values at a location just before the VG. After the flow encounters the VG, the averaged helicity is found to increase and reach its maximum value in the very near vicinity of the VG trailing edge because of the generated vortices, for Z between 1.5H and 3H. It can be noticed that the helicity peak for β=90° is about 12 times higher than that for β=20° meaning higher energetic vortices.

For 20°<β<60° the profile of the vorticity streamwise evolution is similar having a maximum at the tail of VG and decreasing continuously along the duct because of the dissipation of the LV. Whereas for higher β values (70° and 90°), secondary peaks are generated along with the duct due to the secondary vortices generated.

For Re=911, the value of the helicity peak increases by a factor of 3 compared to that of Re=456. As a profile of the curve, for all the angles, the maximum value of the helicity is at the tail of the VG. For small angle values 20°<β<40°, after reaching to the maximum value it fades away along the duct due to the dissipation of the LV. For 50°<β<90° a secondary peak is generated each at a different location along the duct. It is interesting to notice that for β=60°, 70° and 90°, similar values of helicity are obtained near VG whereas along the downstream direction of the duct, both β=60° and 70° have a secondary peak due to the secondary vortices. The secondary peak values of both β=60° and 70° are almost equal, but the primary peak value of the β=70° is higher than that of the β=60°. On the other hand, for β=90°, the primary peak value is higher than that of all the cases but the effect of the secondary vortices are smaller compared to that of β=60° and 70°. It can be concluded that based on the helicity values, β=70° appears to be the optimal angle that can be considered for Re=911 compared to the other values of roll-angle.

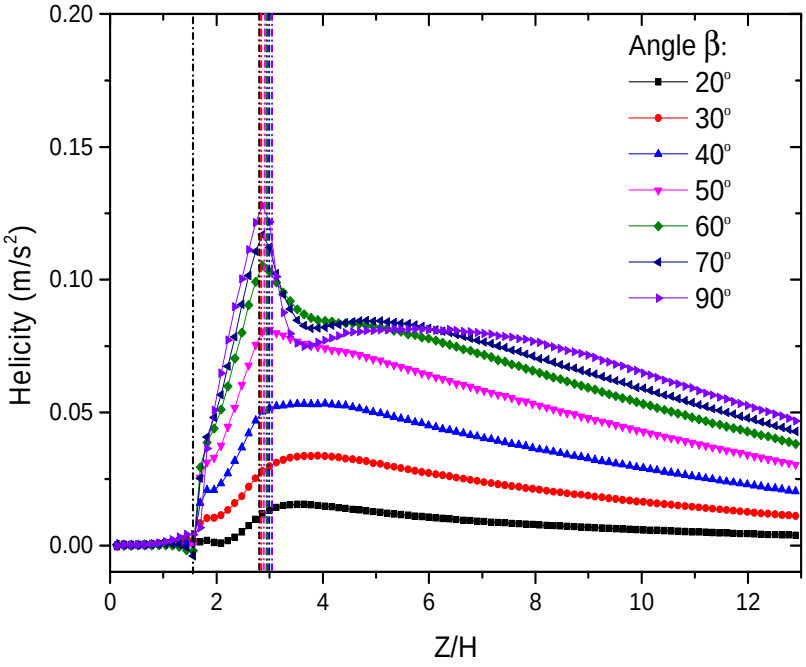

(a)

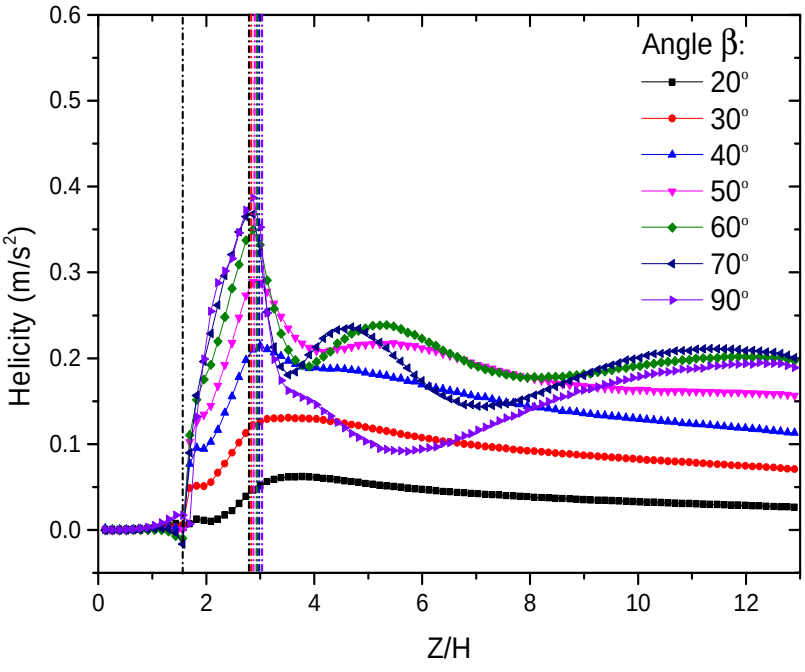

(b)

Figure 4.14: Variation of averaged helicity along the duct for (a) *Re*=456 and (b) *Re*=911

In Figure 4. 15 the streamwise variation of the dimensionless location of the main vortex is presented, where the distance between the vortex core and the bottom wall is measured. It is observed that for *Re*=456, the position of the core of the main vortex starts in an increasing profile for all the values of roll-angle just after the tail of the VG. It is observed that by increasing the value of β, the position of the main vortex increases reaching a maximum location at a value of X=0.5*H* for β=90°, which represents the half of the duct height.

For the case *Re*=911 the position of the core of the main vortex increases with the increase of the β. By comparing both Reynolds numbers, it is obvious that for *Re*=911 the increase is more rapid, where for high values of β, the location of the core of the main vortex reaches the half of the duct height more quickly. On the other hand, for low values of β, the location of the core of the main vortex will not reach that height.

As the dimensionless location of the core of the main vortex reaches the half of the duct height, it leads to a better mixing of the fluid in the duct. As a result, the heat transfer rate increases, and then the Nusselt number is affected. The variation in the Nusselt number is studied in the coming sections, in order to provide a clear view of the effect of the roll-angle β on the heat transfer enhancement.

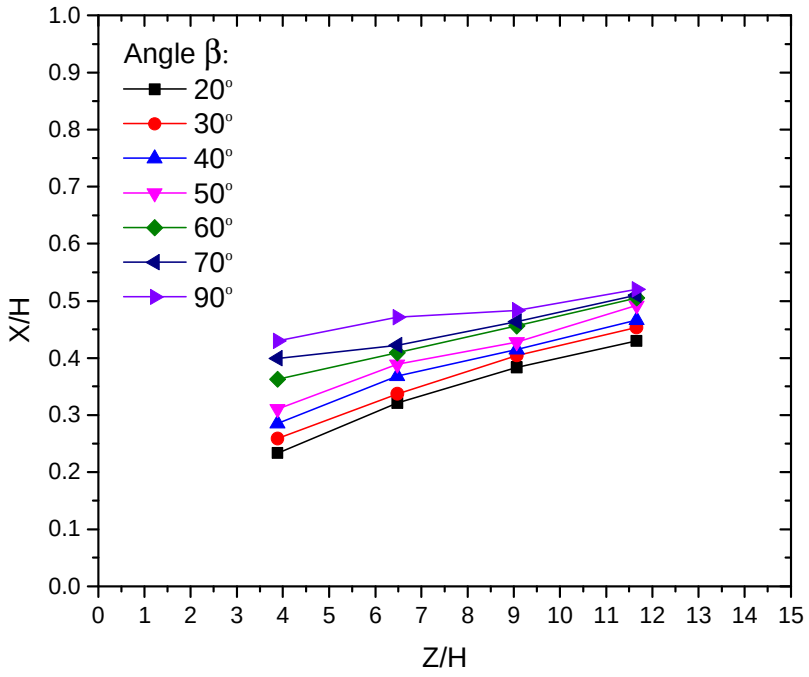

(a)

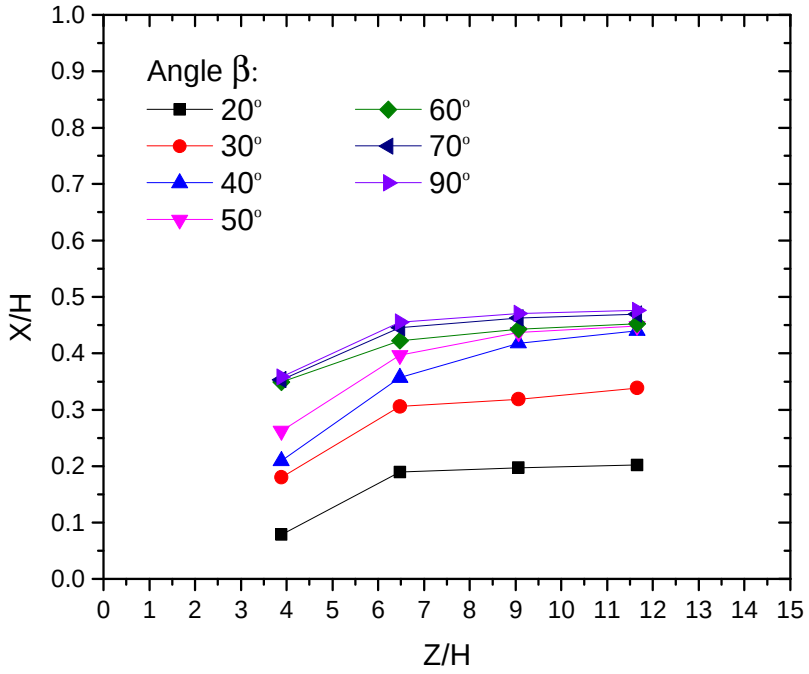

(b)

Figure 4. 15: Dimensionless location of the main vortex along the duct for (a) *Re*=456 and (b) *Re*=911.

4.4.3 Local performance

In order to study the local performance, different locations behind the VG are considered on both bottom and top walls where the wall heat flux density is studied for each case. Figure 4.16 and Figure 4.17 represent the results obtained for β=20° and β=90° for both Reynolds numbers. At a short distance from the VG (Z/*H*=6.7) the secondary vortex can still be seen. Along the downstream, the heat flux density is dominated by the main vortices. By increasing the distance Z/*H*, the heat flux density decreases, and the vortices diverge.

By comparing Figure 4.16 and Figure 4.17, the effect of the roll-angle β is introduced on the local performance. Whereas for β=90°, both bottom and top wall heat flux values are higher than that of β=20°.

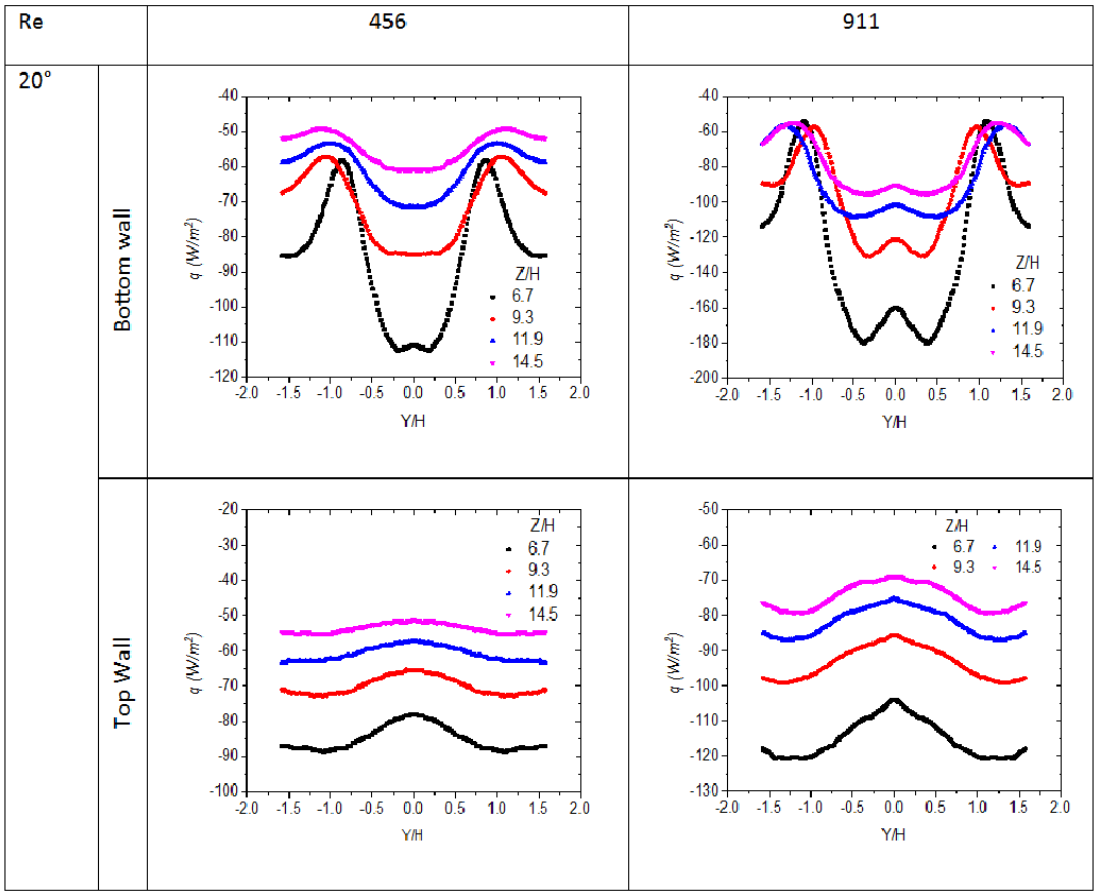

Figure 4.16: Heat flux both on bottom and top walls for different locations away from the VG both for *Re*=456 and *Re*=911 for β=20°.

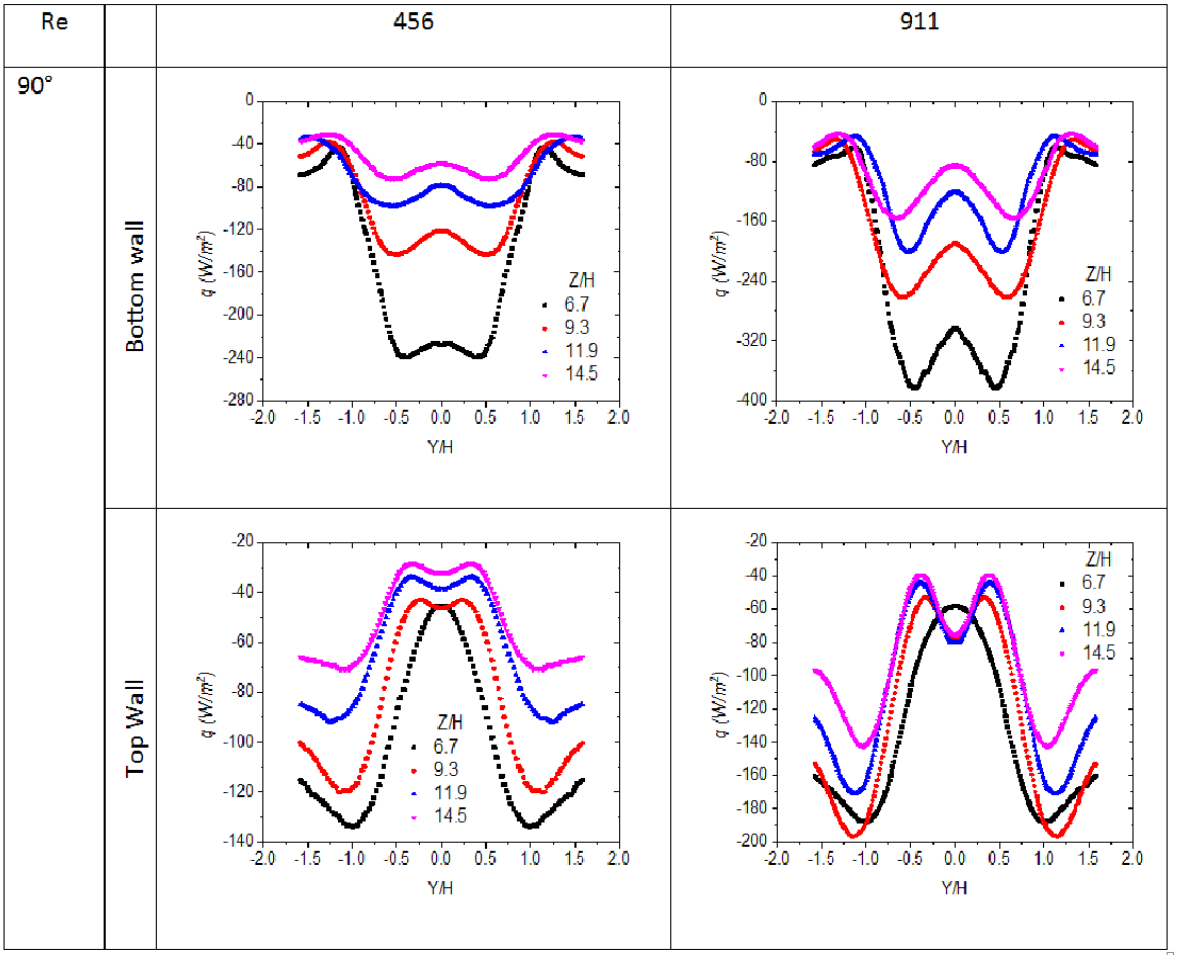

Figure 4.17: Heat flux both on bottom and top walls for different locations away from the VG both for *Re*=456 and *Re*=911 for β=90°.

The streamwise variation of the cross-section averaged Nusselt number is presented in Figure 4.18 and Figure 4.19 for bottom and top walls respectively, on which the vertical dashed lines represent the leading and trailing edges of the VG. The average Nusselt number on each cross section is obtained by the following equation:

$$Nu = \frac{2H}{k_f}\frac{q"}{(T_w - T_f)} \tag{4.12}$$

$$Nu(z) = \frac{2H}{k_f} \frac{q"(z)}{\left(T_w - T_f(z)\right)} \tag{4.13}$$

where $q"$ is the average wall heat flux density on both walls, $q"$(z) is the average wall heat flux density at a given (z) streamwise location, k_f is the thermal conductivity of the fluid, T_w the wall surface temperature and T_f(z) the fluid bulk temperature at a given Z cross-section.

The streamwise distribution of the span-averaged Nusselt number is plotted for all values of roll-angles β as well as for the case of the empty duct. For both Reynolds numbers, similar profile is obtained, where at the inlet of the duct, the Nusselt number values decrease until the location Z=1.6*H* which represents the head of the VG. At that location the Nusselt number value starts to increase due to the heat transfer enhancement until it reaches the tail of the VG where it drops to the minimum. For low values of β the Nusselt number value drop is found to be even below that observed for the empty duct channel. This drop is seen at a location Z=2.3*H* which is at the tail of the VG. After the drop a second peak is generated where the value of the Nusselt number increases at a location of just after the VG (Z=2.5H). For all the values of angle β, a similar profile is obtained where a second peak is generated just after the VG after which it decreases with a small oscillation along the longitudinal direction of the duct.

The drop in the Nusselt number curve below the value observed for the empty duct channel occurs only on the bottom wall. In Figure 4.19, it is clear that the Nusselt number for the top wall decreases in the inlet of the duct, until location Z=1.6*H*, the value starts to increase reaching their maximum at Z=2.3*H* which represents the tail of the VG. After which the curves start to drop along the longitudinal direction of the duct with.

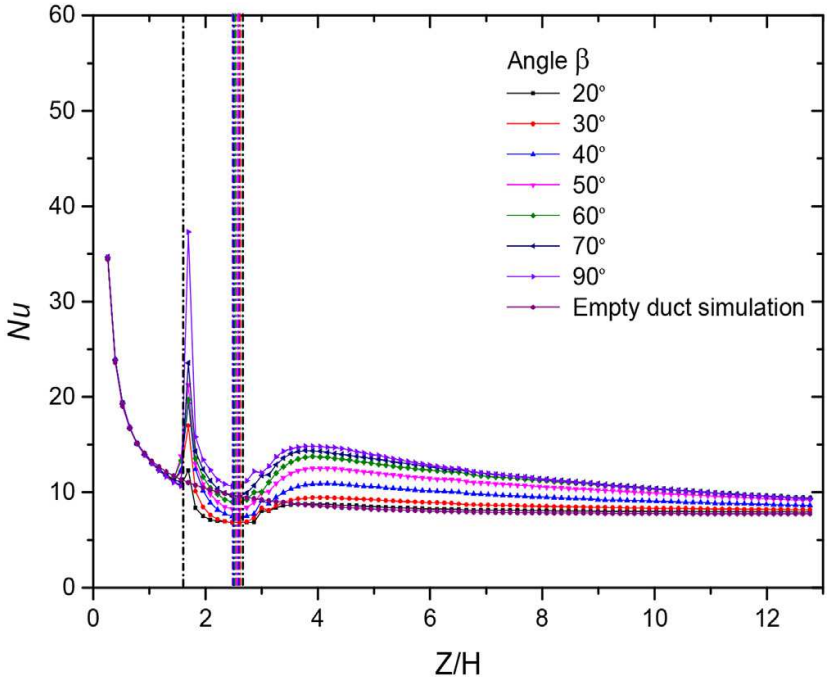

(a)

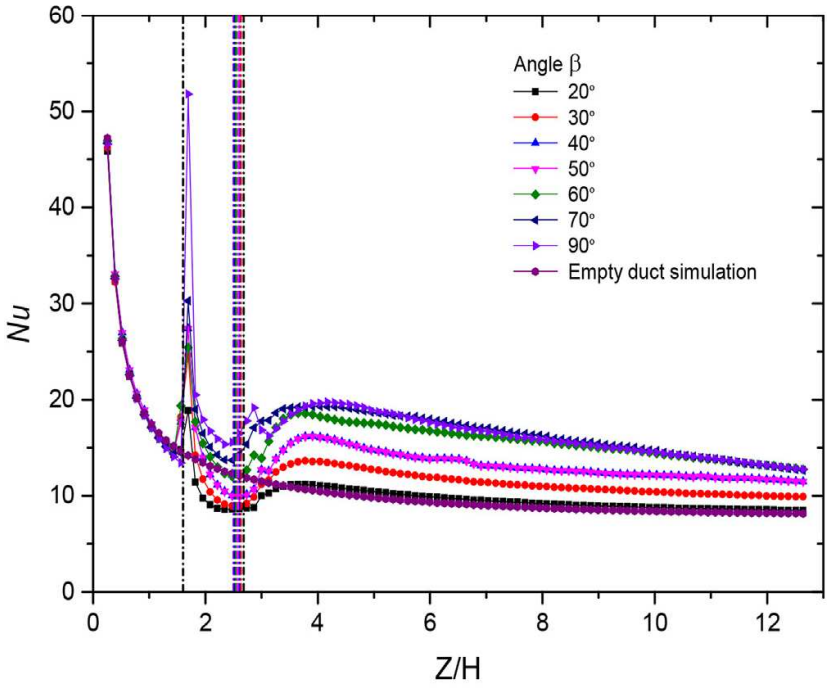

(b)

Figure 4.18: Bottom wall and VG Nusselt number for (a) *Re*=456 and (b) *Re*=911.

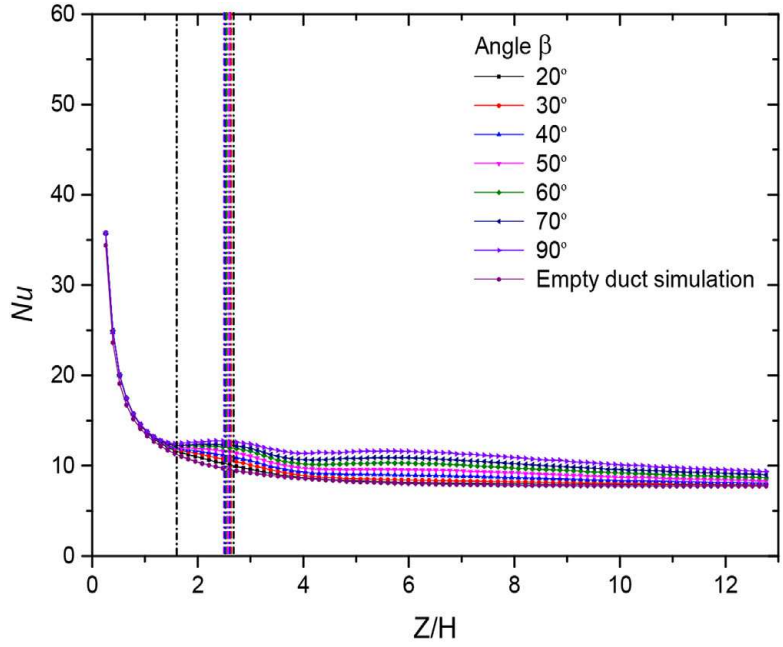

(a)

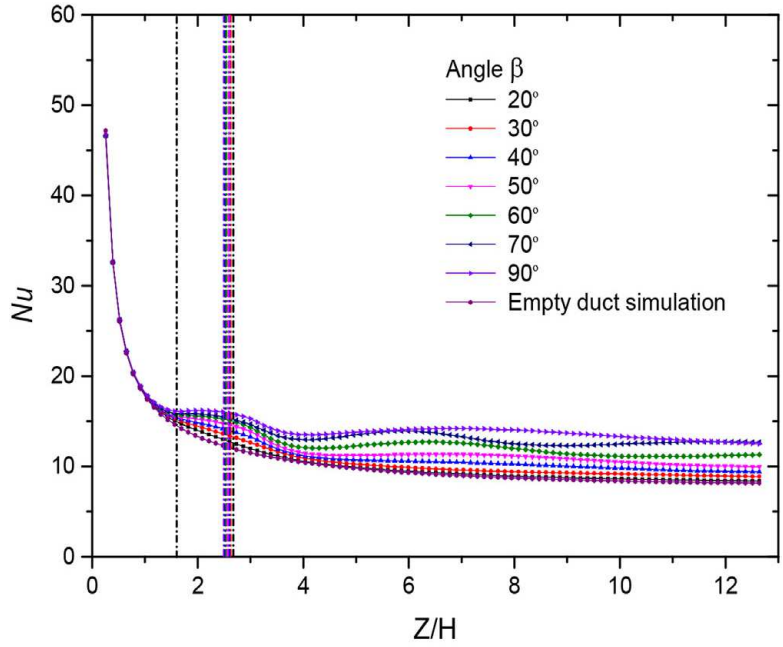

(b)

Figure 4.19: Top wall Nusselt number for (a) *Re*=456 and (b) *Re*=911.

To understand the drop of the Nusselt number below that of the empty duct curve at the VG location in some studied cases, a study is performed to check the interaction between the heat flux on the bottom wall and the top wall and the near-wall velocity profile. In Figure 4.20 and Figure 4.21 the boundary heat flux and the velocity fields are displayed for roll-angles equal to 20° and 90°, for both Reynolds numbers values. The planes are taken at a distance of X=*H*/8 away from the bottom or top wall, knowing that X=0 represents the bottom wall location. It appears that the velocity value for the bottom wall case at a location under the area of the VG highlighted by a circle is nearly zero. For low values of β this area of velocity null is greater than for the case of high β, implying that there is a bigger region where a bigger dead zone is created under the VG, where due to zero velocity there is almost no heat transfer due to convection. As a result, Nusselt number value is dropping even below that of the empty duct channel case. On the other hand, since there is no VG placed on the top wall, there is no dead zones created. Thus, there is convective heat transfer on the top wall enhanced by the presence of the VG on the bottom wall. This is supported by the values of the Nusselt number, represented in Figure 4.19 for the top wall, on which for all the values of roll-angle β, the curves are above the values of the empty duct channel.

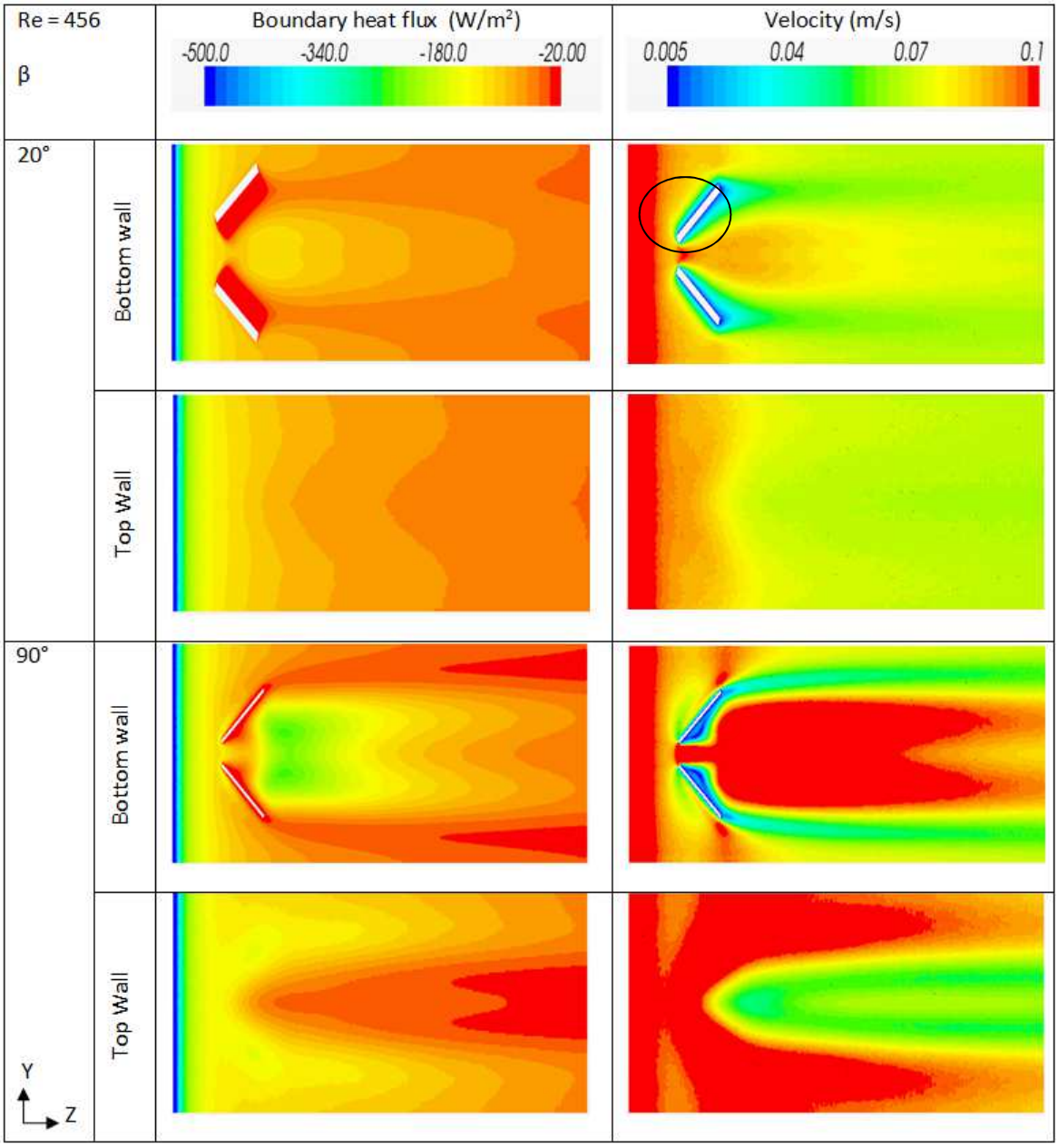

Figure 4.20: Heat Flux profile for bottom and top walls and the velocity profile at an $X=H/8$ away from both bottom and top walls for Re=456.

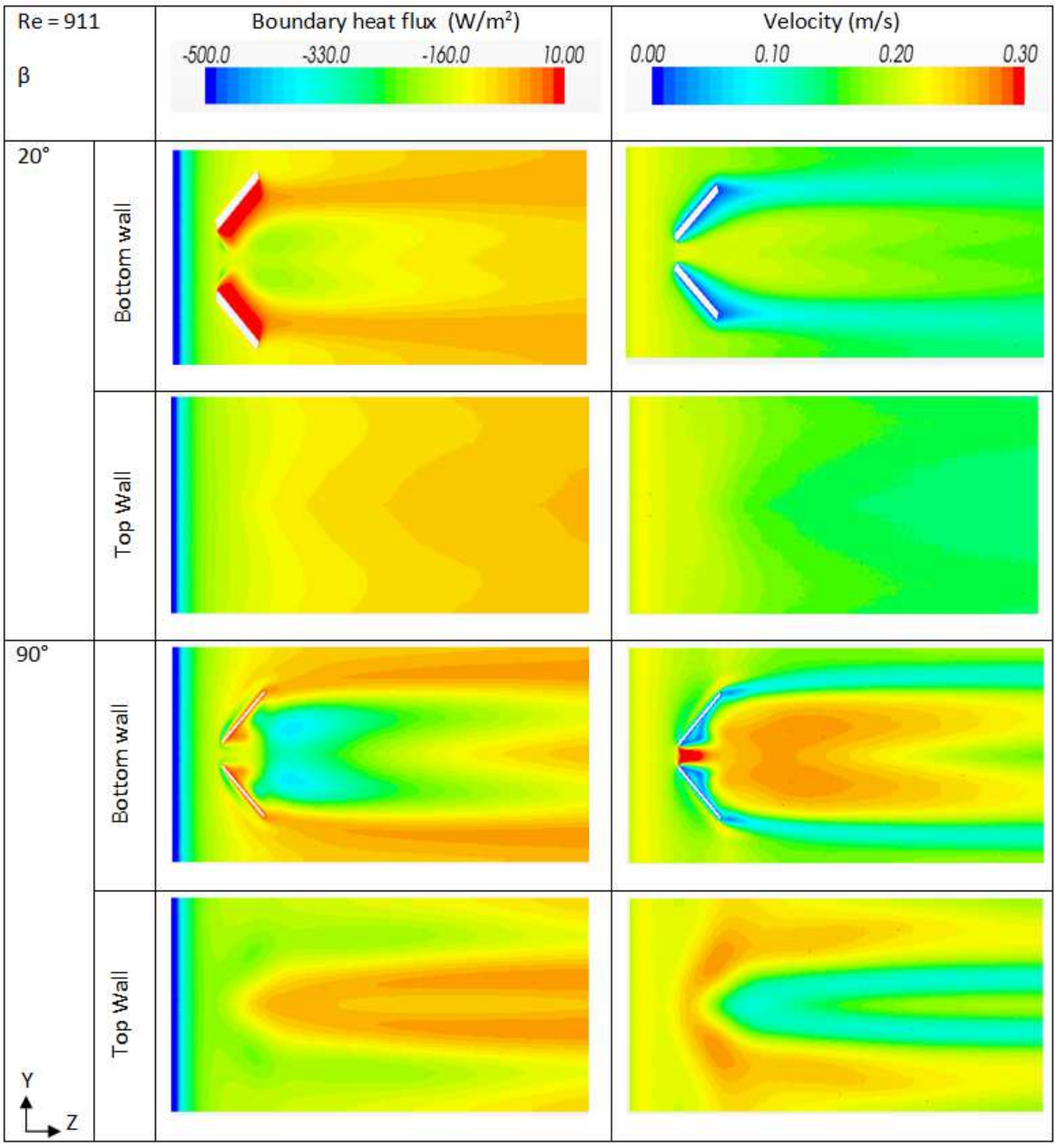

Figure 4.21: Heat Flux profile for bottom and top walls and the velocity profile at an $X=H/8$ away from both bottom and top walls for Re=911.

Fanning friction factor is calculated from the pressure gradient obtained from the simulation. As Darcy's friction can be calculated by:

$$f_{darcy} = 2\frac{D_h}{L}.\frac{\Delta p}{\rho U^2} = \frac{4H\Delta p}{L\rho U^2} \tag{4.14}$$

thus

$$f = \frac{f_{darcy}}{4} = \frac{H\Delta p}{L\rho U^2} \tag{4.15}$$

where H is the height of the duct (m), Δp is the pressure drop (Pa) between the inlet and the outlet, L is the length of the duct, ρ is the fluid density (kg/m^3) and U is the mean flow velocity (m/s).

In order to calculate the local Fanning friction factor $f(z)$, the following relation is used:

$$f(z) = \frac{f(z)_{darcy}}{4} = \frac{H\Delta p(z)}{Z\rho U^2} \tag{4.16}$$

where $\Delta p(Z)$ is the pressure drop (Pa) between the inlet and the cross section at location Z.

In Figure 4.22, the streamwise evolution of the friction factor is represented. For both Reynolds numbers the profile of the curve for high roll-angle values (β=50°, 60°, 70° and 90°) is similar where it starts to drop along the length of the duct until it reaches the leading edge of the VG. At that point, a gradual increase starts to appear reaching its maximum value at the tail of the VG, after which the curve continues to drop making an asymptote with the empty channel curve. On the other hand, for low values of roll-angle (β=20°, 30° and 40°) the profile starts to drop along the length of the duct until it reaches the leading edge of the VG. At that point an increase starts to appear that last for small values of *Z/H*, after which the curve continues to drop making an asymptote with the empty channel curve.

For the case *Re*=456 the maximum peak obtained is higher than that of the case *Re*=911 knowing that the friction factor in inversely proportional to the fluid velocity which by itself directly proportional to the Reynolds number. On the other hand, the pressure drop Δp value for *Re*=911 is higher than that of *Re*=456, but the ratio of it with respect to the velocity square is lower than that for *Re*=456.

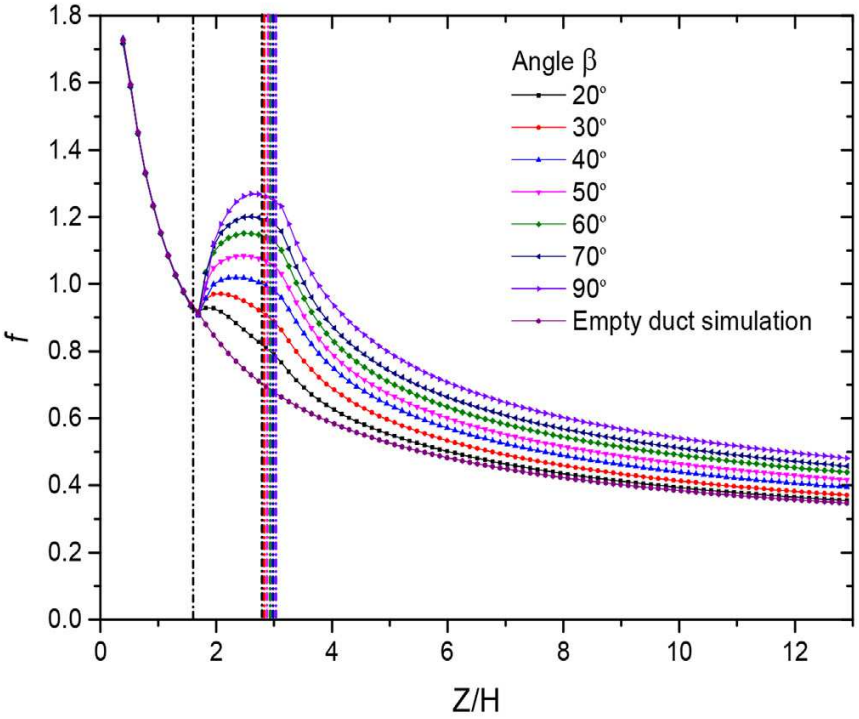

(a)

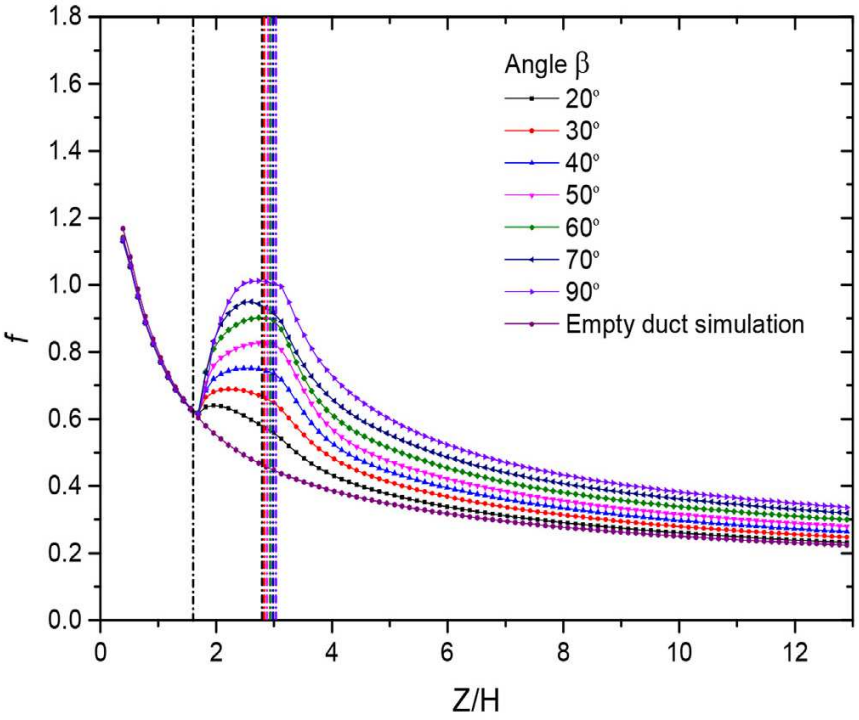

(b)

Figure 4.22: Friction factor streamwise variation for (a) *Re*=456 and (b) *Re*=911.

4.4.4 Global performance

In order to study the global effect of the transverse angle β of the VG on the enhancement of the heat transfer, global values of the Nusselt number, friction factor and the enhancement factor are presented and discussed in this section.

Figure 4.23 represents the global Nusselt number plotted for both Reynolds numbers, versus the roll-angle β. The Nusselt number is calculated using equation (4.1). For both values of Reynolds numbers, the Nusselt number is found to monotonically increase with the value of the roll-angle. $\beta = 0°$ represents the empty duct channel. By comparing the empty duct values of Nusselt number with the other cases, for all the case the *Nu* value increases. A similar profile is obtained for both Reynolds values.

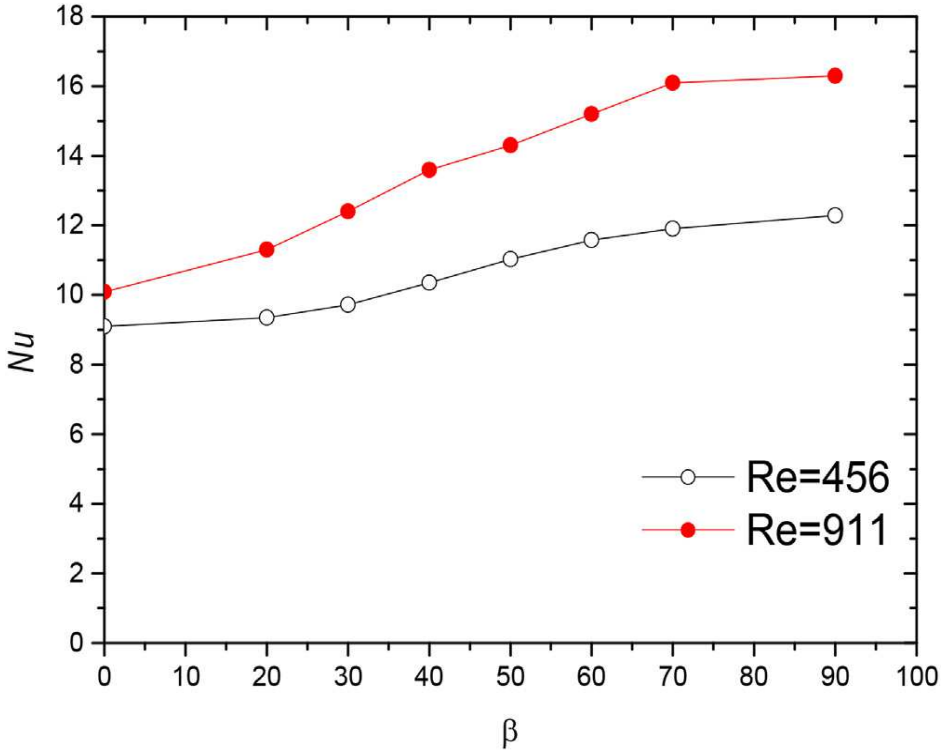

Figure 4.23: Global Nusselt number for *Re*=456 and *Re*=911.

The global friction factor is also plotted for both Reynolds numbers versus the roll-angle in Figure 4.24. The friction factor is calculated using equation (4.15). As the roll-angle β

increases, the friction factor increases too. For high values of angle β the pressure drop is high. As a result, the pressure gradient is increased leading to a high value of friction factor. $\beta = 0°$ represents the empty duct channel. By comparing the empty duct values of friction factor with the other cases, for all the case the friction factor value increases. A similar profile is obtained for both Reynolds values.

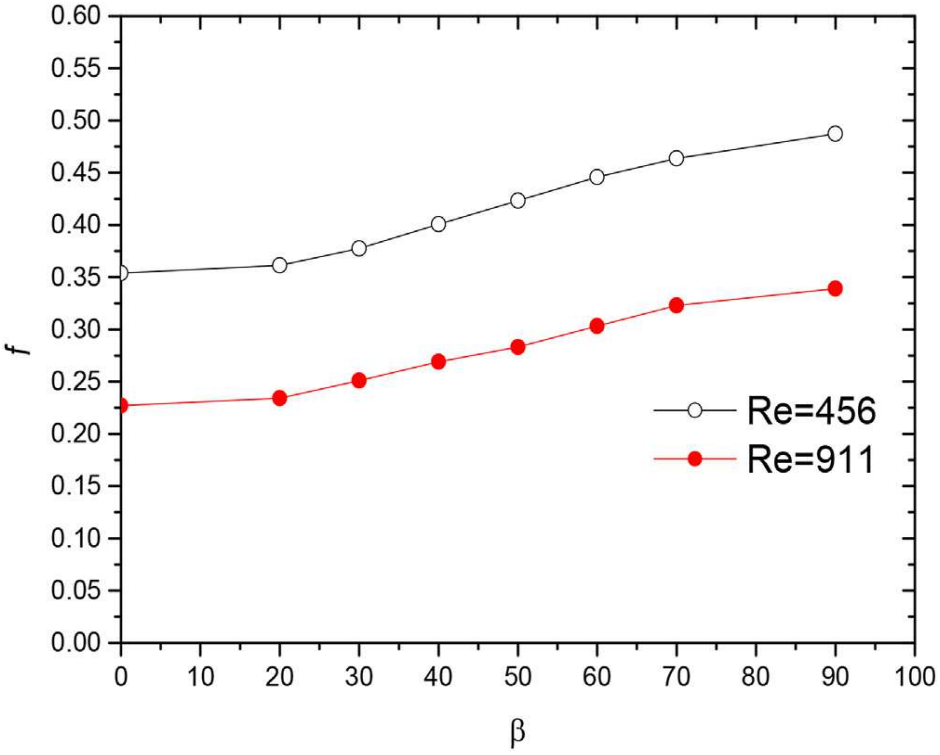

Figure 4.24: Global friction for *Re*= 456 and *Re*= 911.

Based on the previously mentioned relations of the Nusselt number and the friction factor, an enhancement factor is calculated using the following relation:

$$\eta = \left(\frac{Nu}{Nu_0}\right)\left(\frac{f}{f_0}\right)^{(-1/3)} \tag{4.17}$$

where Nu_0 and f_0 are the values of Nusselt number and friction factor respectively for the empty duct channel.

Figure 4.25 represents the enhancement factor for both Reynolds numbers. For *Re*=456, the value of the enhancement factor starts to increase monotonically with the increase of the transverse angle β reaching its maximum value of 1.2 at β=90°. On the other hand, for the case of *Re*=911 the profile of the enhancement factor curve starts to increase with the increase of the roll-angle β until it reaches a maximum value of 1.32 at β=70°, after which its value slightly drops to a value of 1.3 at β=90°. Thus, it can be considered that for the case *Re*=456 the optimum value of β is the highest angle 90°. Nevertheless, for the case *Re*=911 the optimum roll-angle among those tested values of β to provide the best enhancement is found to be 70° and not the highest angle. This is also supported by the helicity curve shown in Figure 4.12 where the secondary vortices are detected.

By comparing the values of the enhancement factor of both Reynolds numbers, for all the values of β, that of *Re*=911 have a higher percentage of enhancement than that of *Re*=456. For β=70°, the enhancement factor percentage of *Re*=456 is 1.18%, whereas for *Re*=911 is 1.32% having a difference of 0.14%. On the other hand, for β=20°, the enhancement factor percentage of *Re*=456 is 1.02%, whereas for *Re*=911 is 1.027% having a difference of 0.007%.

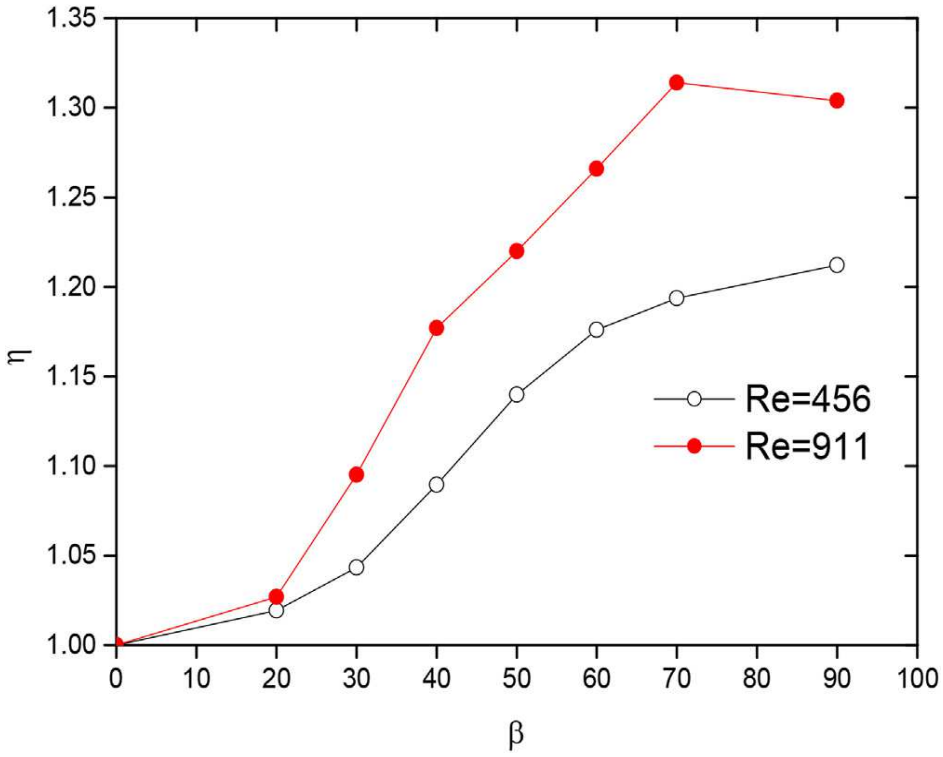

Figure 4.25: Enhancement factor for *Re*=456 and *Re*=911.

4.5 Conclusion

In this study, heat transfer and fluid flow characteristics in a rectangular duct with RWPVG inserted on its bottom wall are numerically investigated. For different values of generator's roll-angle (*β)* both local and global hydrodynamic and thermal parameters are calculated and studied. The goal of these studies is to figure out the effect of the roll-angle on the heat transfer enhancement. The main outcomes of this study can be summarized as followed.

For high values of roll-angle (close to *β*=90°), it is observed that the helicity increases just after the flow encounters the VG where the vortices are first formed. The helicity peak for *β*=90° is about 12 folds higher than that for *β*=20° meaning more energetic vortices. Moreover, increasing the mean flow velocity, i.e. the Reynolds number, leads to increase the helicity. It is observed that for *Re*=456, the dimensionless *X/H* position of the main vortex measured from the bottom wall, starts at low position and increases along the duct until it reaches a maximum value

of around 0.5 representing the middle of the duct for the highest value of roll-angle β. Whereas for the case of higher Reynolds number, dimensionless location of the main vortex is increased suddenly at the Z/H=6.5 and after that in continuous to increase gradually along the length of the duct. For Re=911, the highest value of X/H=0.5 is reached by the high values of β. Whereas for β=30° the value of the X/H=0.35 and for β=20°, X/H=0.2.

It is crucial to take into consideration that by increasing the roll-angle value, not only the heat transfer will be enhanced but on the other hand, the pressure drop will increase too. In order to be able to make decision for this challenging issue the enhancement factor is studied where both the heat transfer and the pressure drop are taken into consideration.

For Re=456, it is shown that the enhancement factor monotonically increases with the increase of the roll-angle β, reaching its maximum value of 1.2 at β=90°. On the other hand for the case of Re=911 the profile of the enhancement factor starts to increase with the roll-angle β until it reaches a maximum value of 1.32 near β=70°. Thus, it can be considered that for Re=911 the optimum roll-angle among those tested values of β which leads to the best enhancement is 70° and not the highest angle, while for Re=456 the optimum value of β among those tested is the highest angle 90°.

After all these investigations, it is crucial to mention that the roll-angle β has a significant effect on the enhancement of the heat transfer. It is interesting to study the 70° case in place of the perpendicular RWPVG for further investigations. As an advancement of the obtained results, few more values of β can be added for values near to 70° in order to find the exact value of the optimum angle. Due to different values of obtained for different Reynolds numbers, it is interesting to go to higher Reynolds and even study in the turbulent regime too.

CHAPTER 5

Rectangular Wing Vortex Generator

(The study of this chapter is published as an article "Effect of the angle of attack of a rectangular wing on the heat transfer enhancement in channel flow at low Reynolds number", in Heat and Mass Transfer in 2017.)

5.1 Introduction

Another solution for designing a VG whose shape changes with the variation of the dynamic pressure of the flow is the wing configuration with a variation of the angle of attack. IT is well known that the variation of the angle of attack has a certain importance on the formation quality of the longitudinal swirls and on the pressure loss caused by the VG. Anyway, in scientific bibliography the whole variation of angle of attack (with very low value of angle of attack) is not fully done. It is so important before using this solution in our auto-adaptative Heat exchanger to clearly assess the influence on heat transfer and pressure drop of high variations on angle of attack for a rectangular wing configuration.

This chapter presents numerical computation results of laminar convection heat transfer in a rectangular channel whose bottom wall is equipped with one row of rectangular wing vortex generators. The governing equations are solved using finite volume method by considering steady state, laminar regime and incompressible flow. Three-dimensional numerical simulations are performed to study the effect of the angle of attack α of the wing on heat transfer and pressure drop. Different values are taken into consideration within the range $0°<\alpha<30°$. For all of these geometrical configurations the Reynolds number is maintained to Re=456.

To assess the effect of the angle of attack on the heat transfer enhancement, Nusselt number and the friction factor are studied on both local and global perspectives. In addition, the location of the generated vortices within the channel is studied, as well as their effect on the heat transfer enhancement throughout the channel for all α values. Based on both local and global analysis, our results show that the angle of attack α has a direct impact on the heat transfer enhancement. By increasing its value, it leads to better enhancement until an optimal value is reached, beyond which the thermal performances decrease.

5.2 Computational domain and boundary conditions

The computational domain consists of one row of a rectangular wing (RW) placed in between two parallel plates as shown in Figure 5. 1(a). The computational domain has a height $H = 20$ mm, a width W=5H and a length L=15H. The RW is inserted near the entrance on the bottom wall at a distance P=H away from the inlet as shown in Figure 5. 1(b). The angle of attack α, which is the angle between the VG reference line and the incoming flow in the Z direction, is variable in a range from 0° to 30°. Remaining dimensions are given in Table 5.1in terms of the channel height H. Taking into account that both lateral sides are considered to be symmetry relative to the plan (x, z), the computational domain is considered to be the half of the VG transverse pitch, thus half of the main domain. Flow and heat transfer simulations are carried out for Reynolds number 456, with uniform inlet temperature set to $T_{in} = 293\ K$. Wall surface temperature $T_w = 333\ K$ is set for both bottom and top channel walls, as well as for the VG walls.

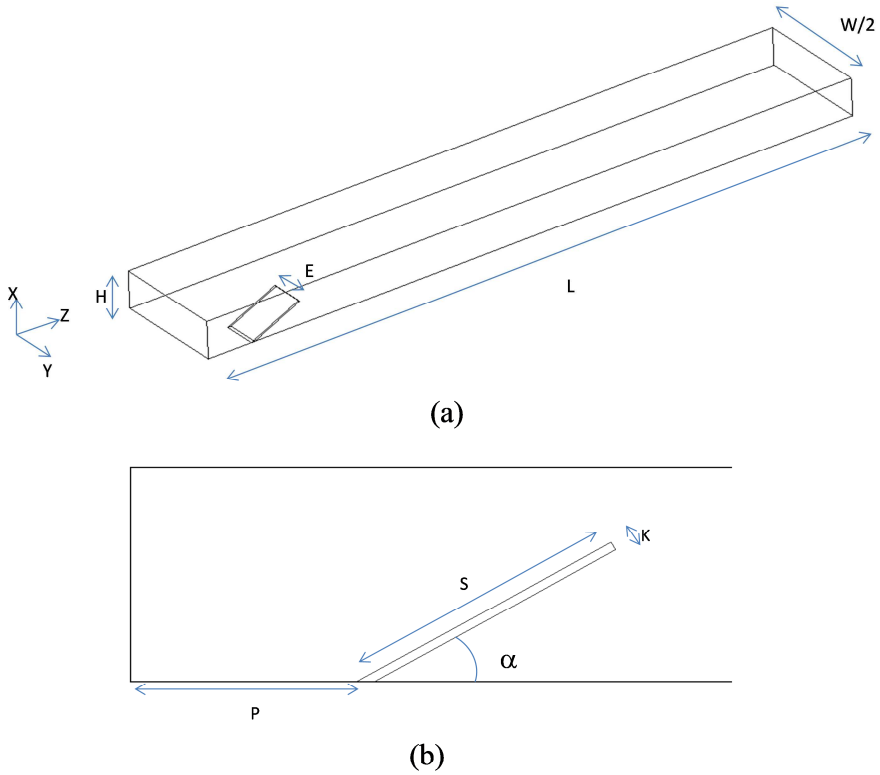

Figure 5. 1: (a) Isometric view of the computational domain, (b) side view showing the attack *angle* α.

Table 5.1: VG geometrical characteristics and computational domain dimensions.

Channel height	H	20 mm
Channel width	W	$5H$
Channel length	L	$15H$
Angle of attack	α	0°–30°
VG length	S	$1.3H$
VG width	E	$0.75H$
Distance from the inlet to VG	P	H
VG thickness	K	$0.04H$

5.3 Mesh study

A non-uniform polyhedral mesh is generated in the core of the computational domain. Near the channel walls and VG surfaces, a prism-layer refinement mesh is preferred due to the presence of high velocity, temperature and pressure gradients in these regions. An example of the mesh on a flow cross section is shown in Figure 5.2.

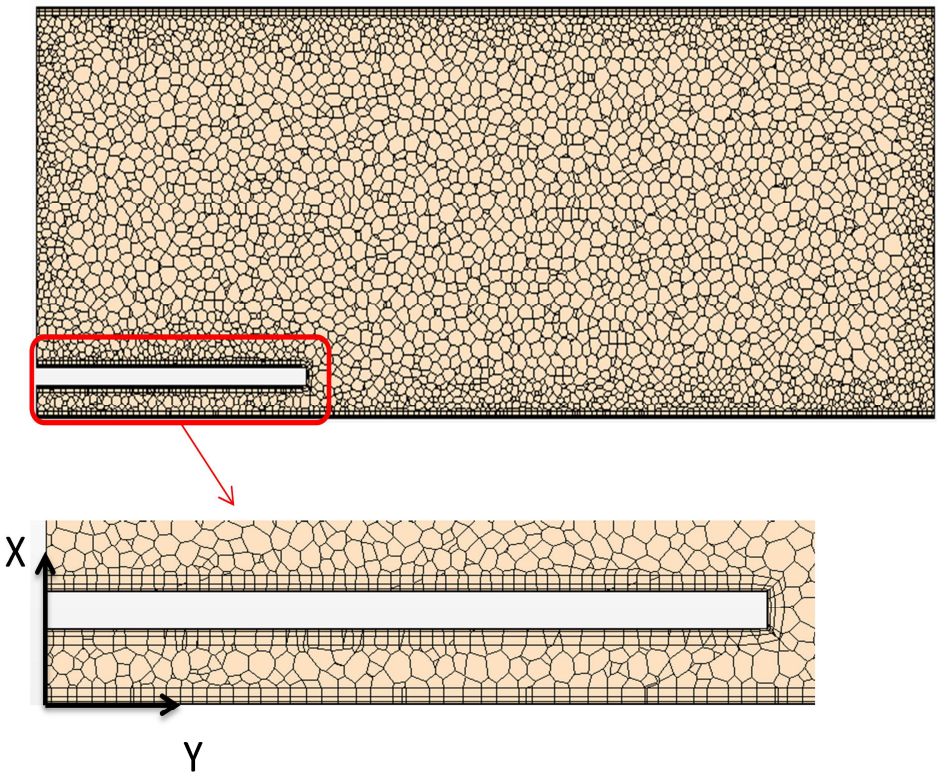

Figure 5.2: Example of the mesh on a cross section showing the refinements around the VG and near the walls for α=10° at Z=1.7 H

To determine the appropriate mesh density, the solver is run several times with increasing mesh densities until no significant effect on the results is detected, then the solution is considered to be a grid independent solution. The mesh validity verification is performed by using the method proposed by Celik *et al.* [51] who used the grid convergence index (*GCI*) and the apparent order of convergence (*c*). In the present study the mesh refinement is assessed by means

of the global Nusselt number. This dimensionless number represents the ratio of convective to conductive transfer as defined in equation (4.1).

Three different mesh densities and their features are recapitulated in Table 5. 2. The average mesh size is obtained by studying volume of each cell with respect to the total number of cells. It is desirable that the grid refinement factor value be greater than 1.3 as proposed by Celik *et al.* [41]. Based on equations (4.1) to (4.3), the Nusselt number is calculated for each mesh density then the convergence order *c* and *GCI* are computed.

Table 5. 2: Wing mesh characteristics.

Mesh	M0	M1	M2
Number of cells	703,645	1,532,441	3,289,799
Mesh size (mm)	0.354	0.273	0.212
Refinement factor	-	1.3	1.3

Hence, it is found that the uncertainty in the fine-grid solution is $GCI = 1.49\%$ and the convergence order is $c = 3.49$, which are both accepted values for which the results are considered to be grid independent. Based on the obtained values M2 is selected. For more details about the calculation of *c* and *GCI* the reader can refer to Celik *et al.* [41].

Additionally local mesh study is also performed by considering transversal probe lines located at a distance *H* downstream the wing (see Figure 5.3) on both top and bottom channel walls, where wall heat fluxes transversal profiles can be analyzed. A third probe line is created in the core flow, at the center of the channel (*H*/2) and at the same distance downstream from the wing, to enable the velocity and temperature transversal profiles analysis for each mesh density considered.

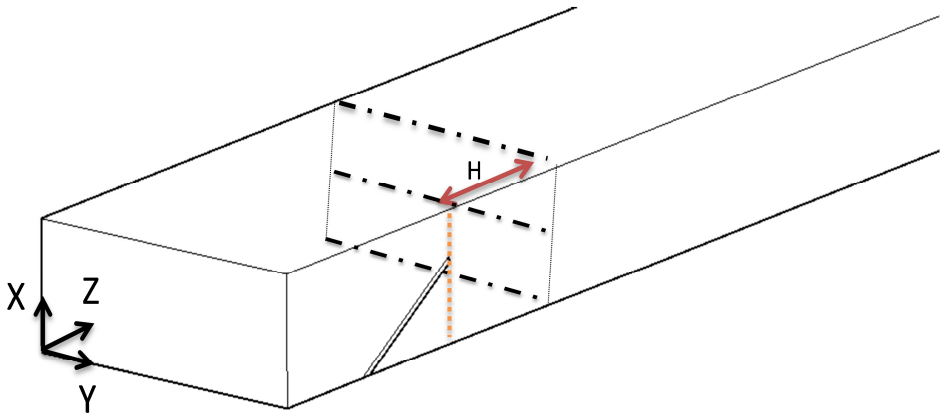

Figure 5.3: Isometric view of the computational domain showing the location of the probe lines created downstream the VG for local mesh analysis.

The local relative errors between mesh densities M1 and M2 are calculated for various variables using equations (4.5) – (4.8).

Based on the results presented in Figure 5.4, it can be seen that the relative errors between M1 and M2 mesh densities always do not exceed 2.5% insuring good accuracy of the selected mesh density. Further validation is done hereunder by comparing the present computational results to a formerly published correlation.

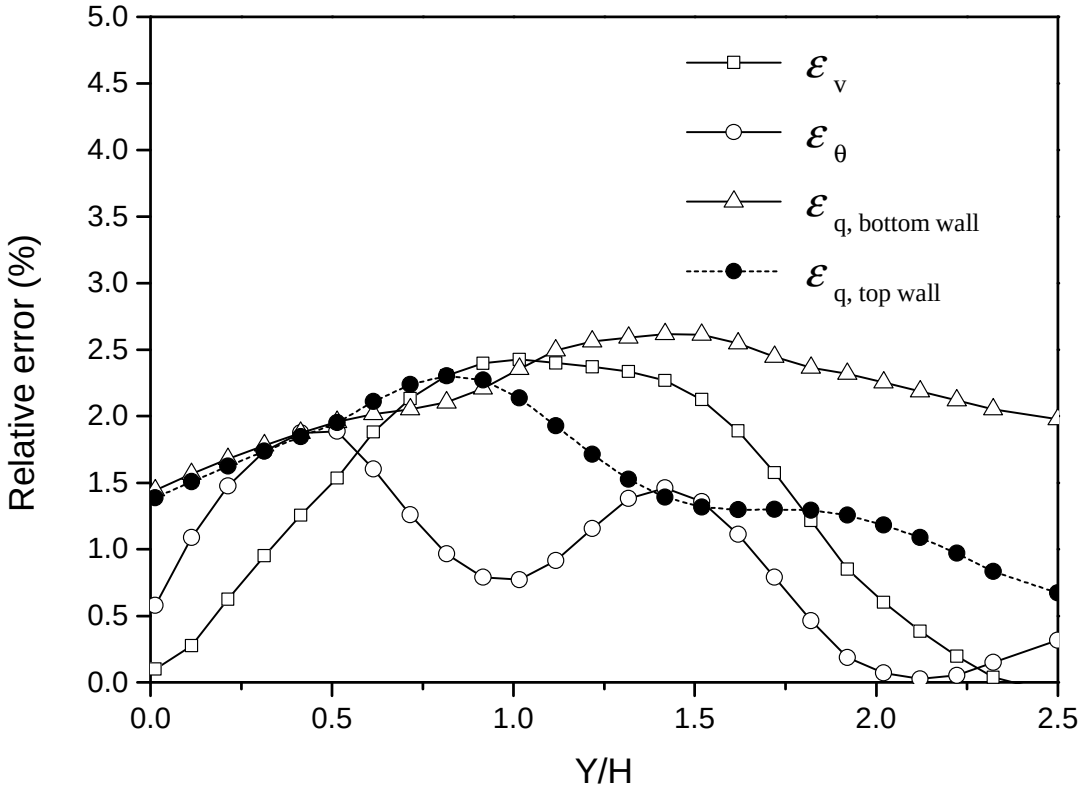

Figure 5.4: Relative local error between the meshes M1 and M2 for bottom and top wall heat fluxes, velocity and dimensionless temperature in the core flow (at mid-channel height).

5.4 Results and discussions

The major purpose of the present study is to analyze the effect of the angle of attack on the heat transfer and aeraulic performances, and then the flow topology and the temperature distribution are studied along the channel. Also investigations are done on the local and global parameters to check the effect of the angle of attack on the thermal performance enhancement.

5.4.1 Empty channel validation

Since the velocity and the temperature are set to be uniformed at the inlet of the computational domain, it is considered that the flow is a developing flow.

For thermally and hydraulically developing laminar air flow, the present numerical results are validated for local Nusselt number using Stephan correlation [62]. This correlation is valid in the range $0.1 \leq \mathrm{Pr} \leq 1000$ for parallel plate channels. The local Nusselt number is represented as followed:

$$Nu_x = 7.55 + \frac{0.024 x_*^{-1.14}(0.0179 Pr^{0.17} x_*^{-0.64} - 0.14)}{(1 + 0.0358 Pr^{0.17} x_*^{-0.64})^2} \tag{5.1}$$

with

$$x_* = \frac{x}{D_h RePr} \tag{5.2}$$

where x represents the location along the channel starting from the inlet till the outlet of it.

Based on equations (5.1) and (5.2) the local Nusselt number is calculated and compared to computational results obtained for the empty channel. Figure 5.5 represents the results, where the average percentage error is 1.87 % along the duct.

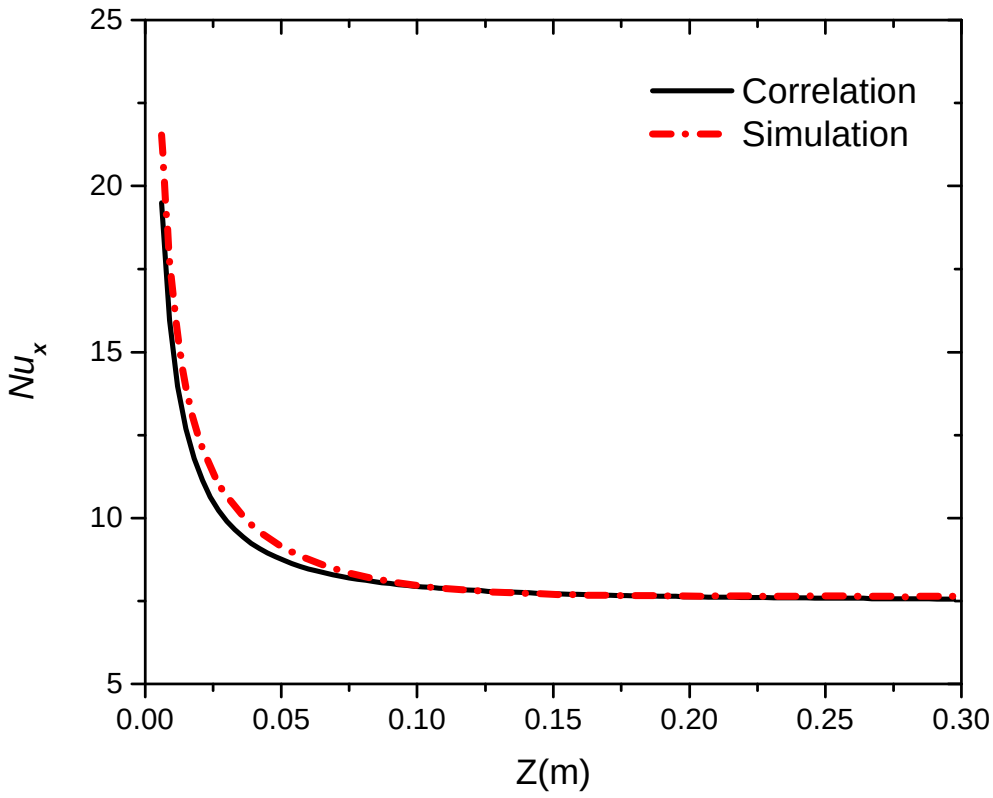

Figure 5.5: Validation for empty channel simulation

5.4.2 Flow structure and temperature distributions

In order to understand the flow behavior, its structure is first studied for two values of the angle of attack: α=10° and α=30°, for same Reynolds number *Re*=456.

Figure 5.6 represents on the one hand the helicity distribution, where helicity is the product of the velocity with value of the vorticity, and in the other hand the vorticity streamlines along the channel for different cross sections located downstream the VG, for α=10° on Figure 5.6 (a) and for α=30° on Figure 5.6 (b) By studying these two parameters, the generation of the vortices due to the VG is highlighted. Also the intensity of the vortex and its location along the channel is studied by taking different planes. Z=2.5H represents the plane just after the VG, where the vortices are generated due to the presence of high velocity gradients. As shown in Figure 5.6, rotating vortices are generated downstream from the VG. At Z=2.5H there is a negative values of helicity, due to the reverse vortices generated by the VG and their effect is detected till the end of the channel.

By comparing α=10° and α=30°, it is clear that how the angle of attack α effects on the generation of the vortices and their effect on the flow topology along the channel. For α=30°, the generated vortices are more intense than that of α=10°, also at Z=5H an induced secondary vortex is detected for the case of α=30°.

As the angle of attack α increases, it is clear that the effect of the vortices generated last longer along the channel, until location of Z=15H which represents almost the outlet of the channel. For the case α=10° at Z=15H, the effect of the VG starts to fade away which is supported by both the streamlines and the helicity contours. On the other hand, for the case of α=30° at Z=15H, the effect of the generated vortices is dominant till the end channel.

Z/H	α=10° Streamlines	α=10° Helicity
2.5	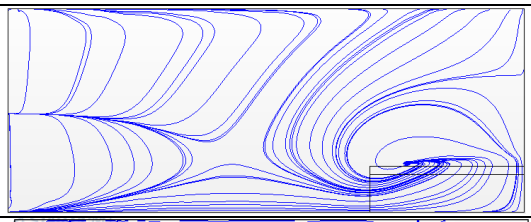	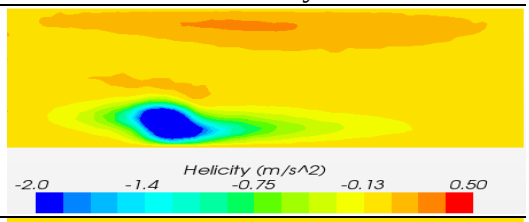
5	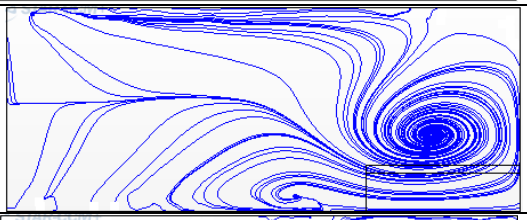	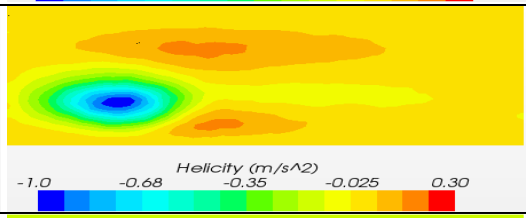
7.5	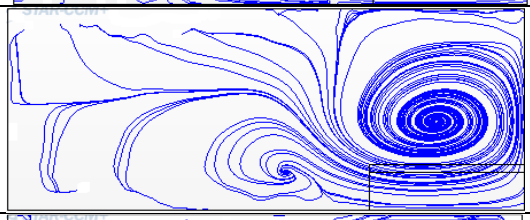	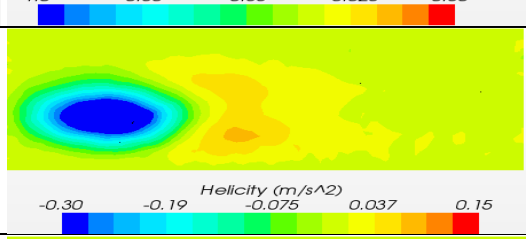
10	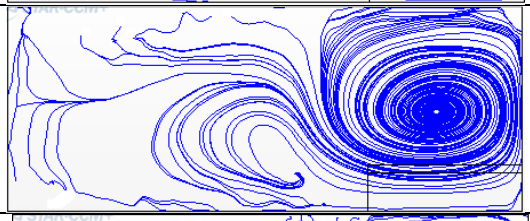	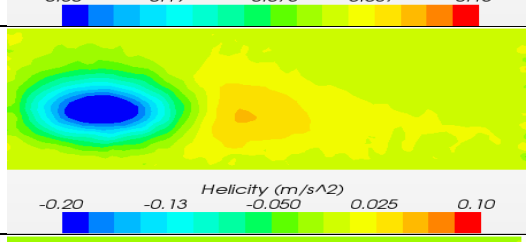
12.5	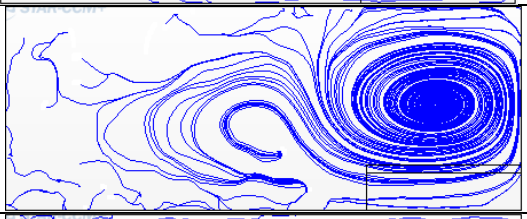	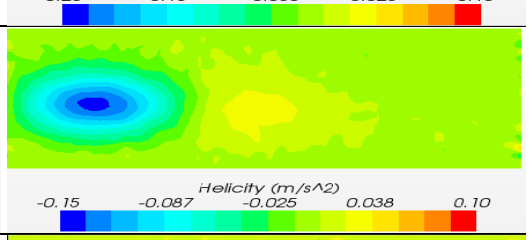
15	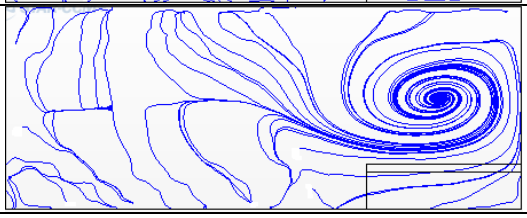	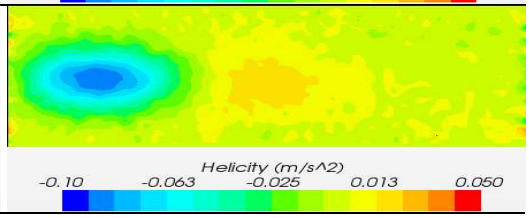

(a)

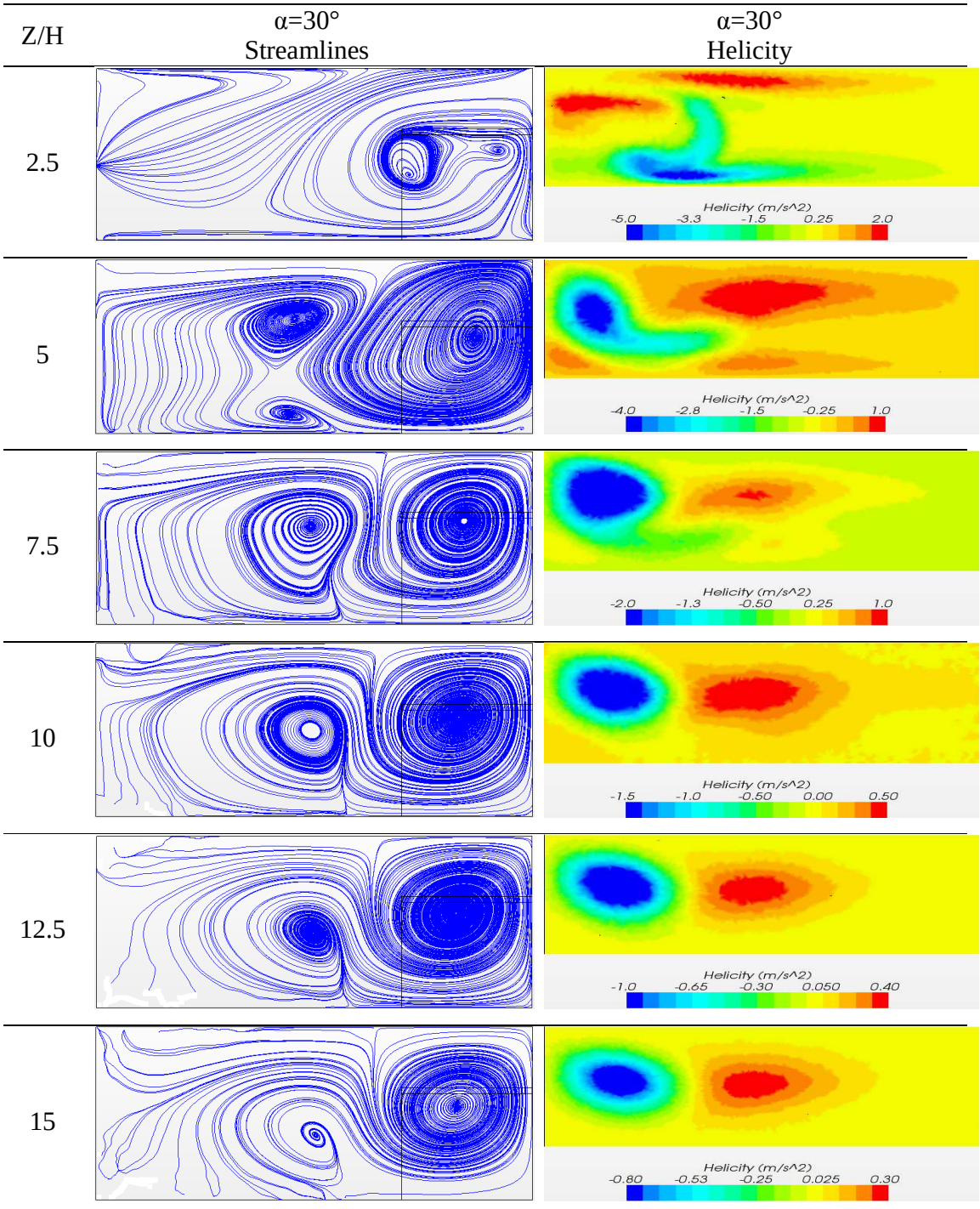

(b)

Figure 5.6: Helicity distribution (right side) and streamlines (left side) for *Re*=456 at locations *Z*/*H* in the range [2.5–15], for (a) α=10°, (b) α=30°

In Figure 5.7 the temperature distribution is represented for different flow cross sections at locations Z/H in the range [2.5–15] and for α=10° and 30°. It illustrates that the streamwise vortices previously mentioned affect the temperature distribution downstream the VG, especially for the highest angle. Indeed, in the common flow down region, between the two main vortices (i.e. in the symmetry plane of the RW), hot fluid particles are ejected from the top wall towards the flow core due to upwash effect, while the thickness of the thermal boundary layer on the bottom wall is found to decrease due to downwash effect. In the common flow up region (i.e. between two neighboring vortex pairs) the upwash effect ejects near-wall hot fluid from the bottom wall towards the flow core. This mixing process and thermal boundary thinning are clearly seen for the highest attack angle value, due to the fact that the vortices are more energetic and cover larger area in the flow cross section. Then, the heat transfer enhancement seems to be dependent of the wing attack angle value. This is assessed quantitatively and discussed in the next sections by representing the streamwise development of the Nusselt number and the vorticity strength.

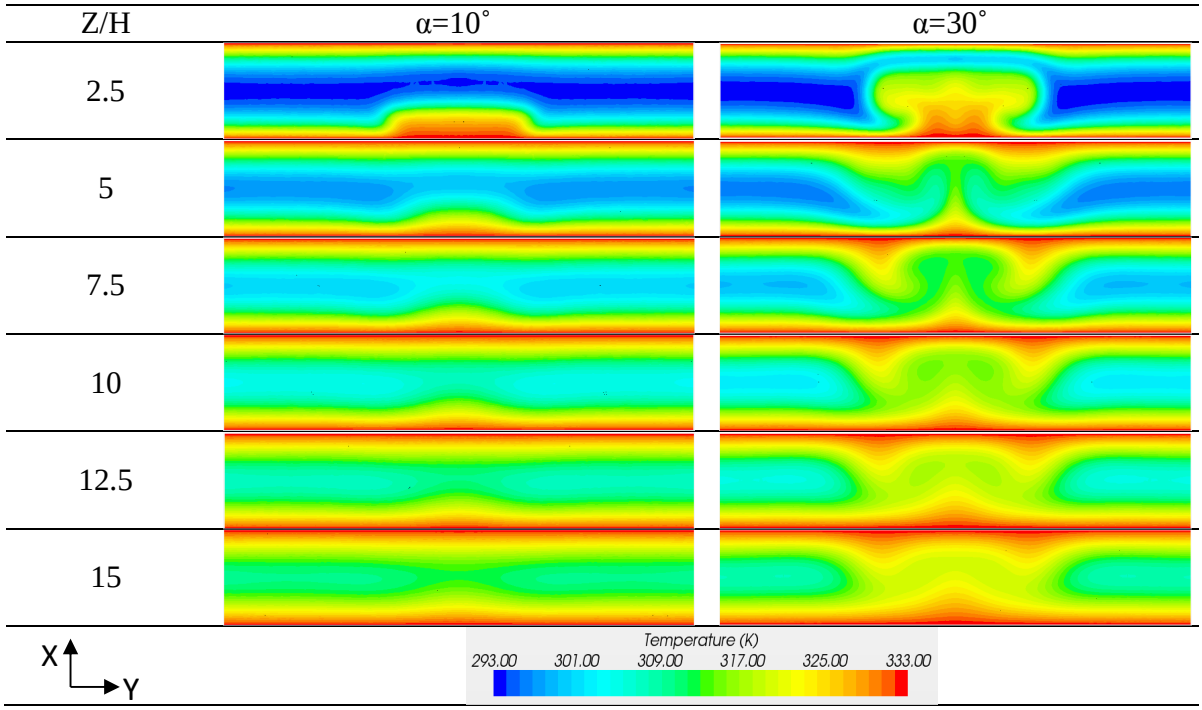

Figure 5.7: Temperature distribution for *Re*=456 on different flow cross sections at locations *Z*/*H* in the range [2.5–15], for α=10° (left side) and α=30° (right side)

The streamwise variation of the area-weighted span-averaged helicity is represented in Figure 5.8, where the dashed vertical lines represent the head (Z=1.2*H)* and the tail (2*H*<Z<2.4*H*) of the VG.

It is observed that the helicity values start to decrease at the entrance of the channel reaching even negative values at a position just upstream the VG. The negative values are obtained due to the direction of the rotation of the main vortex. Downstream the flow encounters the VG, the averaged helicity is found to increase and reach its maximum value in the very near vicinity of the VG trailing edge because of the generated vortices, for location *Z* between 2*H* and 3*H*. It can be noticed that the helicity peak for the case α=30° is about 6 times higher than that for α=10° due to higher energetic vortices.

For α=10° and α=15° the profile of the streamwise evolution of the vorticity is similar having a maximum at the VG tail and decreasing continuously along the channel because of the dissipation of the longitudinal vortices. Whereas for higher α values (20°, 25° and 30°),

secondary peaks are generated downstream from the first one due to the induced vortices generated. It is interesting to note that the higher the angle of attack, the higher the primary generated peak and also the higher the secondary peaks. However, at a distance from the secondary peak, for the case α=20° the helicity sustains a higher value, from Z=6.5H compared to α=30°. For the case α=25°, the value of the secondary generated peak is almost the same as that of the case α=30° and the helicity continuous to exhibit higher values along the channel compared to the other cases.

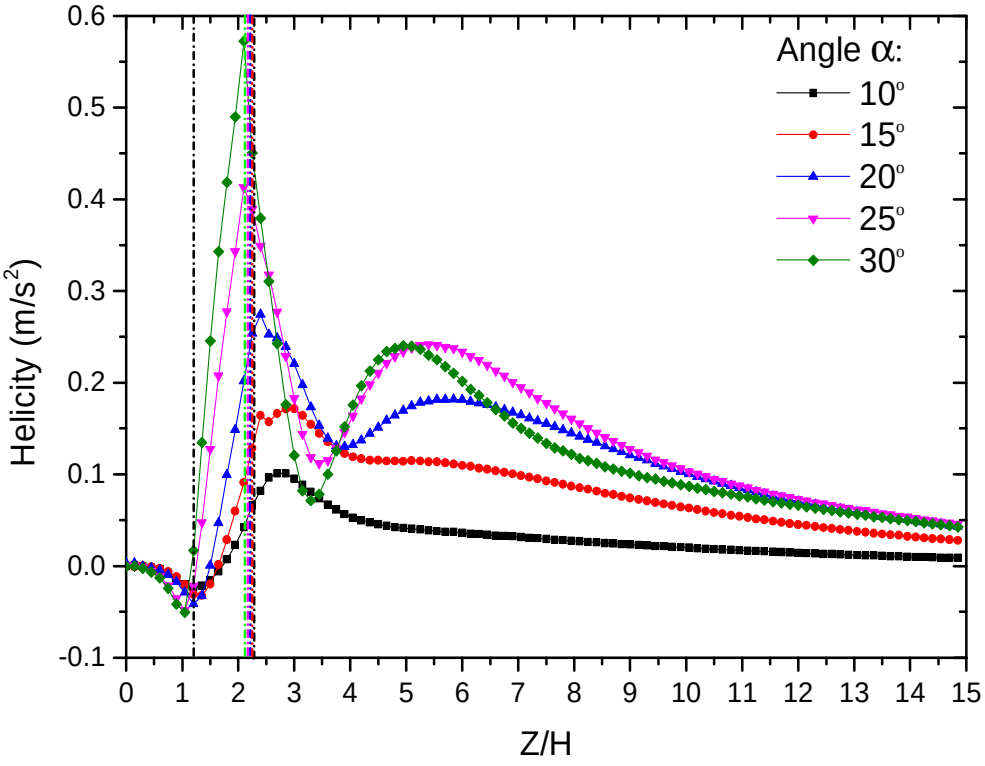

Figure 5.8:Variation of span-averaged helicity along the parallel plate for *Re*=456

In Figure 5.9 the streamwise variation of the dimensionless location of the main vortex is presented; it corresponds to the distance between the vortex core and the bottom wall. The

position of the core of the main vortex starts in an increasing profile for all the values of attack angle just after the VG tail at Z=2.5*H*. It is observed that by increasing the value of attack angle α, the position of the main vortex along the channel increases rapidly. For the cases $\alpha<25°$, the position of the main vortex core increases gradually along the channel, until reaching values for *X* around 0.50*H*. It is interesting to note that for $\alpha=30°$ the location of the core of the main vortex reaches a maximum value *X*=0.65*H* at the location *Z*=7.5*H* and then decreases to *X*=0.55*H* at the channel output.

As the dimensionless location of the core of the main vortex reaches around the half of the channel height, it leads to a better mixing of the fluid in the channel. It mixes the hot particles located in the vicinity of both lower and upper boundaries with that of the central ones having a lower temperature values. As a result, the heat transfer rate increases, due to the high temperature gradient and then the Nusselt number. The variation in the Nusselt number is then studied in the next sections, in order to improve the comprehension of the effect of the angle of attack α on the heat transfer enhancement.

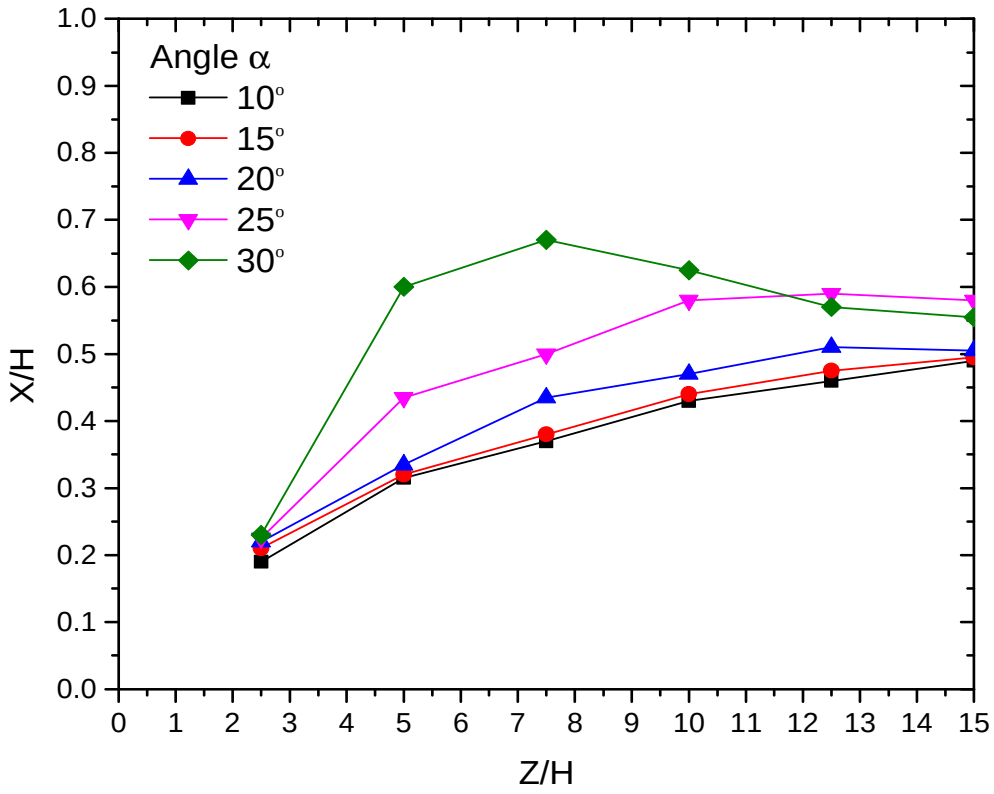

Figure 5.9: Dimensionless location of the main vortex along the channel for *Re*=456

5.4.3 Local performances

The streamwise distribution of the span-averaged Nusselt number at the bottom wall is plotted on Figure 5.10(a) for values of attack angles α in the range [10°–30°] as well as for the case of the empty channel, simulated with the same operating conditions except the VG which is removed. At the inlet of the channel, the values of *Nu* starts to decrease until the location Z=1.2H which represents the beginning location of the VG. From this location, the Nusselt number value starts to increase due to the heat transfer enhancement as a result of the generated vortices until it reaches the VG tail. Further downstream, for all the simulated cases, the Nusselt value drops to a minimum value, at a location of Z=1.2H which represents the beginning location of the VG, and this minimum value is found to be even below the empty channel case, for the cases α in the range [10°–20°]. For low values of α [10°–20°], the area under the VG is greater than that of the higher angles. As a result of this, a dead zone is created with zero velocity leading to a drop in the convective heat transfer thus drop in the Nusselt number. Downstream the VG, the Nusselt number increases until attains a second peak at locations Z in the range [3.5H–5H]. For all the values of α, a similar profile is obtained where after the second peak the Nusselt number decreases along the longitudinal direction of the channel. However, the higher the angle of attack, the higher the Nusselt number.

Figure 5.10(b) represents the streamwise distribution of the span-averaged Nusselt number at the top wall, plotted for values of attack angles α in the range [10°–30°] and for the case of the empty channel. The Nusselt number for the top wall starts to decrease in the inlet of the channel and at the location Z=1.2H, the value starts to increase reaching its maximum at Z=2.3H for all values of α except that of α=10° which continues to decrease smoothly along the longitudinal direction of the channel. The higher the angle of attack, the higher the Nusselt number peak. The drop in the Nusselt number curve below the value of the empty channel also occurs on the top wall for the cases of α=20°, 25° and 30°. It occurs for α=20° at Z=9H, α=25° at Z=6H and α=30° at Z=5H. This behavior is explained in the next section.

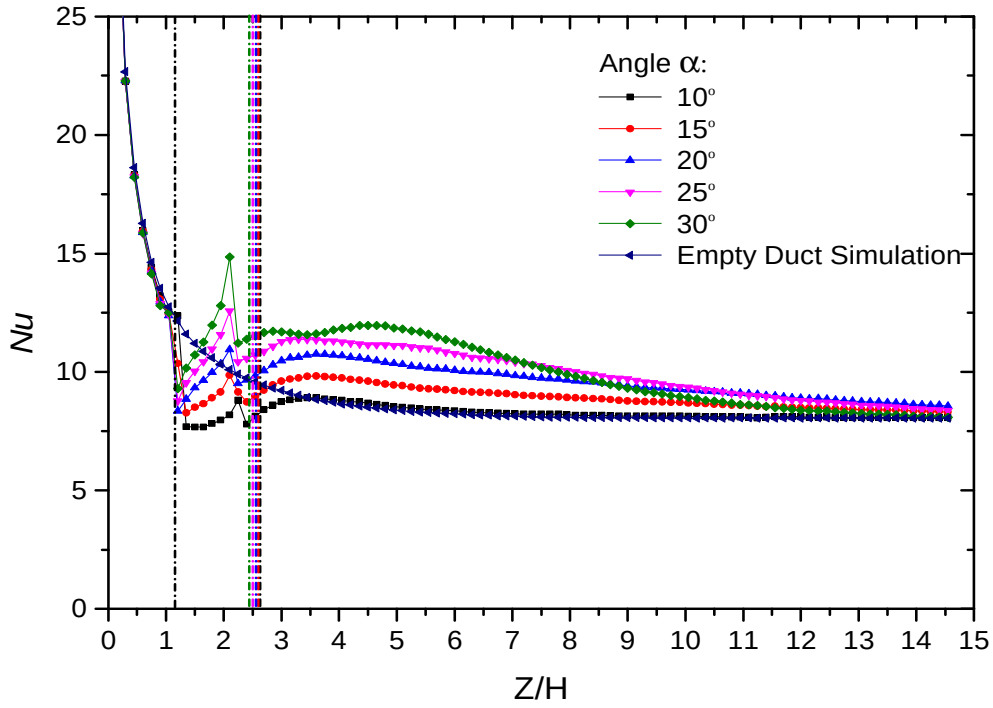

(a)

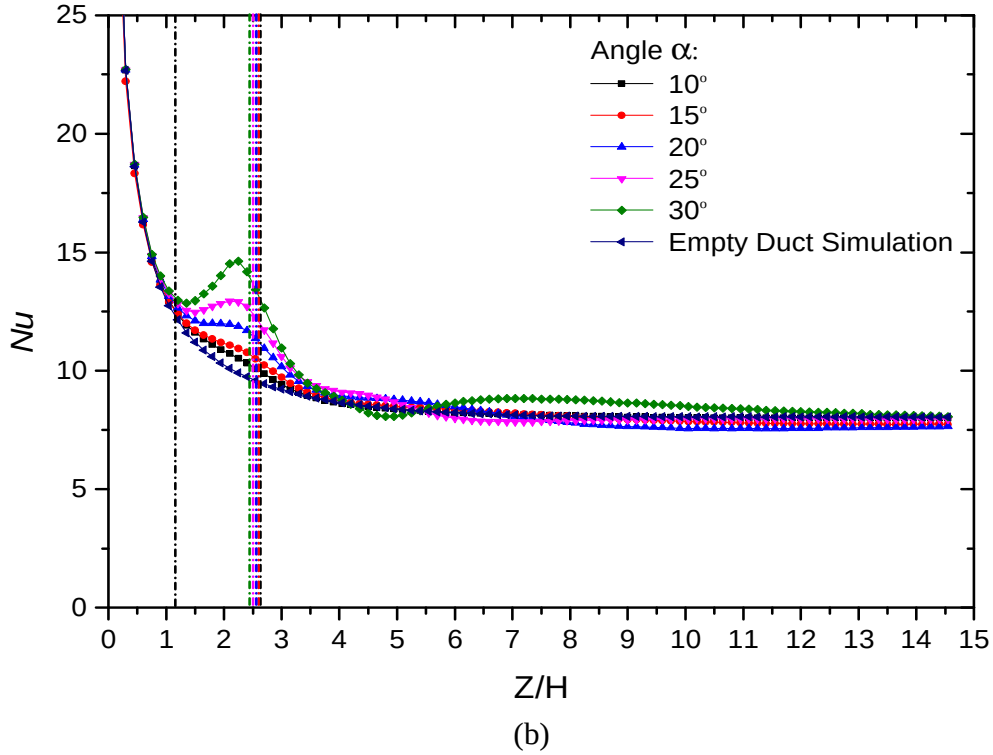

(b)

Figure 5.10: Nusselt number for *Re*=456 at (a) bottom wall, (b) top wall

To understand the drop of the Nusselt number in some cases of channel equipped with VG below the results of empty channel, a study is done to check the near-wall velocity distributions. In Figure 5.11, the near wall velocity is studied for the values of α in the range [10°–30°] at two locations: X=*H*/10, i.e. a plane parallel to the bottom plan located at a small distance (*H*/10), knowing that X=0 represents the bottom wall. Another plane of investigation is defined at X=9*H*/10 away from the bottom wall. The velocity value for the case X=*H*/10 at a position under the VG highlighted by a black circle is zero: a dead zone is being created under the VG where due to zero velocity there will be negligible convective heat transfer. As a result the Nusselt number at that location is dropping even below the empty channel. On the other hand, for the case X=9*H*/10, for α=20°, 25° and 30°, very low values of velocity is detected on the near top wall too. As a result, for α=20°, 25° and 30° it appears very weak convective heat transfer on the top wall at the positions highlighted by a circle. This is supported by the values of the Nusselt number that are represented in Figure 5.10 for the top wall case.

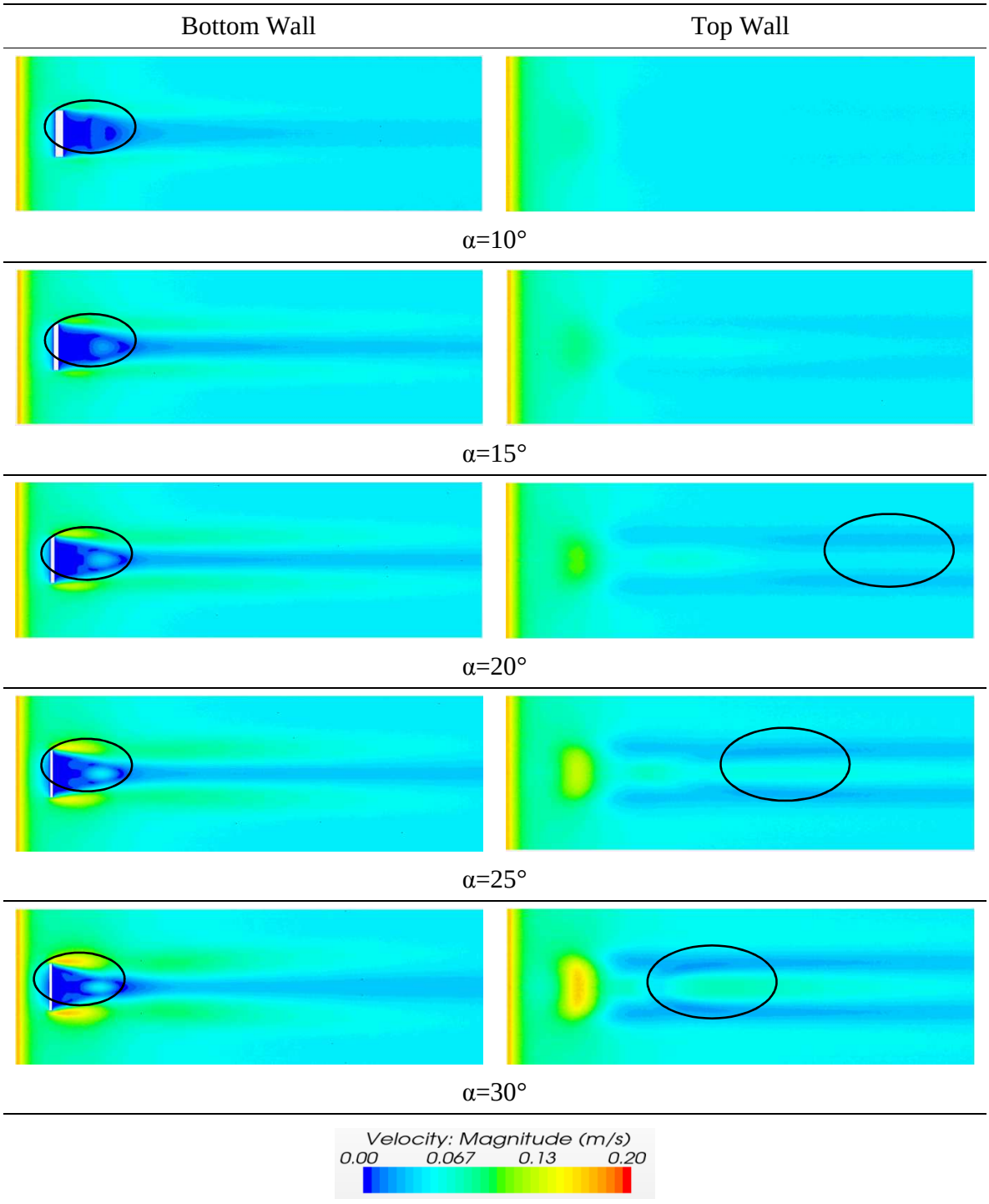

Figure 5.11: Velocity magnitude contours at location $X=H/10$ away from bottom wall (left side) and top wall (right side) for Re=456.

To evaluate the pressure losses induced by the VG, Fanning friction factor *f* is calculated from the pressure gradient obtained from the simulation. Darcy's friction can be represented by equation (4.14) and (4.15).

In Figure 5.12, the streamwise variation of the friction factor is represented. The profile of the curve is similar in all the cases. It starts to drop along the length of the channel until it reaches the VG leading edge. At that point, a gradual increase starts to appear reaching its maximum value at the VG tail of the VG, downstream which the curve continues to drop making an asymptote with the empty channel curve. From the leading edge of the VG, the higher the angle of attack, the higher the friction factor.

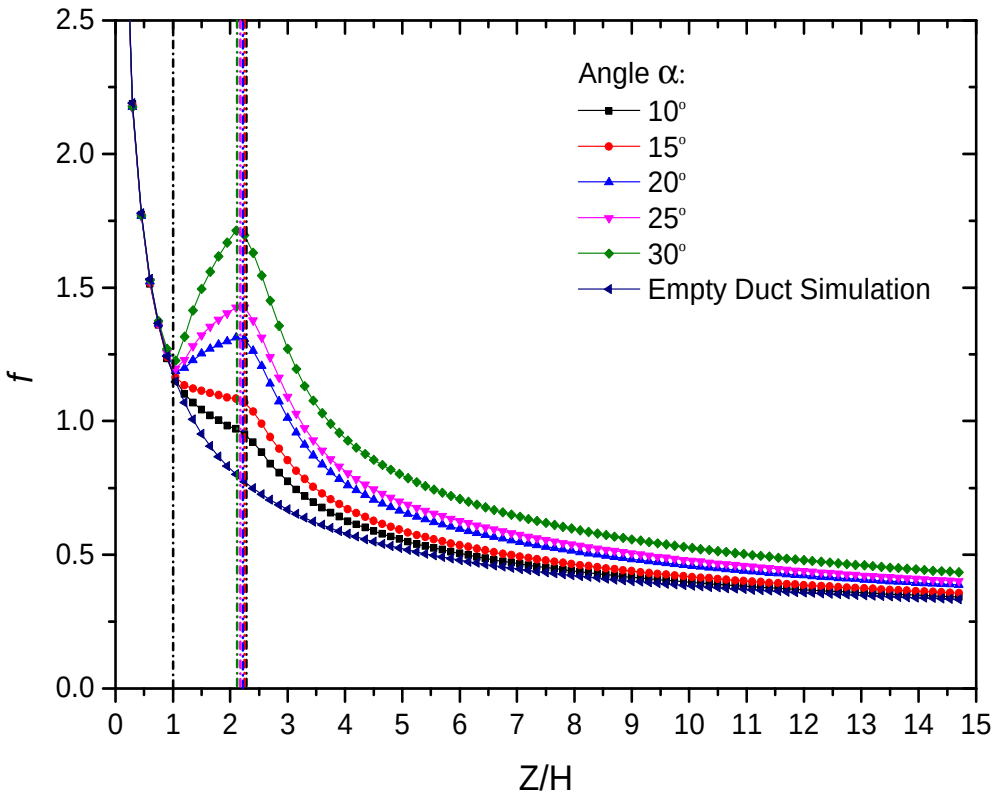

Figure 5.12: Friction factor streamwise variation for *Re*=456

5.4.4 Global performances

In order to study the global effect of the angle of attack α of the VG on the enhancement of the heat transfer, global values of the Nusselt number, the friction factor and the thermal enhancement factor are presented and discussed in this section.

Figure 5.12 represents the global Nusselt number plotted versus angle of attack α. The Nusselt number is calculated using equation (4.1). The Nusselt number is found to monotonically increase with the value of the angle of attack. By comparing the empty channel and α=10°, there is an increase of about 1% in the Nusselt number, on the other hand for α=30° this increase reaches to a value of 10%.

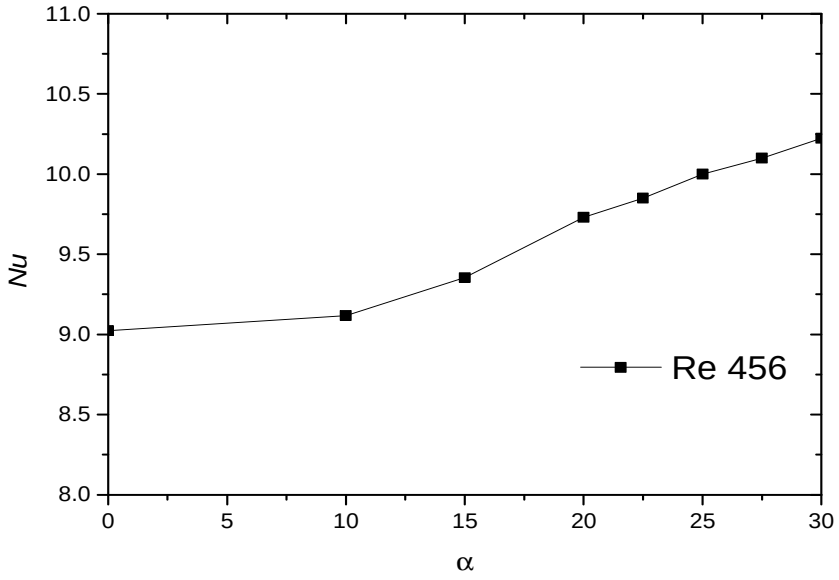

Figure 5.13: Global Nusselt number for *Re*=456.

The global friction factor is plotted versus the angle of attack in Figure 5.14. The friction factor is calculated using equation (4.15). As the angle of attack α increases, the friction factor increases too. For higher values of angle α the pressure drop is increased, as a result the pressure gradient is increased leading to higher values of friction factor. This increase reaches a value of 30% by comparing the empty channel with respect to that of α=30°.

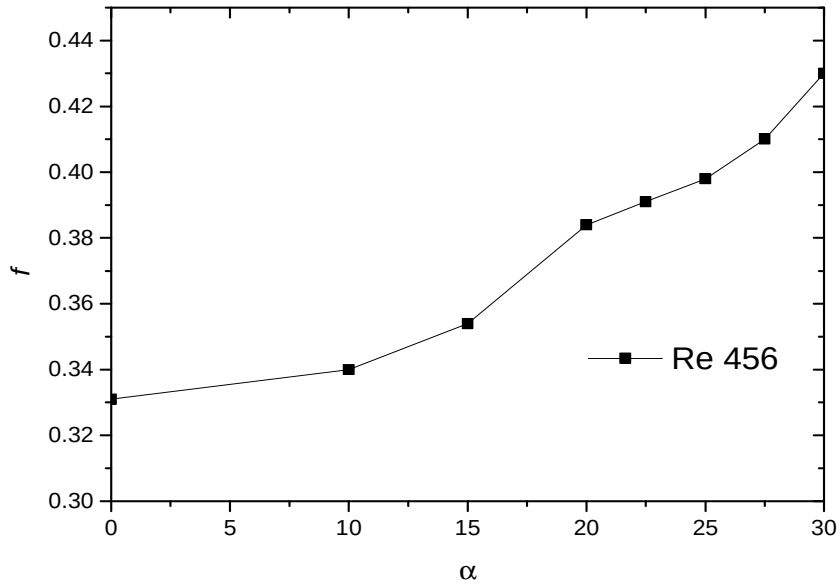

Figure 5.14: Global friction factor for *Re*=456.

Figure 5. 15 represents the thermal enhancement factor versus the angle of attack based on the previously mentioned relation in equation (4.17). The value of the thermal enhancement factor starts to increase with the increase of the angle of attack α. For values of α=10° and α=15°, there is a linear increase reaching a value of 1.012 representing 1.2% of enhancement. For α=20°, there is an increase in the thermal enhancement factor reaching its maximum value of 1.043 representing 4.3% of enhancement for the case α=25°, beyond which the enhancement factor slightly drops. This increase in the enhancement is supported by the helicity curve represented in Figure 5.6, where secondary peaks are generated for $20° \leq \alpha \leq 30°$.

Thus it can be considered that for the operating condition *Re*=456, the optimum angle of attack providing the best thermal enhancement is 25° and not the highest angle, this is supported by the helicity study which have shown the detected secondary vortices in Figure 5.8 where the curve of α=25° sustains higher values along the channel compared to the other tested angles.

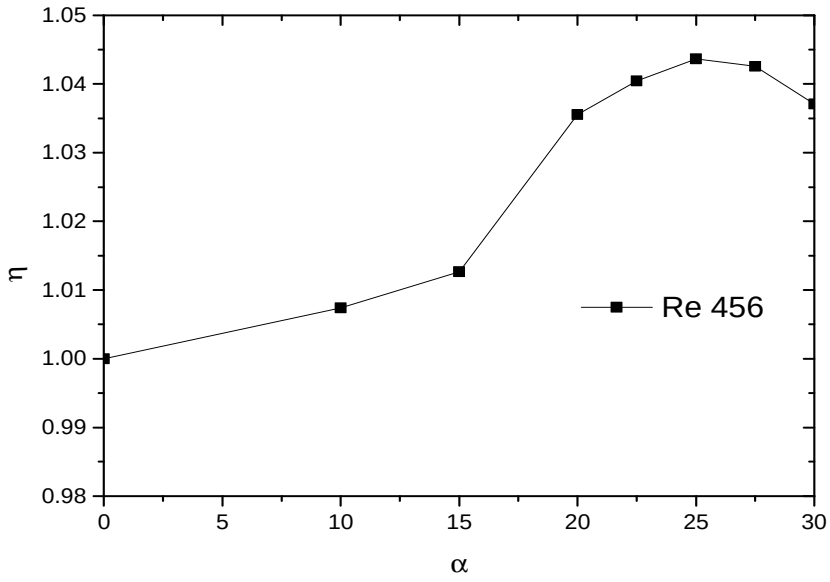

Figure 5. 15: Thermal enhancement factor for *Re*=456.

5.5 Conclusion

In this study, the heat transfer and fluid flow behavior in a parallel plate channel with rectangular wing vortex generator (RWVG) inserted on the bottom wall is numerically investigated. For different values of angle of attack α, both the local and the global parameters are calculated and studied to figure out the effect of the angle of attack on the heat transfer enhancement. The main outcomes of this study can be summarized as followed.

First, for high values of angle of attack (close to α=30°), the generated vortices get wider and more energetic along the longitudinal direction compared to low values (i.e. α=10°).

Second, it is observed that the helicity increases just after the flow encounters the VG where the vortices are first formed. The helicity peak for α=30° is about 6 folds higher than that for α=10° meaning higher energetic vortices.

Third, it is observed that for α in the range [10°–25°], the dimensionless vertical position X/H of the main vortex starts at low position and increases along the channel until it reaches a

maximum value at the outlet of the channel (Z=15H) around X=0.5H representing the middle of the channel, for the case α=25°, it reaches a maximum value of X=0.58H. On the other hand, for the case α=30°, the dimensionless X/H position reaches a maximum value of X=0.68H before the outlet channel and then drops back to attain 0.55H at the end of the channel.

Finally, the thermal enhancement factor starts to increase with the angle of attack until it reaches a maximum value of 1.043 representing 4.3% of enhancement at α=25°, beyond which its value decreases. It can be considered that the optimum angle of attack of the vortex generator which leads to the best enhancement under these operating conditions is 25° and not the highest angle.

CHAPTER 6

Fluid Solid Interaction

6.1 Introduction

A flexible solid structure contacting a flowing fluid is subjected to a pressure which may cause deformation in the structure. As a return, the deformed structure alters the flow field. The altered flowing fluid, in turn, exerts another form of pressure on the structure with repeats of the process. This kind of interaction is called Fluid-Structure Interaction (FSI). An example of the FSI system is the air flow around an airplane wing causing the wing to vibrate and even deform. Because of the deformation of the wing the air pattern around the wing is modified. [64]

In 1828, the concept of hydrodynamic mass was proposed first by Friedrich Bessel who investigated the motion of the pendulum in a fluid. In 1843 Stokes performed a study on the uniform acceleration of an infinite cylinder moving in an infinite fluid medium and concluded that the effective mass of the cylinder moving in the fluid increased because of surrounding fluid by the amount of hydrodynamic mass equal to the mass of fluid it displaced. It was known that this finding produced the concept of fluid-structure interaction. In the 1960s, some designers of nuclear reactor systems found that the hydrodynamic mass of a structure in a confined fluid medium resulting from the fluid-structure interaction was much larger than that for the structure in an infinite fluid medium, which was equal to the mass of fluid displaced by the structure.

Nowadays, various techniques for numerically simulating the strongly coupled fluid-structure systems are under development as the Computational Fluid Dynamic (CFD) analysis technique evolves rapidly. [64]

6.2 Numerical simulation of FSI 2D validation

The benchmark configuration proposed by Turek and Hron [8] has been chosen for the present FSI model validation. The configuration consists of a laminar incompressible 2D channel flow around an elastic beam attached to a fixed cylinder. Under the unsteady effect of the hydrodynamic forces imposed by the flow around the cylinder, self-sustained oscillations are

induced to the structure. A sketch of the computational domain is given in Figure 6.1. The domain has an inlet with a laminar parabolic velocity profile, a zero-pressure condition at the outlet, and no slip boundary conditions at the walls. The 2D channel has a length of 2500 mm and a height of 410 mm. The circular cylinder has a radius of 50 mm and is slightly shifted from the horizontal middle line to produce a non-symmetrical flow. The flexible structure has a length of 350 mm and a thickness of 20 mm. The axis origin is taken at the tip of the flap from its initial position.

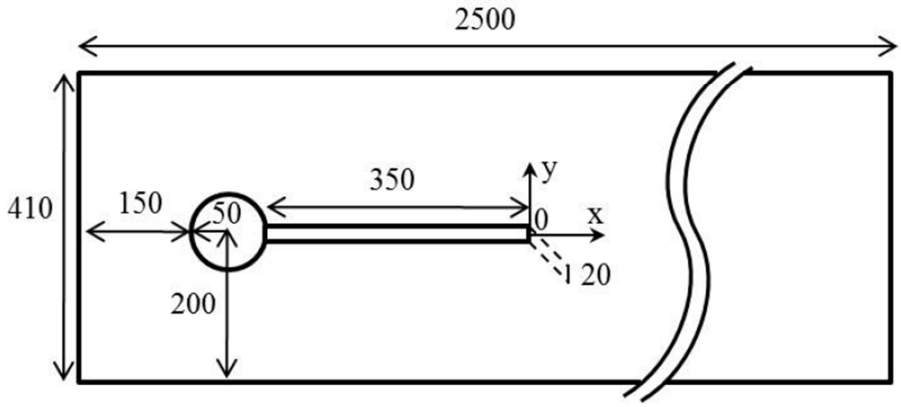

Figure 6.1: Schematic view of the computational domain used as benchmark (dimensions are in mm)

Three different configurations are investigated and described in Turek and Hron [8] depending on the flow velocity, the shear modulus and density of the moving elastic beam. The second configuration case (cited as FSI2 in Table 12 in [8]) is retained for benchmark since the flap motion shows the largest displacements. The corresponding physical quantities are summarized in Table 6.1.

Table 6.1: Physical properties of FSI2 numerical computation [8]

Parameter	$\rho_s[kg/m^3]$	ν_s	E[Pa]	$\rho_f[kg/m^3]$	$\nu_f[m^2/s]$	$U_{max}[m/s]$
FSI2	10,000	0.4	1.4×10^6	1,000	0.001	1.5

The fluid domain is discretized with 43,000 triangular cells and the mesh is refined near the walls and the fluid-structure interface, i.e. the elastic beam. The moving structural domain consists of 400 quadrilateral cells. In this simulation, a maximum number of 7 FSI outer iterations were needed to attain convergence criteria of 10^{-4} for both displacements and forces on the fluid-structure interface. To avoid divergence problems especially caused by negative cell volumes, the mesh solver uses in this numerical validation the 2.5D surface remeshing that applies on wedge/prism cells extruded from triangular surface elements. This method agglomerates cells that violate the skewness or size criteria and locally remeshes the agglomerated cells or faces. If the new cells or faces satisfy the skewness criterion, the mesh is locally updated with the new cells (with the solution interpolated from the old cells) [52]. Otherwise, the new cells are discarded, and the old cells are retained. In the present numerical validation, a maximum cell skewness of 0.7 has been used for remeshing with cell size criterion depending on the minimum and maximum length scale of the mesh. The effect of remeshing especially at high deflections is shown in Figure 6.2 at the trailing edge of the elastic beam where the cells undergo cyclic expansion and compression, thus the remeshing algorithm always preserves a decent quality of the mesh. An under-relaxation factor for both displacements and forces is set to unity and highlights a good stability and robustness of the model. The pressure-velocity coupling is established using the coupled algorithm [52], which solves the momentum and pressure-based continuity equations together. The convergence criteria for pressure and velocity is set to 10^{-6}. The Laplace mesh smoothing convergence criteria is set to 10^{-4} using a diffusion-based smoothing with a diffusion coefficient $\alpha = 1.5$ which causes the cells far from the fluid-solid interface to absorb much of the motion. Temporal discretization is performed using a first order implicit scheme and the time step is set to 10^{-4} sec. In an explicit time, integration scheme, the time step is conditionally stable and limited by the courant number which is defined by:

$$CFL = \frac{U_f \Delta_t}{\Delta_x} \leq CFL_{max} \tag{6.1}$$

where Δ_t is the time step, Δ_x is the size interval between two adjacent cells and CFL_{max} is typically chosen to be equal to unity when using explicit time stepping to achieve numerical stability.

However, the fully implicit first order scheme is unconditionally stable with respect to the time step value. Nevertheless, the CFL based on the time step size of 10^{-4} seconds and the minimum cell distance remains always less than unity.

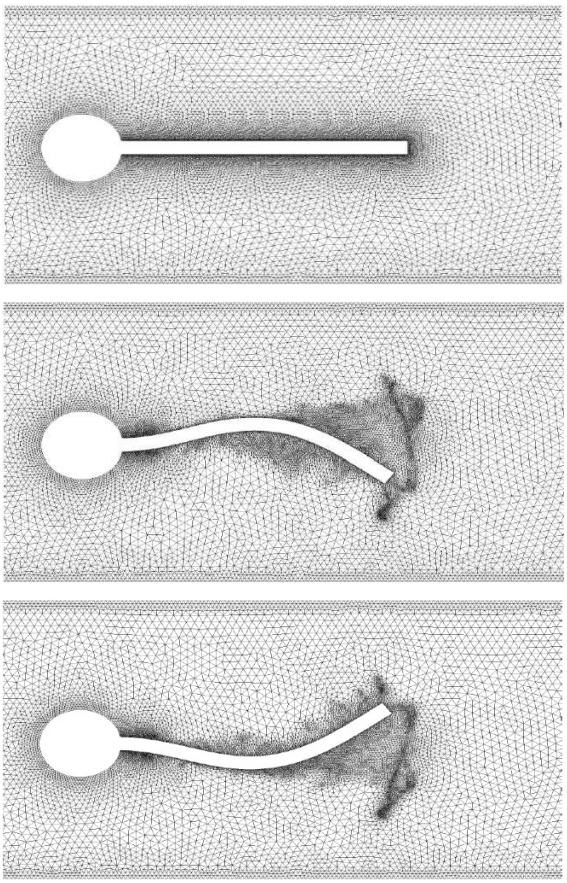

Figure 6.2: Dynamic mesh motion with remeshing

The displacement at the tip of the elastic beam in y direction is shown in Figure 6.3. After a 7 seconds transient state, the beam shows harmonic oscillations at constant frequency and amplitude. The vortex shedding from the upstream cylinder induces alternating forces on each side of the elastic beam that cause a periodic flapping motion as shown in Figure 6.4.

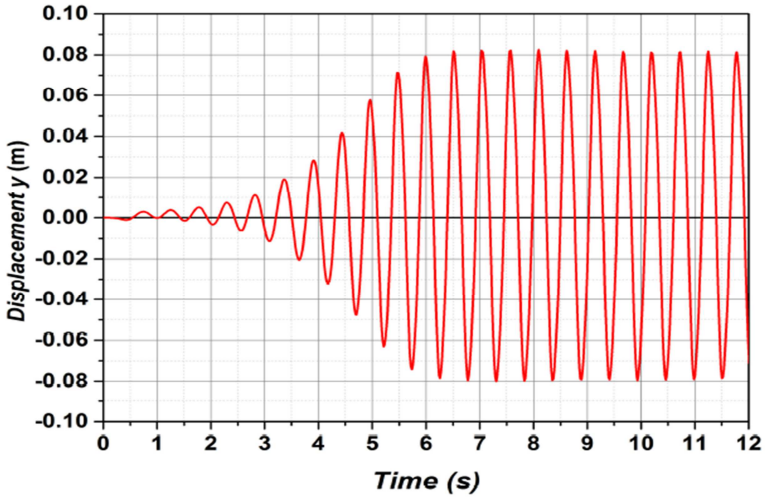

Figure 6.3: Displacement of the flap tip measured in the y direction for the numerical simulation proposed as a validation test case FSI2

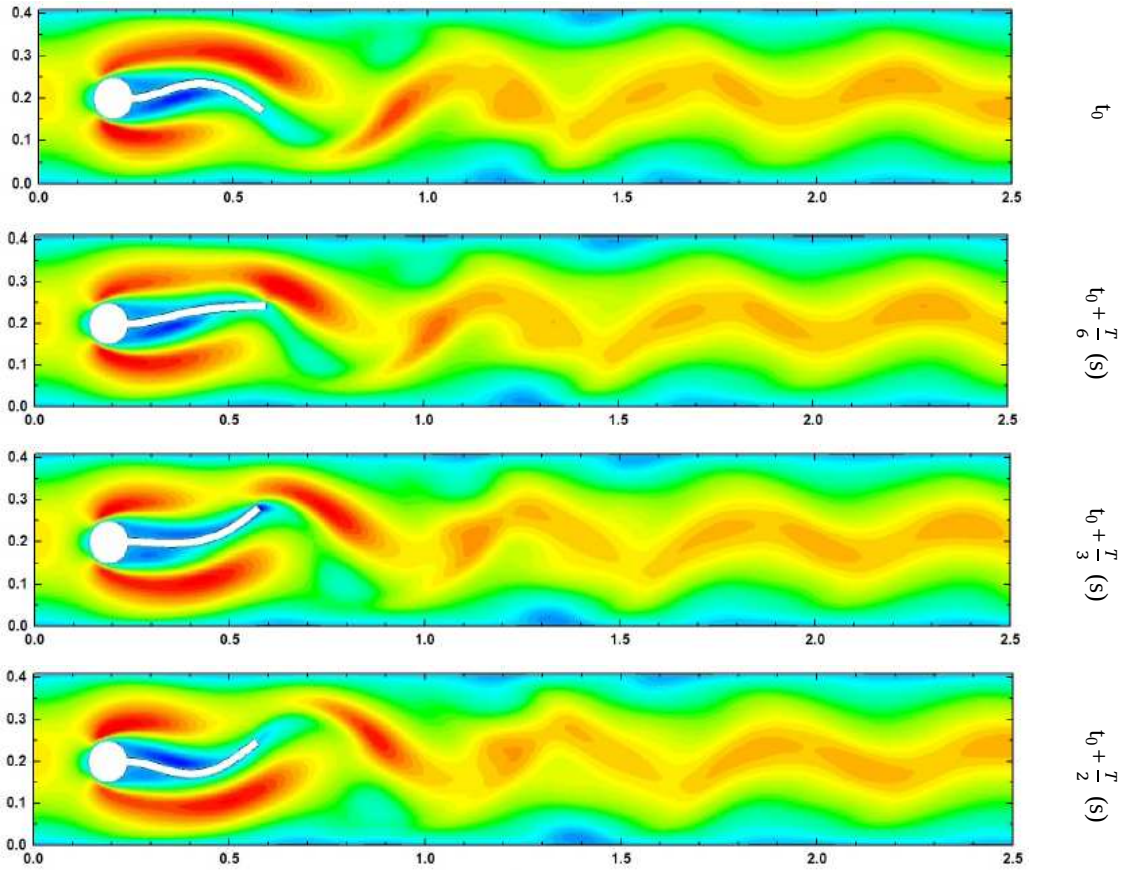

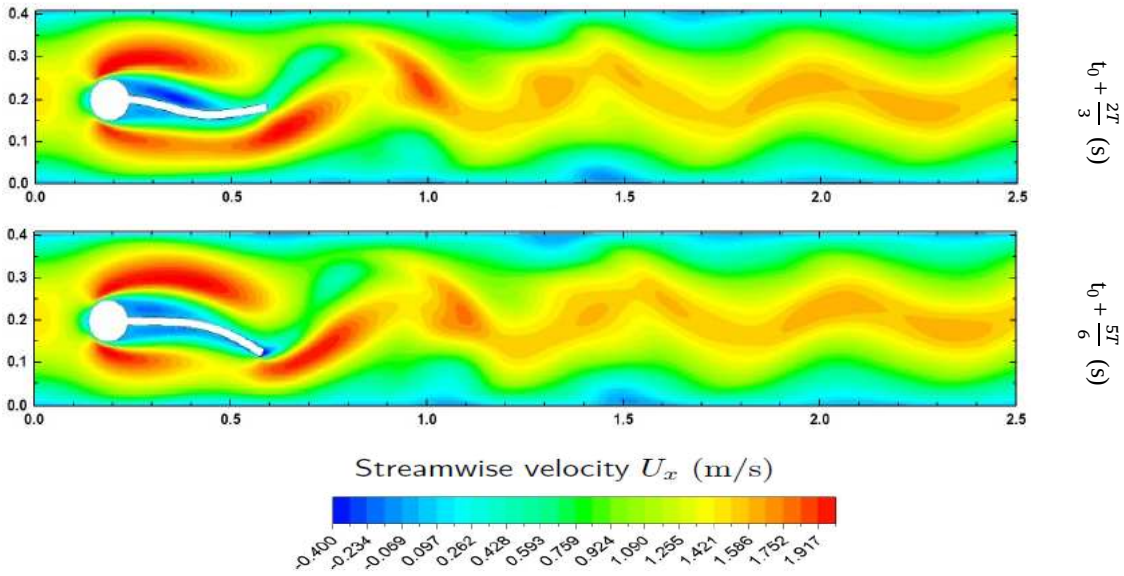

Figure 6.4: Instantaneous streamwise velocity fields Ux during one period of oscillation

For comparison with Turek and Hron [8], the mean and amplitude of y displacement are computed from the last period of oscillations according to the following relations proposed in [8]:

$$mean = \frac{1}{2}(\min + \max) \tag{6.2}$$

$$amplitude = \frac{1}{2}(\max - \min) \tag{6.3}$$

The frequency of the oscillations is then computed by using a Fast Fourier Transformation on the displacement signal. Results are summarized in Table 6.2 and compared with the reference values [8]. One can observe that results are in very good agreement with the reference case and only exhibit small discrepancies for the x-direction displacement (error is of 0.14% for the mean, 1.13% for the amplitude and 1.30% for the frequency) and y-direction (error is of 5.7% for the mean, 1.24% for the amplitude and 5.0% for the frequency).

Table 6.2: Results comparison between present simulation and Turek and Hron [8]

	x direction		y direction	
	CFD results	Turek [8]	CFD results	Turek [8]
Mean (mm)	-14.56	-14.58	1.30	1.23
Amplitude (mm)	12.58	12.44	81.05	81.06
Frequency (Hz)	3.75	3.80	1.90	2.00

6.3 Validation of 3D FSI

After validating the 2D FSI numerical modeling, it is important to study the results of a 3D case FSI and compare the obtained numerical results with an experimental study done having similar boundary and initial conditions. The fluid properties and the mechanical and the properties of the VG are set to be similar for both the experiment and the numerical study.

6.3.1 Experimental setup

An experimental setup is prepared where a rectangular wing vortex generator, with a smaller dimension than that of the wind tunnel, is placed in a rectangular duct and the tilt angle of the vortex generator is measured for different values of the inlet velocity. To perform the experiment a subsonic wind tunnel is an educational tool for the highest technical level to carry out aerodynamic experiments, doubling as a sophisticated research tool. Figure 6.5 represents the experimental setup with the detailed dimensions being summarized in Table 6.3.

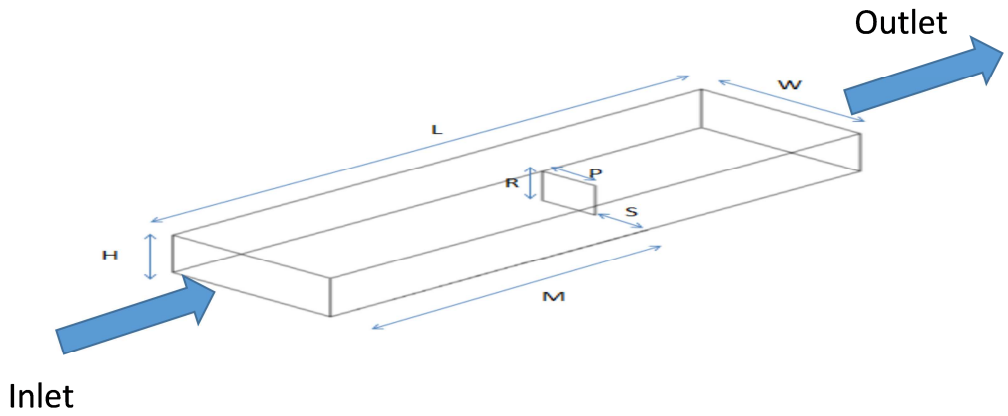

Figure 6.5: Experimental setup

Table 6.3: Dimensions of the experimental setup

H	13 cm
L	100 cm
W	30 cm
M	60 cm
S	10 cm
R	10 cm
P	10 cm

Figure 6.6 represents the experimental setup in the isometric view with the vortex generator placed in the testing duct, whereas in Figure 6.7, the side view of the experimental setup is introduced. To be able to read the tilt angle, which is the angle of the tail of the vortex generator after bending with respect to its initial perpendicular position, high definition camera is used to take several snap shots for a better reading of the values. Not only the tilt angle was a concern but also the inlet velocity value. To read the velocity values at the inlet of the duct a hot wire anemometer is placed before the vortex generator to obtain the value of the developed flow velocity at the mid plane of the channel height. Figure 6.8 summarizes the schematic detailed diagram of the experimental setup.

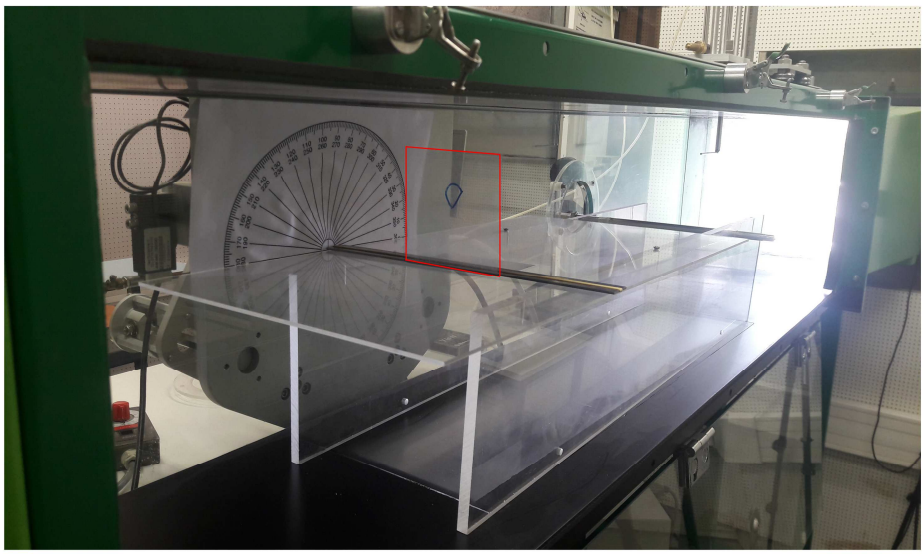

Figure 6.6: Experimental setup (isometric view)

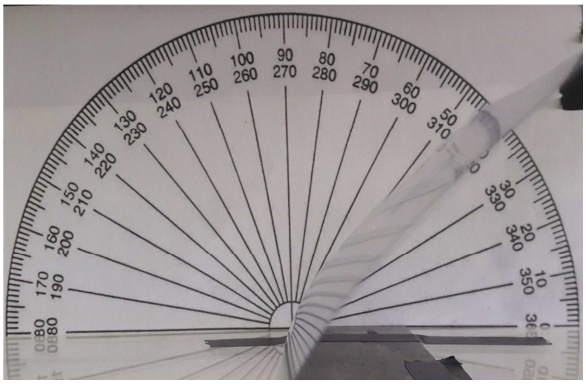

Figure 6.7: Experimental setup (side view)

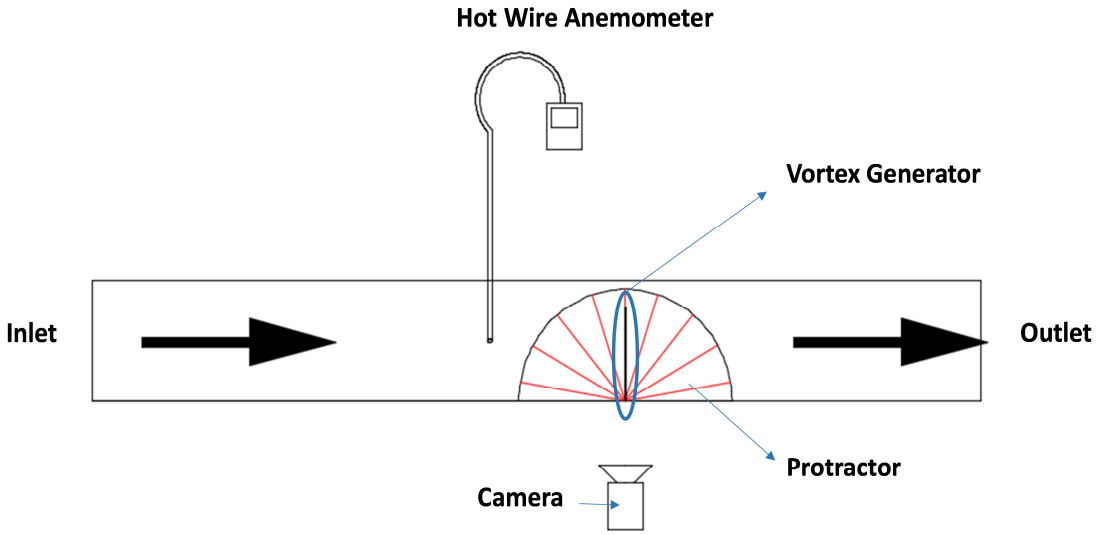

Figure 6.8: Schematic detailed diagram of the experimental setup

To be able to read the angle of tilt experimentally, a method has been adopted. Figure 6. **9** represents the method, where the α represents the tilt angle measured between the bottom wall and the head of the VG after deflection.

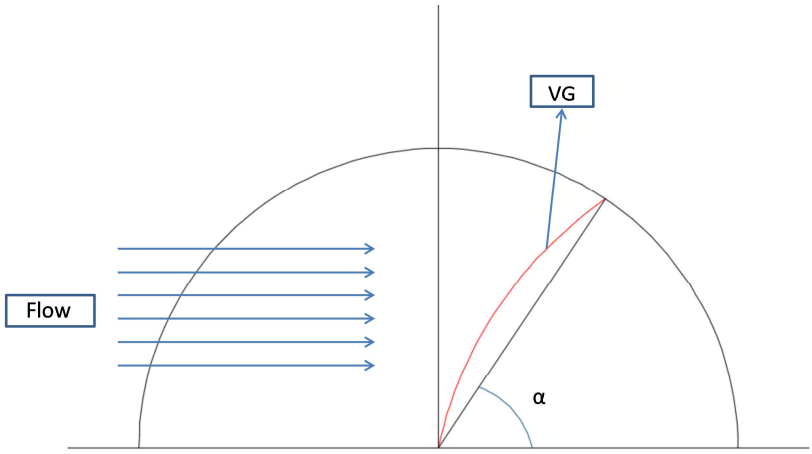

Figure 6. 9: Tilt angle measuring method

6.3.2 Experimental results

The most challenging part of the experimental study was to determine the type of the vortex generator used in the system to observe a deflection in the tilt angle value with a slight variation in the inlet velocity value. Different types of flexible materials are used with different thicknesses. **Table 6. 4** represents the list of the materials used.

Table 6. 4: List of the Materials used for the VG

Materials	Thickness (mm)
Nylon 6.6	0.2 and 0.5
LDPE (Low Density Polyethylene)	0.7
Rubber	2 and 5

Figure 6.10 represents the case where Nylon 6.6 is used having a thickness of 0.5 mm. The tilt angle of the VG is measured as mentioned above with respect to the increase of the Reynolds number. As the Reynolds number increases the tilt angle increases too. Reaching to values of around 45° for Reynolds number values of Re =110000, after which there was a very high perturbation in the VG. The same has been repeated twice for both increasing the velocity and decreasing the velocity and the results are represented as Trial 1 and Trial 2.

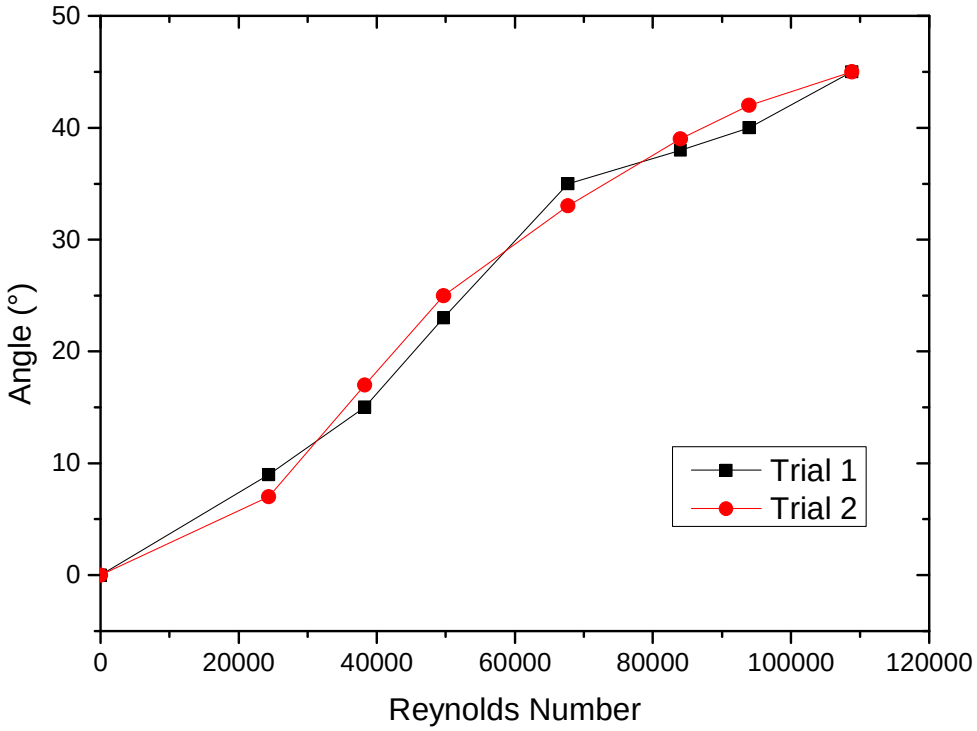

Figure 6.10: Nylon 6.6 VG with a thickness of 0.5 mm

The thickness of the VG has a great influence on the tilt angle deflection, to have a deeper study in this domain several thicknesses have been studied for the same material. Figure 6.11 represents the tilt angle variation with respect to the Reynolds number for Nylon 6.6 VG with a thickness of 0.2 mm. For lower values of Reynolds number compared to that of 0.5 mm thickness VG, the tilt angle deflection has a higher value, reaching 45° at a Reynolds number of around 58000.

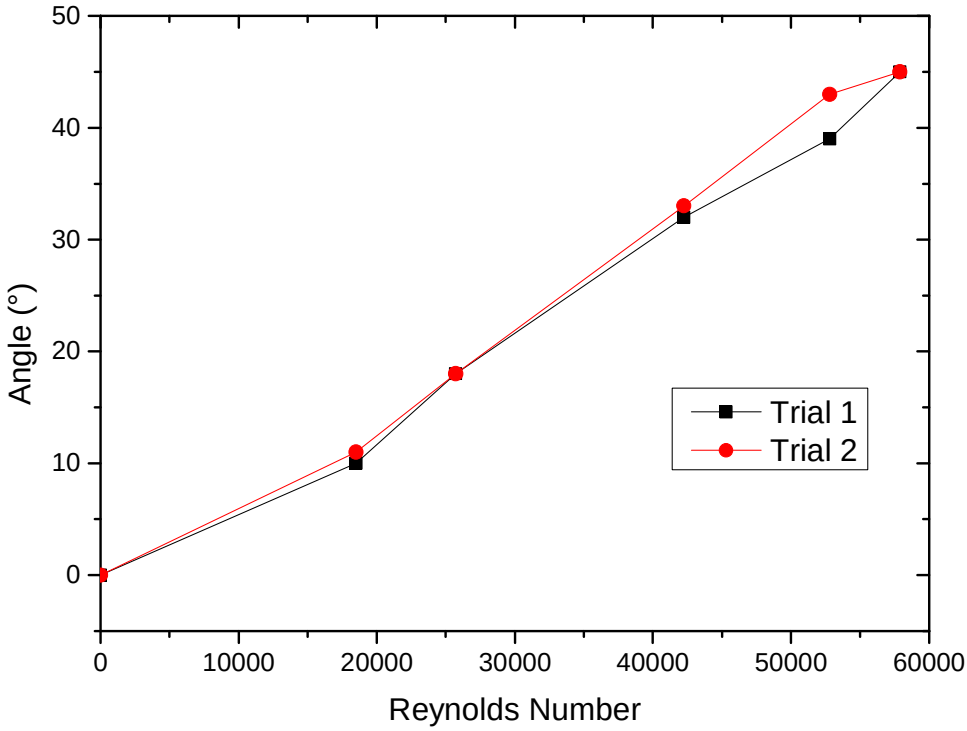

Figure 6.11: Nylon 6.6 VG with a thickness of 0.2 mm

As a further study, low density polyethylene (LDPE) is used having a thickness of 0.7 mm, the outcome results are represented in Figure 6.12. The experiment has been repeated for both increasing and decreasing Reynolds number values. As the Reynolds number value increases the tilt angle deflection increases too, reaching around 28° at a Reynolds number of 65000. Since it is thicker than that of previously used VG, the physical behavior of the VG was more stable for high velocity values. Because of this, the LDPE is picked as to be used for the CFD simulations. All the mechanical and physical properties listed in Table 6. 5 of the LDPE are inserted in the CFD Ansys in order to have a reasonable comparison and validation between the CFD results and the experimentally obtained ones.

Table 6. 5: Properties of LDPE

Property	Value
Density	1200 kg/m^3
Modulus of Elasticity	110 MPa
Poisson's Ratio	0.45

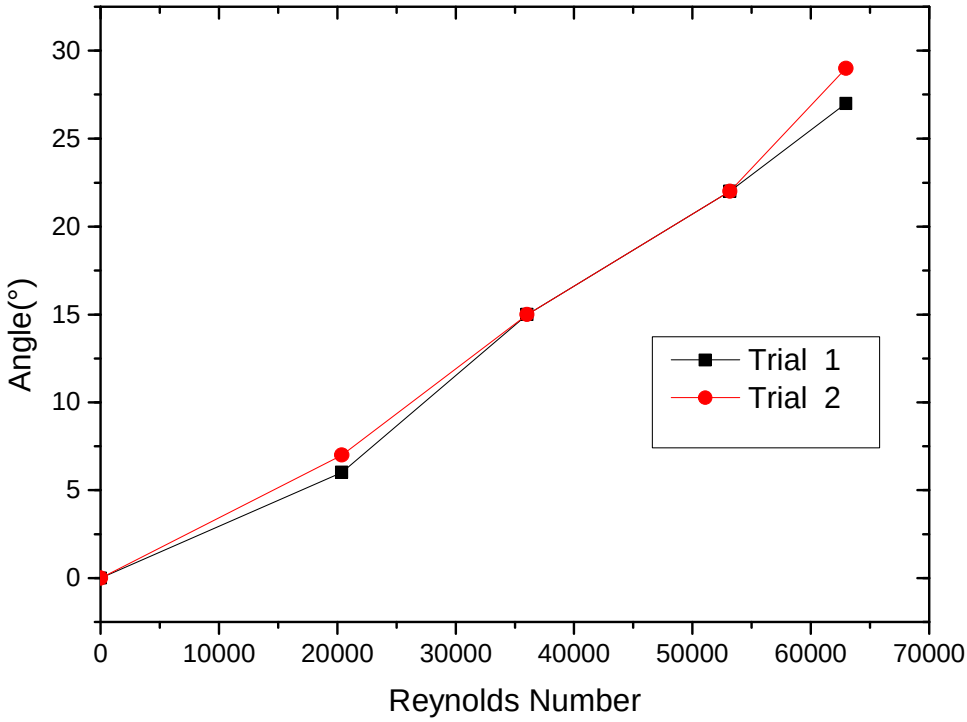

Figure 6.12: LDPE VG with a thickness of 0.7 mm

6.3.3 Validation of the velocity profile in 3D CFD FSI

To make a comparison between the experiment done and the computational studies, it was crucial to validate the results. To do so, a strategy is adopted where the inlet velocity profile within the duct is measured experimentally using hot wire anemometers and the obtained results

are set as to be the boundary condition at the inlet of the computational domain. Figure 6.13 represents the obtained results; the anemometer was placed at the inlet of the channel at a distance of 0.2 m before reaching the vortex generator. It is clear from the figure that the flow is developing flow. To be sure of the entrance profile we set the CFD entrance profile with the measured values represented in Figure 6.13. By doing so a common ground has been created for both the experiment and the CFD where both have the same geometry and similar inlet velocity and physical properties.

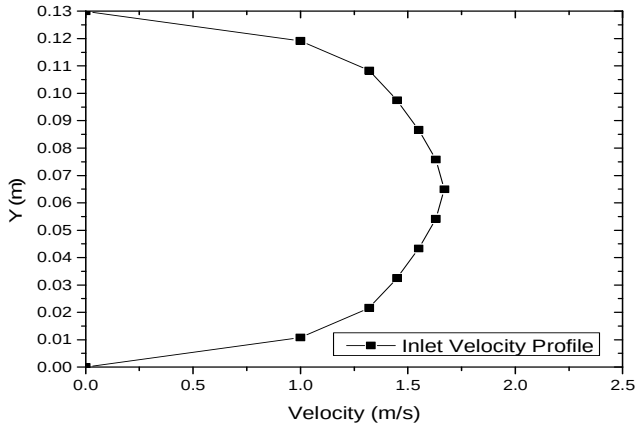

Figure 6.13: Inlet velocity profile having a U_{max} = 1.67 m/s at the middle of the channel

After running the CFD, two more parameters are studied to validate the study. One is the tilt angle of the vortex generator, and second is the velocity profile after the vortex generator. Figure 6.14 represents the velocity profile measured at a downstream distance Z=0.2 m away measured from the position of the VG. As shown in the figure, the experimental values and the simulation ones are very close. By studying the difference between the experimental and numerical results, the mean percentage error is calculated to be 11.73%. For most of the detected points the error is within the range of 5% except for that of velocity value below 0.35m/s. The main reason for having a difference in values for low velocity ranges is due to the precision of the hot wire anemometer used in the experiment to read the values.

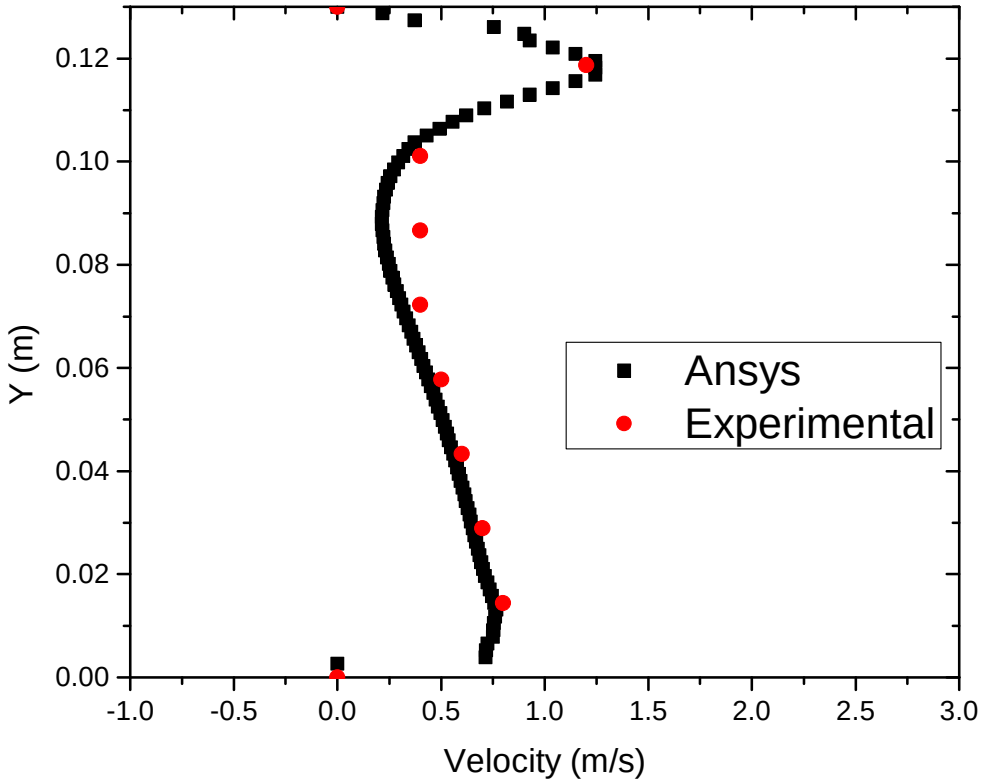

Figure 6.14 Velocity profile after the VG for (Z=0.2m downstream the VG)

6.3.4 Validation of the 3D CFD FSI

After the validation of the velocity profile, the second strategy was to check for the tilt angle value which was the main objective to the experiment. The experimental results of the tilt angle are represented with respect to different velocity values in Figure 6.12 for the case LDPE VG with a thickness of 0.7 mm. Since the deflection of the VG is the main concern of the study, a comparison is done between the CFD values and the experimental.

First, Figure 6.15 represents the deflection of the VG due to the flow obtained by the numerical simulations for the case LDPE VG with a thickness of 0.7 mm. After obtaining steady state, the

coordinates of the VG are taken and plotted using AutoCAD. Table 6.6 represents the coordinates of each point located on the VG: point A represents the intersection point of the VG with the ground, point B represents the head of the VG initially and point C represents the head of the VG at the end of the simulation at a steady state. After drawing the geometry, the tilt angle was measured using the dimensions toolbox and it was 6°.

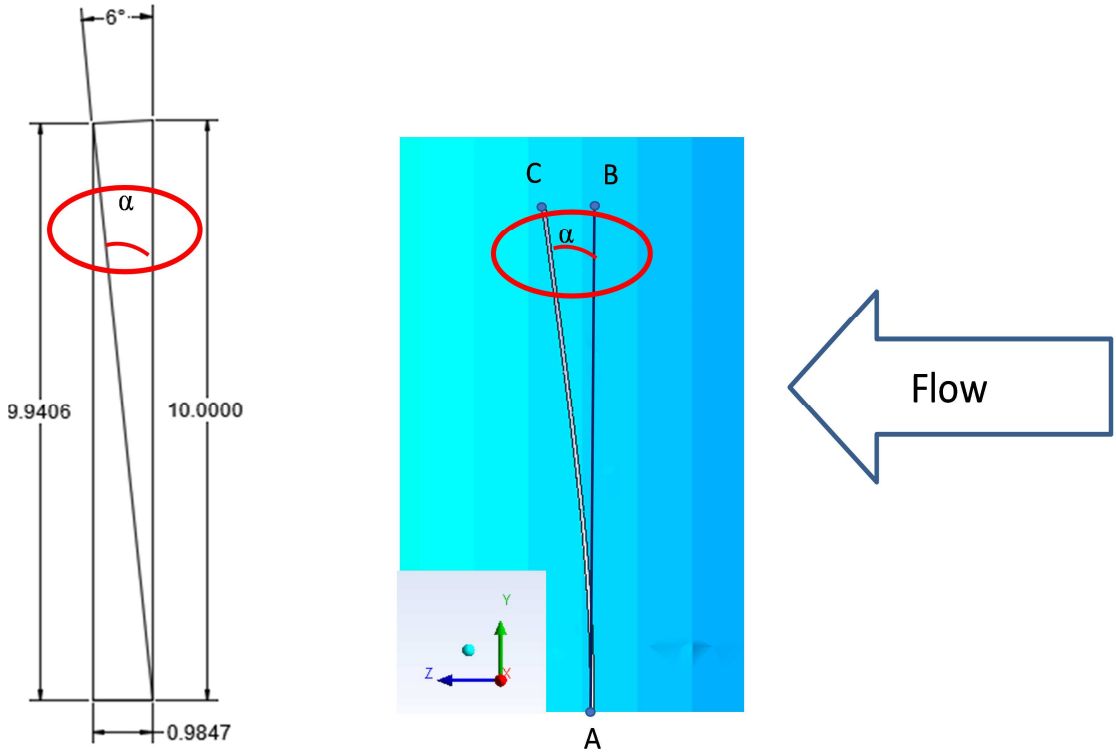

Figure 6.15: Tilt angle obtained by CFD using 0.7mm LDPE at Re 20,700

Table 6.6: Coordinates of the VG obtained by CFD using 0.7mm LDPE at Re 20,700

Coordinates (mm)	x	y	z
A	150	0	100
B	150	100	100
C	150	99.406	109.847

The result obtained experimentally is compared to that of the CFD, Figure 6.16 represents the zoomed values of the tilt angles obtained experimentally.

. It is obvious that the experimentally read deflection was between 5.5°-7°. It is crucial to indicate that both cases, experimental and the CFD have the same inlet velocity as indicated in Figure 6.13.

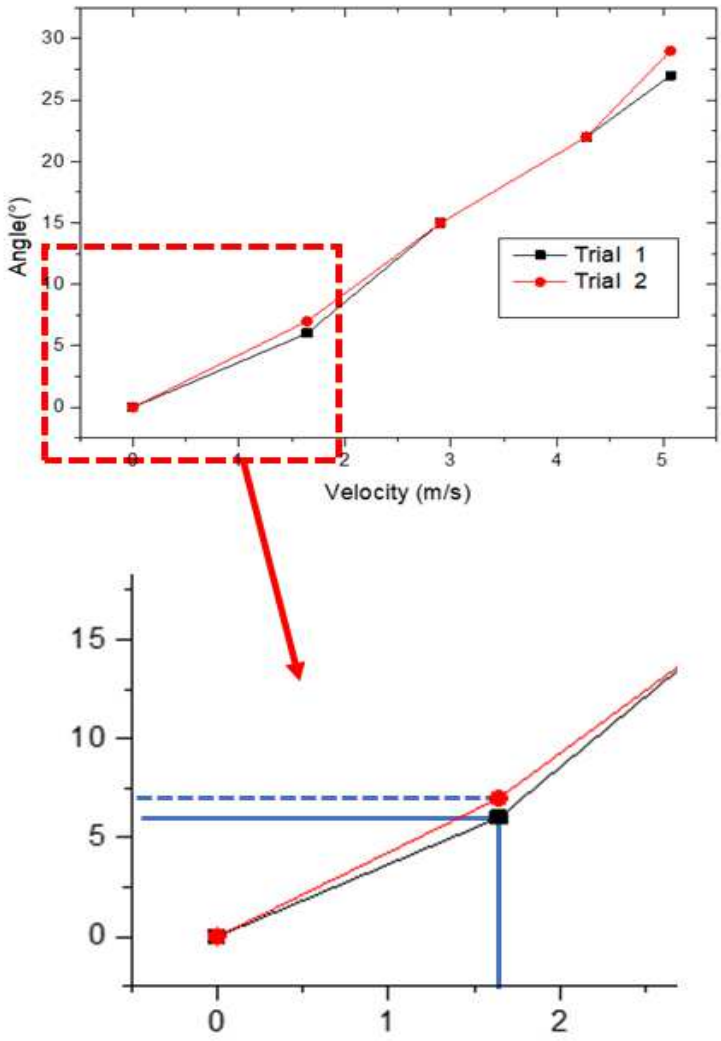

Figure 6.16: Tilt angle experimental results using 0.7mm LDPE at Re 20,700

6.4 CFD analysis of auto adaptive Vortex Generator

After validating the experiment with respect to the CFD simulations, it was clear that to have a large deflection the flow regime became turbulent. Since the 3D FSI simulations are time consuming, the first strategy was to start with a case of 2D. As a computational domain for the 2D FSI simulations, the geometry of the RWVG discussed in Chapter 5 is taken with different turbulent values of Reynolds numbers (4000, 5000, 10000 and 15000). The initial angle of attack was considered to be the optimal angle found based on the study done in Chapter 5 having a value of 25°. The inlet profile of the velocity is set to be as uniformed for all the cases. Table 6.7 represents the summary of each case with the boundary conditions for the 2D FSI simulations.

Table 6.7: Initial and boundary conditions of 2D FSI simulations

Case	Re	v_{in}	T_{in}	T_{wall}
Units		(m/s)	(K)	(K)
1	4,000	1.461	293	333
2	5,000	1.826	293	333
3	10,000	3.652	293	333
4	15,000	5.478	293	333

Before analyzing the outcome results, it is important to validate the steadiness of the solution for all the different cases performed. To do so, the outlet temperature of the channel and the output velocity of the channel are monitored with respect to time. Figure 6.17 and Figure 6.18 represent these two parameters respectively. It is obvious that for both cases the outcome values are at steady state.

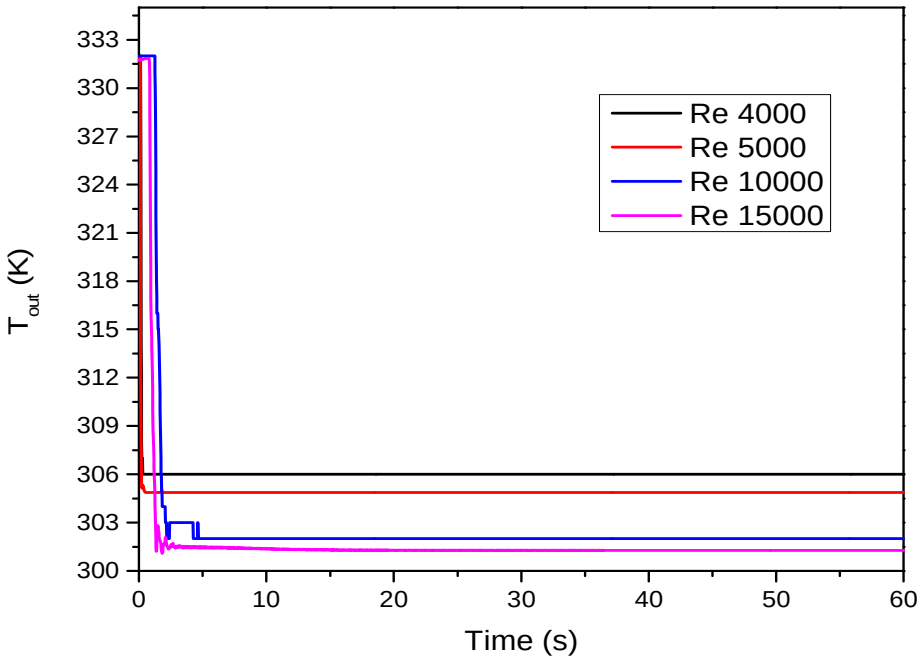

Figure 6.17: The outlet temperature

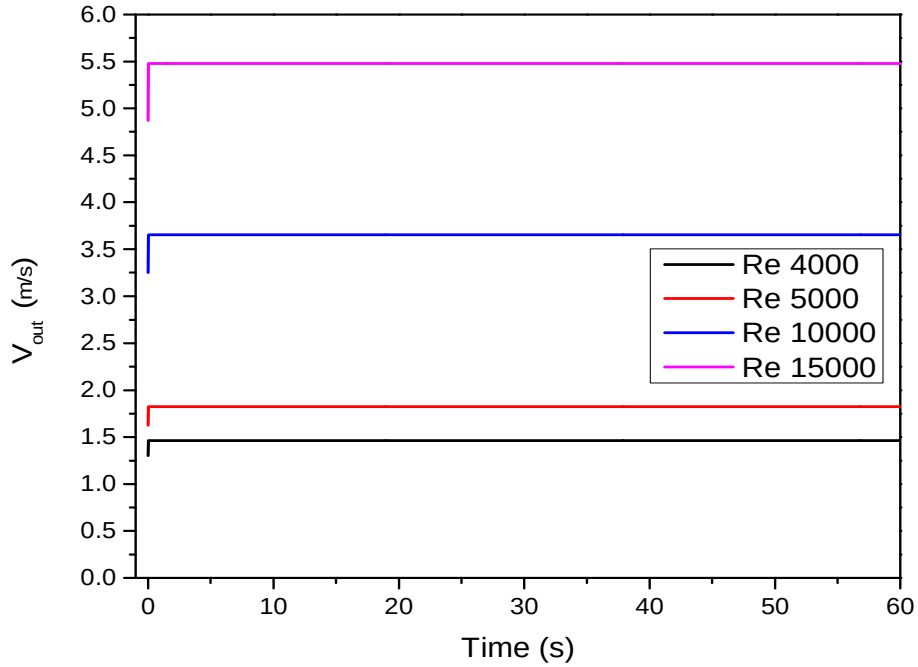

Figure 6.18: The outlet velocity

After having the cases where all the cases have complete steadiness, the local velocity and temperature contours are studied. Figure 6.19 and Figure 6.20 represent the velocity and the temperature contours respectively, for the case of the auto adaptive VG driven by the pressure of the flow. By the increase of the Reynolds number, the flow topology of the fluid is differed. For higher Reynolds number values the effect of the vortices developed along the channel are sustained till the outlet of the channel. For all the cases, a dead zone is developed at the back of the VG, where due to very low velocity values the thermal convection is reduced, and a conductive heat transfer occurred.

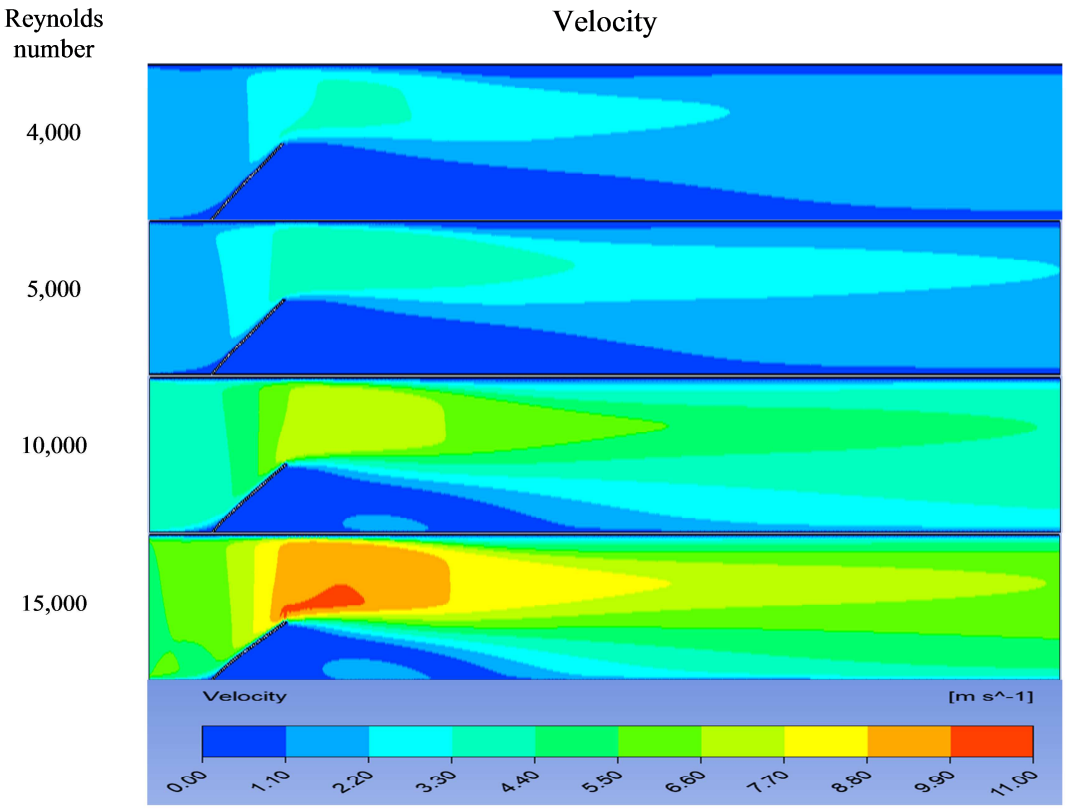

Figure 6.19: Velocity contours of 2D FSI for different Reynolds numbers

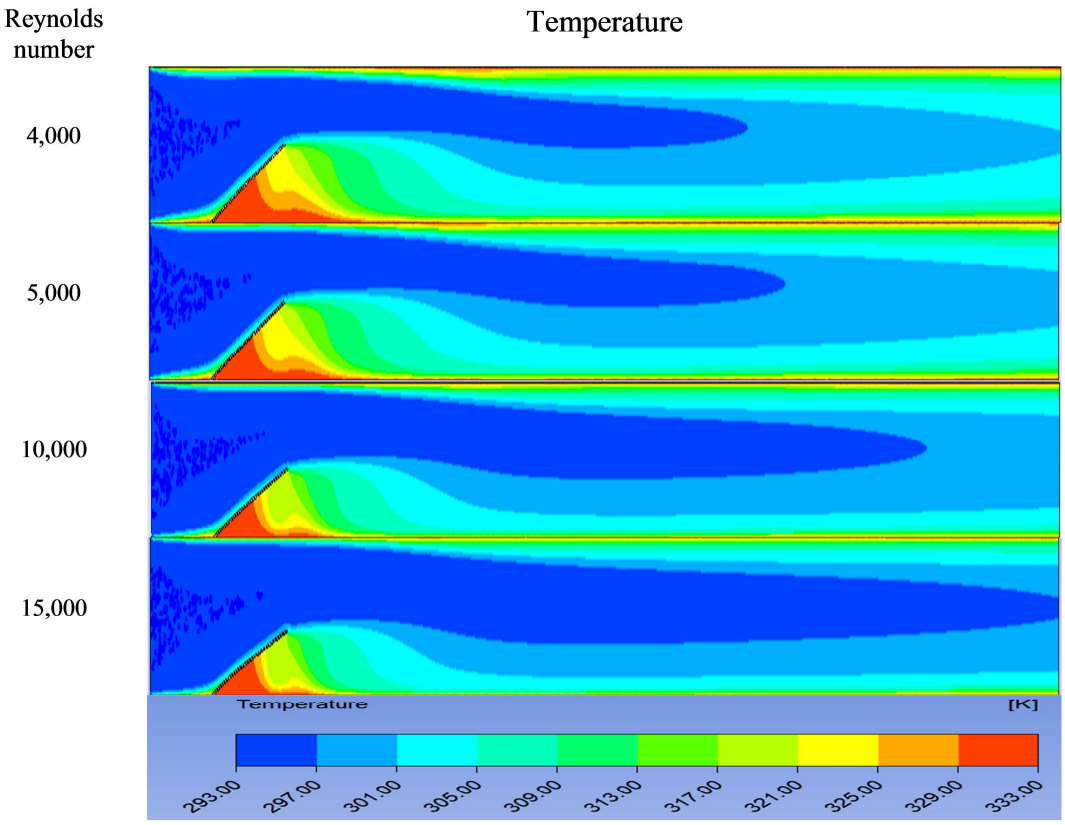

Figure 6.20: Temperature contours of 2D FSI for different Reynolds numbers

To be able to study some physical parameters being affected by the auto adaptive VG, the outlet temperature, the pressure drop and the deflection tilt angle of the VG for all the different cases are tabulated in Table 6.8. By increasing the Reynolds number, the outlet temperature is slightly decreased whereas the pressure drop is largely increased. Because of the high velocity the tilt angle has been increased.

Table 6.8: Summary outcomes of 2D FSI simulations

Case	Re	v_{in}	T_{in}	T_{out}	ΔP	$\Delta\alpha$
Units		(m/s)	(K)	(K)	(Pa)	(°)
1	4,000	1.461	293	305.771	3.330	2
2	5,000	1.826	293	304.869	4.226	3
3	10,000	3.652	293	302.480	11.454	5
4	15,000	5.478	293	300.95	19.321	7

6.5 CFD analysis of static Vortex Generator

To be able to study the effectiveness of the auto adaptive VG concept, static VG CFD simulations are performed for similar cases and the global parameters have been compared. Figure 6.21 and Figure 6.22 represent the velocity and temperature contour for the different Reynolds number. For all the cases, the initial value of the angle of attack α is set to be α = 25°.

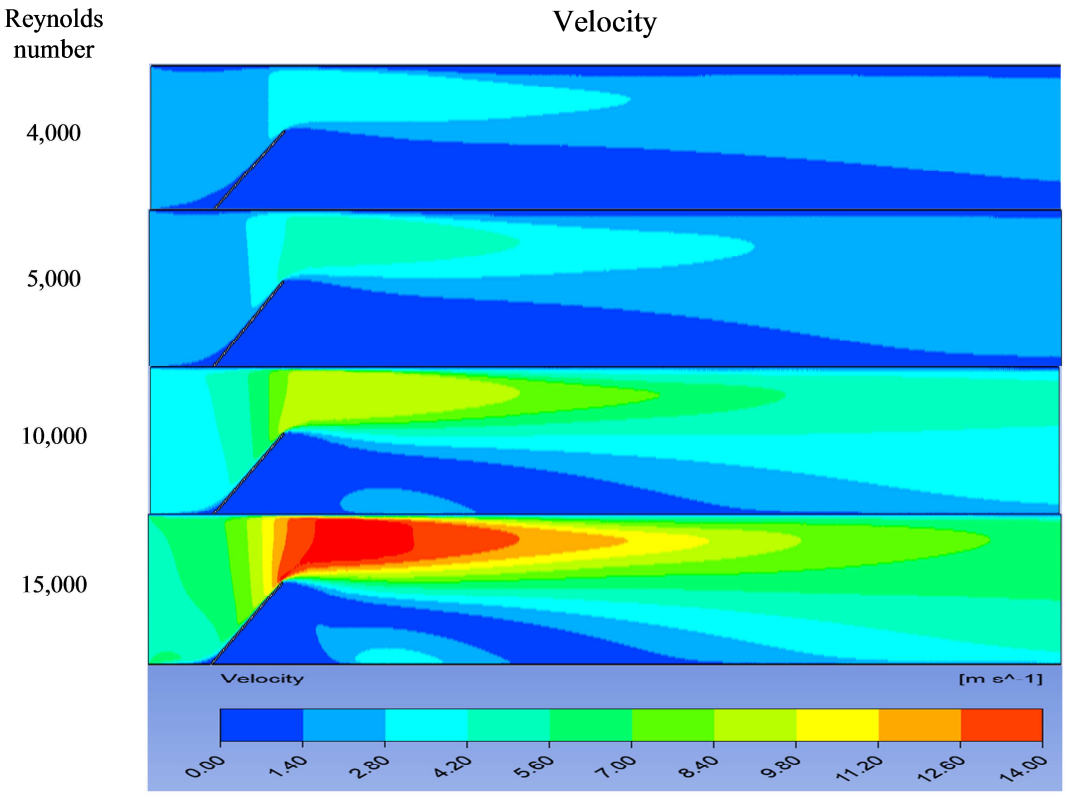

Figure 6.21: Velocity contour of 2D static VG for different Reynolds numbers

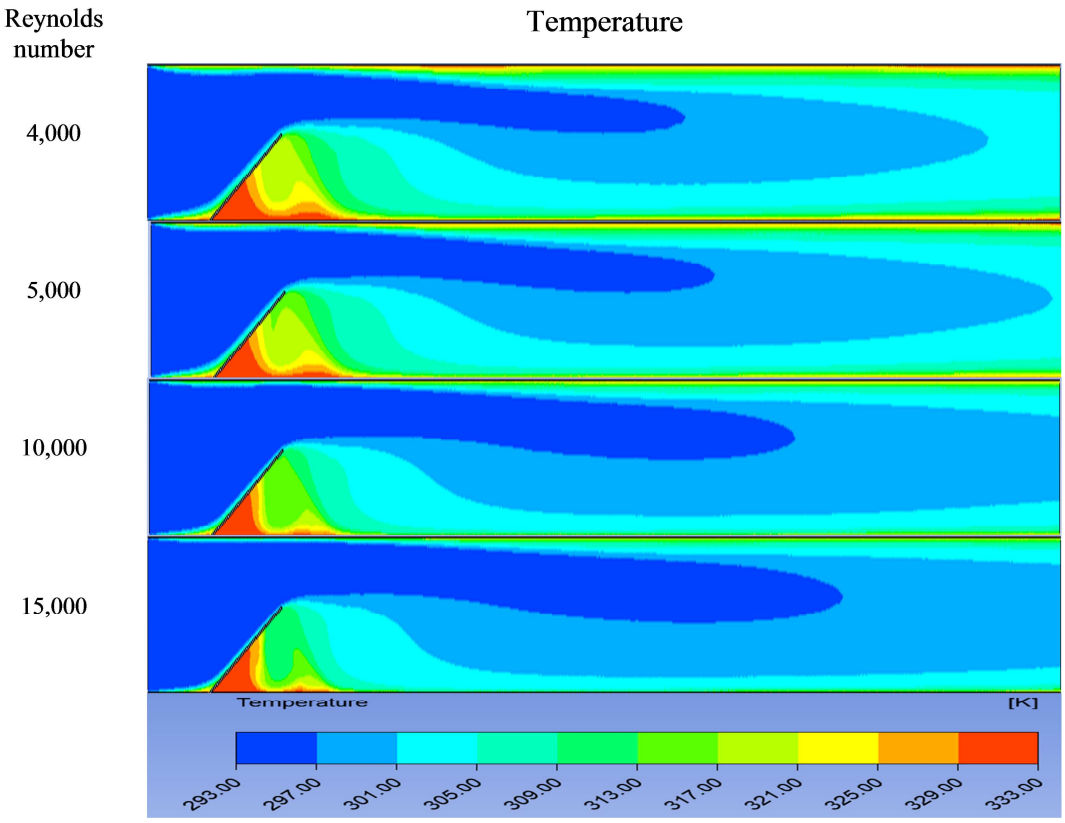

Figure 6.22: Temperature contour of 2D static VG for different Reynolds numbers

To be able to compare the physical parameters studied for the case of the auto adaptive VG, similar factors are studied and tabulated in Table 6.9. By increasing the Reynolds number, the outlet temperature is slightly decreased whereas the pressure drop is largely increased. Since the VG is static in these cases, there is no study of the deflection angle since it is constant ($\alpha = 25°$) for all the cases.

Table 6.9: Summary outcomes of static VG simulations

Case	Re	v_{in}	T_{in}	T_{out}	ΔP
Units		(m/s)	(K)	(K)	(Pa)
1	4,000	1.46	293	304.51	4.43
2	5,000	1.82	293	303.80	6.75
3	10,000	3.65	293	301.97	25.47
4	15,0000	5.47	293	301.10	56.03

6.6 CFD comparison of static and auto-adaptive Vortex Generators

In Figure 6.24, a parametric study is done where the global Nusselt number is calculated for each Reynolds number. Both the static and auto adaptive VG are plotted. By increasing the Reynolds numbers, both cases have a quasi-proportional behavior within the range studied in the present work. For all the studied Reynolds numbers, the values obtained for the static VG are higher than that of the auto adaptive. Because of the increase of the Nusselt number, the heat transfer is being better enhanced in the case of the static VG compared to the auto-adaptive VG. On the other hand, it is important to study the coefficient of the friction and monitor the pressure drop.

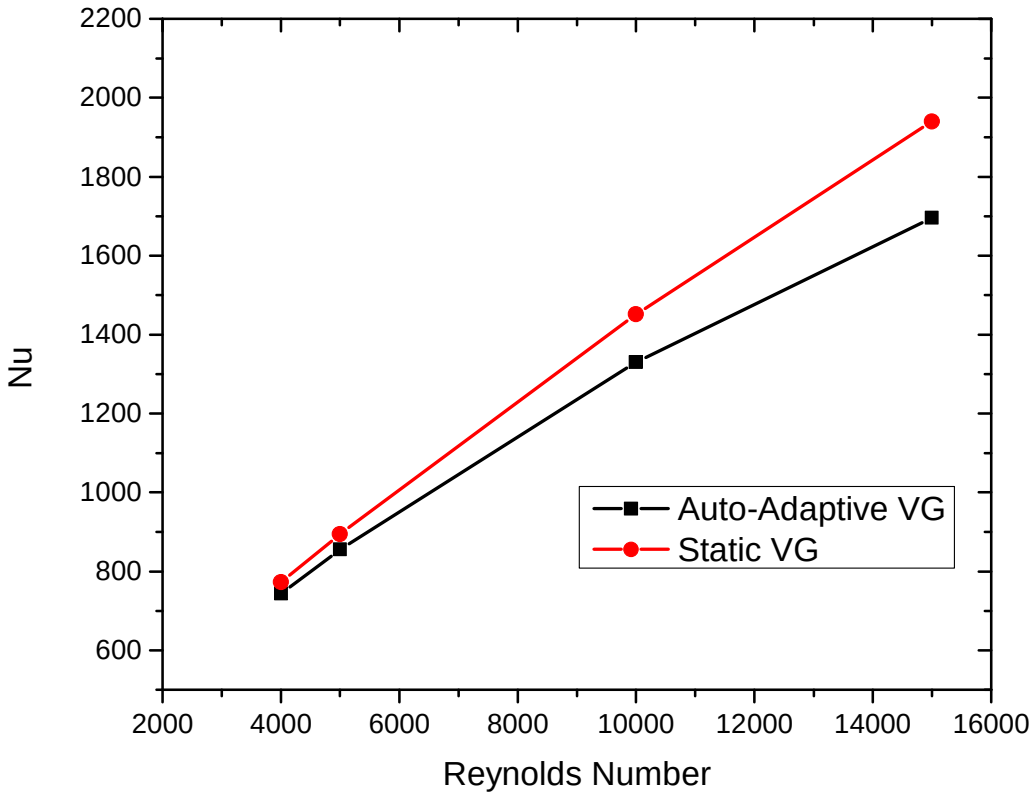

Figure 6.23: Global Nusselt number for both static VG and auto-adaptive VG

Figure 6.24 represents the coefficient of friction for the studied cases. It is interesting to investigate that for the case of the static VG, as the Reynolds number increases the friction factor increases too. On the other hand, for the case of the auto adaptive VG as the Reynolds increases, the global coefficient of the friction decreases. This phenomenon is supported with Figure 6.15 where the tilt angle is being deflected with the increase of the inlet velocity. As a result, the pressure drop is then being decreased.

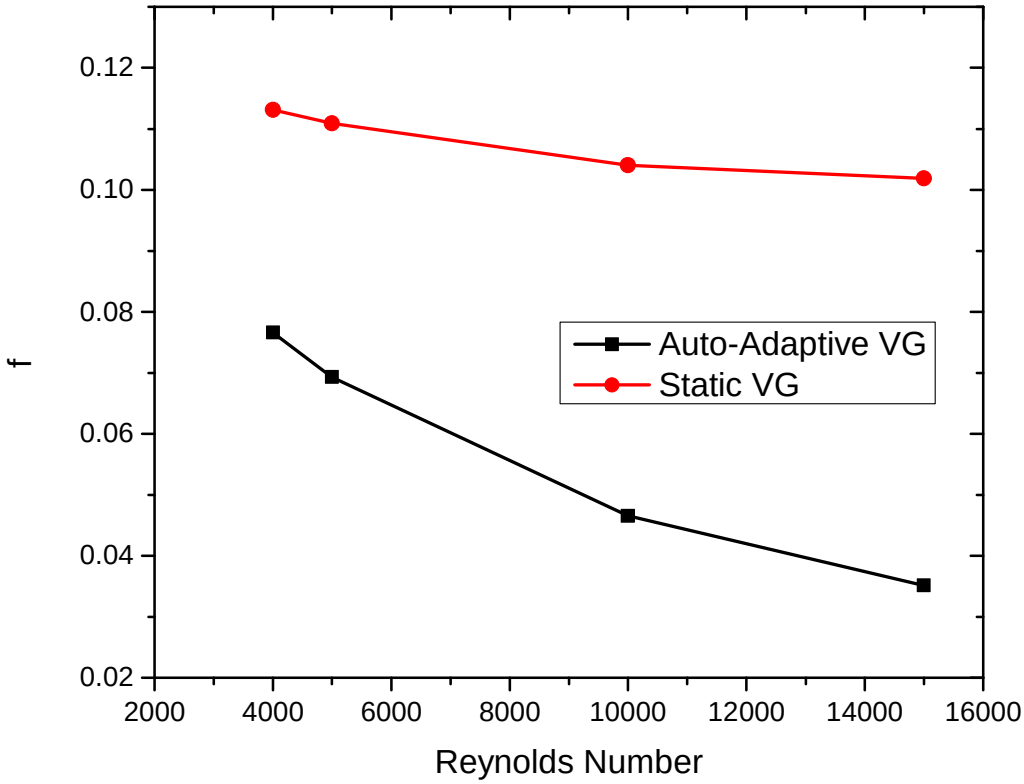

Figure 6.24: Global friction factor for both static VG and auto-adaptive VG

To be able to study and analyses the differences between the static VG and the auto-adaptive VG, Figure 6.25 represents the enhancement factor as defined in equation 6.1 for each case for all the studied Reynolds numbers.

$$\phi = \left(\frac{Nu_{FSI}}{Nu_{static}}\right)\left(\frac{f_{FSI}}{f_{static}}\right)^{(-1/3)} \tag{6.1}$$

For all the cases, the auto adaptive VG exhibits a higher value than that of the static VG. For Reynolds number 4000, the ratio is 1.09 between the static and the auto-adaptive, while this ratio

increases with the increase of the Reynolds number and reaches the highest values of 1.245 for the case of the Reynolds number 15000.

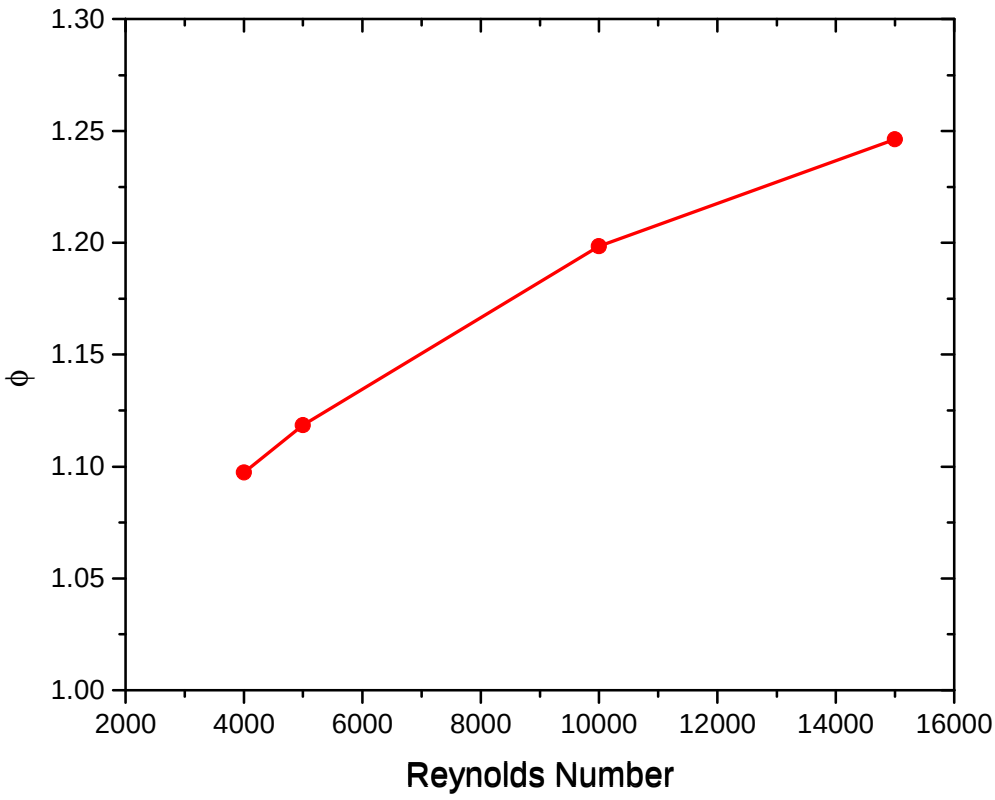

Figure 6.25: Enhancement factor for both static VG and auto-adaptive VG

6.7 Conclusion

The study of the vortex generators in the enhancement of the heat transfer in heat exchangers has been deepened and branched. In this study, the concept of the pressure driven auto-adaptive vortex generator is introduced and studied. After validating the 2D FSI code by comparing the results with that of Turek [8], it was important to prepare an experimental bench with auto adaptive vortex generator and compare the results with that of the 3D FSI code. The mechanical

and physical properties of the VG were concern in this study to be able to have an acceptable deflection at reasonable inlet velocity.

After experimental validations and computation models, the computational domain of the chapter 5 is used where the VG was set to be auto adaptive with respect to the flow. Different values of Reynold's numbers 2D FSI simulations studied and their results are compared with that of the static VG. After representing the local temperature and the velocity contours, it was interesting to study some global parameters being affected by the auto adaptive VG.

By studying the thermal effect, it was clear that the static VG has a higher effect on the heat transfer than that of the auto adaptive (Figure 6.23). For all the Reynold's numbers the curve of the static VG is higher than that of the auto adaptive.

On the other hand, the parameter of the global friction factor, the auto adaptive VG have a lower value and as the Reynold's number increases the friction factor decreases, however for the static VG it starts at a higher value than that of the auto adaptive and as the Reynold's increases it continues to increase.

To be able to study and analyze the overall performance of the design, the thermal enhancement factor is studied (Figure 6.25), for all the Reynold's numbers the enhancement occurred by the auto adaptive VG is higher than that of the static VG. And as the Reynold's increases the enhancements increases too.

After successfully validating the concept of the auto adaptive VG, it will be interesting to perform 3D FSI simulations and study the effect of both the longitudinal and the transverse vortices, and study both the local and global parameters. In addition, it would be crucial to perform studies with higher Reynolds numbers (above 15000), having in mind that the pressure driven auto adaptive VG may lead to a development of new kind of heat exchangers.

CHAPTER 7

Conclusions and Perspectives

7.1 Conclusions

The objective of this study was to investigate the use of pressure driven auto-adaptive vortex generators. To be able to fulfill the objective of the thesis, it was crucial to study and evaluate the concepts of the vortex generators and their effect of the heat transfer enhancement. Detailed overview about heat transfer methods was first presented in a literature review, mainly divided into passive and active methods with emphasis on vortex generators. Vortex generators are one of the passive methods that create secondary flows, disrupt the growth of the boundary layer and create swirling flows that enhance exchange between the walls and the core fluid, thus improving heat transfer. For the case of the passive vortex generators, the number of vortices generated is limited. On the other hand, active methods provide an additional flexibility by controlling frequency, velocity and oscillations amplitude of the vortex generators, hence influencing the number and strength of the vortices create. Nevertheless, active methods require the implementation of an additional external source of energy to control the vortex generators causing an increased complexity of installing the system and more energy consumption.

To be able to design an auto-adaptive vortex generator, a strategy is proposed, where the study is started with simpler cases and has been developed gradually to end up by the auto-adaptive vortex generator.

In the first part of the study, heat transfer and fluid flow characteristics in a rectangular duct with rectangular winglet pair vortex generator (RWPVG) inserted on its bottom wall are numerically investigated. For different values of static vortex generator's roll-angle (β) both local and global hydrodynamic and thermal parameters are calculated and studied. The goal of these studies is to figure out the effect of the roll-angle on the heat transfer enhancement. It was concluded that for high values of roll-angle (close to β=90°), it is observed that the helicity increases just after the flow encounters the VG where the vortices are first formed. The helicity peak for β=90° is about 12 folds higher than that for β=20° meaning more energetic vortices. Moreover, increasing the mean flow velocity, i.e. the Reynolds number, leads to increase the helicity. It is observed that for Re=456, the dimensionless X/H position of the main vortex measured from the bottom wall,

starts at low position and increases along the duct until it reaches a maximum value of around 0.5 representing the middle of the duct for the highest value of roll-angle β. Whereas for the case of higher Reynolds number, dimensionless location of the main vortex is increased suddenly at the Z/H=6.5 and after that in continuous to increase gradually along the length of the duct. For Re=911, the highest value of X/H=0.5 is reached by the high values of β. Whereas for β=30° the value X/H=0.35, and for β=20° X/H=0.2. It is crucial to take into consideration that by increasing the roll-angle value, not only the heat transfer will be enhanced but on the other hand, the pressure drop will increase too. To be able to make decision for this challenging issue the enhancement factor is studied where both the heat transfer and the pressure drop are taken into consideration. For Re=456, it is shown that the enhancement factor monotonically increases with the increase of the roll-angle β, reaching its maximum value of 1.20 at β=90°. On the other hand, for the case of Re=911 the profile of the enhancement factor starts to increase with the roll-angle β until it reaches a maximum value of 1.32 near β=70°. Thus, it can be considered that for Re=911 the optimum roll-angle among those tested values of β which leads to the best enhancement is 70° and not the highest angle, while for Re=456 the optimum value of β among those tested is the highest angle 90°. After all these investigations, it is crucial to mention that the roll-angle β has a significant effect on the enhancement of the heat transfer. It is interesting to study the 70° case in place of the perpendicular RWPVG for further investigations. As an advancement of the obtained results, few more values of β can be added for values near to 70° to find the exact value of the optimum angle. Due to different values obtained for different Reynolds numbers, it is interesting to go to higher Reynolds and even study in the turbulent regime too.

In the second part of the study, the heat transfer and fluid flow behavior in a parallel plate channel with rectangular wing vortex generator (RWVG) inserted on the bottom wall is numerically investigated. For different values of angle of attack α, both the local and the global parameters are calculated and studied to figure out the effect of the angle of attack on the heat transfer enhancement. It was concluded that for high values of angle of attack (close to α=30°), the generated vortices get wider and more energetic along the longitudinal direction compared to low values (i.e. α=10°). Also, it is observed that the helicity increases just after the flow encounters the VG where the vortices are first formed. The helicity peak for α=30° is about 6 folds higher than that for α=10° meaning higher energetic vortices. Moreover, it is observed that

for α in the range [10°–25°], the dimensionless vertical position X/H of the main vortex starts at low position and increases along the channel until it reaches a maximum value at the outlet of the channel (Z=15H) around X=0.5H representing the middle of the channel, for the case α=25°, it reaches a maximum value of X=0.58H. On the other hand, for the case α=30°, the dimensionless X/H position reaches a maximum value of X=0.68H before the outlet channel and then drops back to attain 0.55H at the end of the channel. As a conclusion of this study, the thermal enhancement factor starts to increase with the angle of attack until it reaches a maximum value of 1.043 representing 4.3% of enhancement at α=25°, beyond which its value decreases. It can be considered that the optimum angle of attack of the vortex generator which leads to the best enhancement under these operating conditions is 25° and not the highest angle.

In the third part of the study, the application of the vortex generators in the enhancement of the heat transfer in heat exchangers has been deepened and branched. The concept of the pressure driven auto-adaptive vortex generator is introduced and studied. After validating the 2D FSI code by comparing the results with that of Turek [8], it was important to prepare an experimental bench with auto-adaptive vortex generator and to compare the results with that of the 3D FSI code. The mechanical and physical properties of the VG were concern in this study to be able to have an acceptable deflection at reasonable inlet velocity. After experimental validations and computation models, the computational domain of the chapter 5 is used where the VG was set to be auto-adaptive with respect to the flow. Different values of Reynolds numbers are used in 2D FSI simulations and their results are compared with that of the static VG. After representing the local temperature and the velocity contours, it was interesting to study some global parameters being affected by the auto-adaptive VG. By studying the thermal effect, it was clear that the static VG has a higher effect on the heat transfer than that of the auto-adaptive. For all the Reynolds numbers the curve of the static VG is higher than that of the auto-adaptive. On the other hand, the parameter of the global friction factor, the auto-adaptive VG have a lower value and as the Reynolds number increases the friction factor decreases. However for the static VG it starts at a higher value than that of the auto-adaptive and as the Reynolds number increases it continues to increase. To be able to study and analyze the overall performance of the design, the thermal enhancement factor is studied for all the Reynolds numbers: the enhancement occurred by the auto-adaptive VG is higher than that of the static VG, and as the Reynolds increases the enhancement increases too.

Finally, this study identified several configuration designs for vortex generators both static and auto-adaptive. The auto-adaptive designed rely only on the fluid forces themselves without any external source of energy leading to more energy efficient and compact heat exchangers. However, there will always be suggestions and ideas to improve the designs provided in this manuscript, since the method proposed, and the fluid structure interaction field applied to heat transfer still didn't reached its maturity level and can still be considered innovative. As the first results look promising, the proposed configurations serve as a base for more future studies and investigations and some of them are highlighted in the next section.

7.2 Perspectives

The studies done in this manuscript were divided into two parts, the static vortex generators and the auto-adaptive vortex generator. The most challenging part of the computational simulations was in the second part of the thesis having FSI simulations and preparing the experimental workbench. The time to perform the 2D FSI simulations including the validation simulation, could vary from six weeks to ten weeks period for each unsteady 2D FSI simulation. Moreover, to prepare the experimental workbench, with the needed sensors and instrumentations, it took around five to six months to be able to prepare the setup and perform the experiments. For the validation of the 3D FSI results with that of the experiment, a 3D unsteady FSI simulation is prepared and run a period of six months.

For the first part of the study related to static vortex generators, it would be interesting to perform further simulations for both lower and higher Reynolds numbers. As the computational engines are being developed, it will be interesting to find the optimum angles of the VG using Optimate software and not modifying the geometry manually since the software does the needed modifications based on set restrictions and suggests the optimum design. The shape of the geometry for the static VG where considered as fixed. However, it will be interesting if new designs of VG were used and their effect on the generation of vortices studied.

For the case of the auto-adaptive vortex generators, when large structural deformation occurs, the remeshing algorithm agglomerates the cells that violate a skewness or a size criterion and replaces them with better quality cells, thus preventing the mesh from excessive deterioration.

However, this does not always guarantee a mesh motion without negative cell volume divergence problems, since the automatic remeshing is always called after structural deformation. Thus, if the time step chosen is large enough compared to the smallest cell near the fluid-solid interface, this cell will be compressed or stretched to a negative volume before the remeshing solver is invoked. This was the main reason that in the two-dimensional studies performed in this manuscript, the time step was restricted to as low as 10^{-4} s. Nevertheless, the remeshing algorithms available only perform well with tetrahedral, wedges and prism cells but don't support hexahedral cells. The layering algorithm supports hexahedral cells remeshing but it is only efficient when the motion is purely translational, thus it was necessary to perform the meshing with only tetrahedral cells which eventually increases the number of cells in the domain and requires much more CPU memory. To avoid this, different methods should be used like meshless methods such as smoothed particle hydrodynamics (SPH) [65] or algorithms that model the fluid-structure interaction problem by considering nonmatching overlapping meshes such as the immersed boundary method [66] or the fictious domain method [67].

More studies can be performed to explore higher Reynolds numbers and maybe different solid materials with higher stiffness. Also, further 3D FSI unsteady simulations can be performed and study the effect of both longitudinal and transverse vortices, and study both local and global parameters. It will be interesting even to have different fluids used (water) as a cooling system to increase the pressure forces developed by their flow and thus increase the deflection of the VG. However, these types of simulations need powerful computers and the experimental setups will be more costly.

Finally, this study is a start for a lot of more investigations and research since the parameters that govern the motion and its implications on heat transfer need more deep research to reach its full maturity level. As seen from this section, the studies already presented in this manuscript can open the door to different kind of other future works.

REFERENCES

[1] World Energy Outlook 2018, International Energy Agency, 2018

[2] Khoshvaght-Aliabadi M., Zangouei S., Hormozi F., Performance of a plate-fin heat exchanger with vortex-generator channels: 3D-CFD simulation and experimental validation, International Journal of Thermal Sciences, 88 (2015) 180-192.

[3] Ali S., Habchi C., Menanteau S., Lemenand T., Harion J.L., Heat transfer and mixing enhancement by free elastic flaps oscillation, International Journal of Heat and Mass Transfer, 85 (2015) 250-264.

[4] Alahyari Beig S., Mirzakhalili E., Kowsari F., Investigation of optimal position of a vortex generator in a blocked channel for heat transfer enhancement of electronic chips, International Journal of Heat and Mass Transfer, 54 (2011) 4317-4324.

[5] Jiang Y., Zheng Q., Dong P., Zhang H., Yu F., Research on heavy-duty gas turbine vane high efficiency cooling performance considering coolant phase transfer, Applied Thermal Engineering, 73 (2014) 1175-1191.

[6] Basu D.N., Bhattacharyya S., Das P.K., A review of modern advances in analyses and applications of single-phase natural circulation loop in nuclear thermal hydraulics, Nuclear Engineering and Design, (2014).

[7] Fiebig M., Vortices, Generators and Heat Transfer, Chemical Engineering Research and Design, 76 (1998) 108-123.

[8] Habchi C., Russeil S., Bougeard D., Harion J.L., Lemenand T., Della Valle D., Peerhossaini H., Enhancing heat transfer in vortex generator-type multifunctional heat exchangers, Applied Thermal Engineering, 38 (2012) 14-25.

[9] Turek S. and Hron J. Proposal for Numerical Benchmarking of Fluid Structure Interaction Between an Elastic Object and Laminar Incompressible Flow. Ergebnisberichte angewandte Mathematik. Univ., 2006.

[10] R.L. Webb. Enhancement of single-phase heat transfer. Wiley, New York, 1987.

[11] M. Fiebig, P. Kallweit, N. Mitra, and S. Tiggelbeck. Heat transfer enhancement and drag by longitudinal vortex generators in channel flow. Experimental Thermal and Fluid Science, 4(1):103–114, 1991.

[12] H.K. Ma, B.R. Chen, H.W. Lan, K.T. Lin, and C.Y. Chao. Study of a led device with vibrating piezoelectric fins. In Semiconductor Thermal Measurement and Management Symposium, 2009. SEMI-THERM 2009. 25th Annual IEEE, pages 267–272. IEEE, 2009.

[13] Y. Yu, T. Simon, M. Zhang, T. Yeom, M. North, and T. Cui. Enhancing heat transfer in air-cooled heat sinks using piezoelectrically-driven agitators and synthetic jets. International Journal of Heat and Mass Transfer, 68:184–193, 2014.

[14] C. Williamson and R. Govardhan. Vortex-induced vibrations. Annu. Rev. Fluid Mech., 36:413– 455, 2004.

[15] Introduction to heat Transfer, 4th edition, Frank P. Incorpera, David P.Dewitt, Theodore L Wiley

[16] Anxionnaz Z., Cabassud M., Gourdon C., Tochon P., Heat exchanger/reactors (HEX reactors): Concepts, technologies: State-of-the-art, Chemical Engineering and Processing: Process Intensification, 47 (2008) 2029-2050.

[17] Ghanem A., Habchi C., Lemenand T., Della Valle D., Peerhossaini H., Energy efficiency in process industry – High-efficiency vortex (HEV) multifunctional heat exchanger, Renewable Energy, 56 (2013) 96-104.

[18] Tiggelbeck S., Mitra N.K., Fiebig M., Flow Structure and Heat Transfer in a Channel with Multiple Longitudinal Vortex Generators, Experimental Thermal and Fluid Science 5(1992) 425-436.

[19] Jacobi A.M., Shah R.K., Heat Transfer Surface Enhancement through the Use of Longitudinal Vortices: A Review of Recent Progress Experimental Thermal and Fluid Science, 11 (1995) 295-309.

[20] Habchi C., Lemenand T., Della Valle D., Pacheco L., Le Corre O., Peerhossaini H., Entropy production and field synergy principle in turbulent vortical flows, International Journal of Thermal Sciences, 50 (2011) 2365-2376.

[21] Mohand Kaci H., Habchi C., Lemenand T., Della Valle D., Peerhossaini H., Flow structure and heat transfer induced by embedded vorticity, International Journal of Heat and Mass Transfer, 53 (2010) 3575-3584.

[22] Zhou G., Feng Z., Experimental investigations of heat transfer enhancement by plane and curved winglet type vortex generators with punched holes, International Journal of Thermal Sciences, 78 (2014) 26-35.

[23] Wang C.C., Chen K.Y., Lin Y.T., Investigation of the semi-dimple vortex generator applicable to fin-and-tube heat exchangers, Applied Thermal Engineering, In Press (2015).

[24] Wu J.M., Tao W.Q., Numerical study on laminar convection heat transfer in a channel with longitudinal vortex generator. Part B: Parametric study of major influence factors, International Journal of Heat and Mass Transfer, 51 (2008) 3683-3692.

[25] Wu J.M., Tao W.Q., Numerical study on laminar convection heat transfer in a rectangular channel with longitudinal vortex generator. Part A: Verification of field synergy principle, International Journal of Heat and Mass Transfer, 51 (2008) 1179-1191.

[26] Edwards, F. J.,and Alker, C.J.R., The improvement of Forced Convection Surface Heat Transfer Using Surface Protrusions in the Form of (A) Cubes and (B) Vortex Generators, Heat Tranfer 1974, Proc Fifth Int. Heat Transfer Conf., Vol. 2,pp. 244-248, JSME, Tokyo, 1974.

[27] Tiggelbeck, S., Mitra, N. K., and Fiebig, M., Experimental Investigations of Heat Transfer Enhancement and Flow Losses in a Channel with Double Rows of Longitudinal Vortex Generators, *Int. J. Heat Mass Transfer*, 36, 2327-2337, 1993.

[28] K. Yakut, B. Sahin, C. Celik, N. Alemdaroglu, and A. Kurnuc. Effects of tapes with doublesided delta-winglets on heat and vortex characteristics. *Applied Energy*, 80(1):77–95, 2005.

[29] C. Min, C. Qi, X. Kong, and J. Dong. Experimental study of rectangular channel with modified rectangular longitudinal vortex generators. *International Journal of Heat and Mass Transfer*, 53(15):3023–3029, 2010.

[30] S.J. Kline, F.A. McClintok, Describing uncertainties in single-sample experiments, Mechanical Engineering 75 (1953) 3–8.

[31] C. Habchi, S. Russeil, D. Bougeard, J.-L. Harion, T. Lemenand, D. Della Valle, and H. Peerhossaini. Enhancing heat transfer in vortex generator-type multifunctional heat exchangers. *Applied Thermal Engineering*, 38:14–25, 2012.

[32] P. Sanders and K. Thole. Effects of winglets to augment tube wall heat transfer in louvered fin heat exchangers. *International Journal of Heat and Mass Transfer*, 49(21):4058–4069, 2006.

[33] Johnston, J. P., and Nishi, M., Vortex Generator Jets--Means for Flow Separation Control, *A1AA J.*, 28, 989 994, 1990.

[34] Compton, D. A., and Johnston, J. P., Streamwise Vortex Production by Pitched and Skewed Jets in a Turbulent Boundary Layer, *A1AA J.*, 30, 640-647, 1992.

[35] L. Lal, M. Miscevic , P. Lavieille M. Amokrane ,F. Pigache , F. Topin , B. Nogarde , Tadrist (2013.) An overview of heat transfer enhancement methods and new perspectives: Focus on active methods using electroactivmaterials, *International Journal of Heat and Mass Transfer*,vol 61, pp. 505-524.

[36] Tian-Hu Wang , Ming Peng , Xiao-Dong Wang , Wei-Mon Yan Investigation of heat transfer enhancement by electrohydrodynamics in a double-wall-heated channelInternational Journal of Heat and Mass Transfer 113 (2017) 373–383

[37] Kulacki, F. A., Davidson, J. H., and Dunn, P. F., Convective Heat Transfer with Electric and Magnetic Fields, Chapter 9 in *Handbook of Single-Phase Heat Transfer,* S. Kaka~, R. K. Shah, and W. Aung, Eds., Wiley, New York, 1987.

[38] Lemlich, R., Vibration and Pulsation Boost Heat Transfer, *Chem.Eng.*, pp. 171- 176, May 15, 1961.

[39] Dec, J. E., Keller, J. O., and Arpaci, V. S., Heat TransferEnhancement in the Oscillating Turbulent Flow of a Pulse Combustor Tail Pipe, *Int. J. Heat Mass Transfer,* 35, 2311-2325, 1992

[40] Chung, J. H., and Hyun, J. M., Heat Transfer from a Fully-Developed Pulsating Flow in a Curved Pipe, *Int. J. Heat Mass Transfer,* 37, 43 52, 1994.

[41] Gopinath, A., and Mills, A. F., Convective Heat Transfer from a Sphere Due to Acoustic Streaming, *J. Heat Transfi, r,* 115, 332-341, 1993.

[42] Tadhg S. O'Donovan, Darina B. Murray EFFECT OF ACOUSTIC EXCITATION ON THE HEAT TRANSFER TO AN IMPINGING AIR JET ASME-JSME Thermal Engineering Summer Heat Transfer Conference July, 8-12, 2007, Vancouver, British Columbia, CANADA

[43] B.L. Owsenek, J. Seyed-Yagoobi, R.H. Page, Experimental investigation of corona wind heat transfer enhancement with a heated horizontal flat plate, J. Heat Transfer 117 (1995) 309–315.

[44] B.L. Owsenek, J. Seyed-Yagoobi, Theoretical and experimental study of lectrohydrodynamic heat transfer enhancement through wire plate corona discharge, J. Heat Transfer 119 (1997) 604–610.

[45] D.B. Go, S.V. Garimell, T.S. Fisher, Ionic winds for locally enhanced cooling, J. Appl. Phys. 102 (2007) 053302.

[46] S. Laohalertdechaa, P. Naphonb, S. Wongwises, A review of electrohydrodynamic enhancement of heat transfer, Renew. Sustain. Energy Rev. 11 (2007) 858–876.

[47] M.S. Aris, I. Owen, C.J. Sutcliffe, The application of shape memory alloy as vortex generators and flow control devices for enhanced convective heat transfer, in: Proceedings of the Fifth Joint ASME/JSME Fluids Engineering Conference, FEDSM2007-37080, American Society of Mechanical Engineers, 2007.

[48] M.S. Aris, I. Owen, C.J. Sutcliffe, The application of shape memory alloy as longitudinal vortex generators for enhanced convective heat transfer, in: Proceedings of the 10th UK National Heat Transfer Conference, 2007.

[49] R. Lahoz, L. Grasia, J.A. Puertolas, Training of the two-way shape memory effect by bending in NiTi alloys, J. Eng. Mater. Technol. 124 (2002) 397–401.

[50] Zheng Li, Xianchen Xu, Kuojiang Li, Yangyang Chen a, Guoliang Huang, Chung-lung Chen, Chien-Hua Chen. A flapping vortex generator for heat transfer enhancement in a rectangular airside fin. International Journal of Heat and Mass Transfer 118 (2018) 1340–1356

[51] CD-Adapco, Star-CCM+, in: User guide version 8.06, 2013.

[52] Celik I.B., Ghia U., Roache P.J., Freitas C.J., Coleman H., Raad P.E., Procedure for Estimation and Reporting of Uncertainty Due to Discretization in CFD Applications, Journal of Fluids Engineering, 130 (2008) 078001-078001.

[53] ANSYS Academic Research, Release 15.0, Help system, ANSYS, Inc.

[54] K. Bathe. Finite element procedures. Klaus-Jurgen Bathe, 2006.

[55] J. Thompson, B. Soni, and N. Weatherill. Handbook of grid generation. CRC press, 1998.

[56] M. Schäfer and I. Teschauer. Numerical simulation of coupled fluid–solid problems. ComputerMethods in Applied Mechanics and Engineering, 190(28):3645–3667, 2001.

[57] F. Blom. A monolithical fluid-structure interaction algorithm applied to the piston problem.Computer methods in applied mechanics and engineering, 167(3):369–391, 1998.

[58] C. Felippa and K. Park. Staggered transient analysis procedures for coupled mechanical systems:formulation. Computer Methods in Applied Mechanics and Engineering, 24(1):61–111, 1980.

[59] S. Piperno. Explicit/implicit fluid/structure staggered procedures with a structural predictor and fluid subcycling for 2D inviscid aeroelastic simulations. *International Journal for Numerical Methods in Fluids*, 25(10):1207–1226, 1997.

[60] W. Wall, S. Genkinger, and E. Ramm. A strong coupling partitioned approach for fluid–structure interaction with free surfaces. *Computers & Fluids*, 36(1):169–183, 2007.

[61] B. Hübner, E. Walhorn, and D. Dinkler. A monolithic approach to fluid–structure interaction using space–time finite elements. *Computer Methods in Applied Mechanics and Engineering*, 193(23):2087–2104, 2004.

[62] A. Slone, K. Pericleous, C. Bailey, M. Cross, and C. Bennett. A finite volume unstructured mesh approach to dynamic fluid–structure interaction: an assessment of the challenge of predicting the onset of flutter. *Applied Mathematical Modelling*, 28(2):211–239, 2004.

[63] Lu G, Zhou G. Numerical simulation on performances of plane and curved winglet type vortex generator pairs with punched holes. Int. J. Heat Mass Transf. 2016;102:679e90.

[64]Dezan DJ, Salviano LO, Yanagihara JI. Heat transfer enhancement and optimization of flat-tube multilouvered fin compact heat exchangers with deltawinglet vortex generators. Appl. Therm. Eng. 2016;101:576e91.

[65] Jong Chull Jo, PRESSURE VESSELS AND PIPING SYSTEMS - Fluid-Structure Interactions, Korea Institute of Nuclear Safety, Republic of Korea

[66] T. Rabczuk, R. Gracie, J.H. Song, and T. Belytschko. Immersed particle method for fluid–structure interaction. International Journal for Numerical Methods in Engineering, 81(1):48–71, 2010.

[67] F. Sotiropoulos and X. Yang. Immersed boundary methods for simulating fluid–structure interaction. Progress in Aerospace Sciences, 65:1–21, 2014.

[68] F. Baaijens. A fictitious domain/mortar element method for fluid-structure interaction. *International Journal for Numerical Methods in Fluids*, 35(7):743–761, 2001.

UNIVERSITE BRETAGNE LOIRE

UNIVERSITÉ DE NANTES

Thèse de Doctorat

Assadour KHANJIAN

Génération auto-adaptative de vorticité pour des échangeurs de chaleur intelligents

Auto-Adapting Vortex Generator for Smart Heat Exchangers

Résumé

Cette étude repose sur différentes géométries de générateurs de vortex (VG) placées dans un canal rectangulaire. Un calcul numérique du transfert de chaleur par convection laminaire est pris en compte pour les cas VG statiques, et les cas turbulents sont étudiés pour les VG auto-adaptifs ; leur effet sur l'amélioration thermique du système est analysé.

Dans la première partie, deux géométries différentes de VG statique sont étudiées. Tout d'abord, un canal rectangulaire équipé d'un générateur de vortex à ailettes rectangulaires situé sur la paroi inférieure du canal est pris en compte. Différentes valeurs d'angle de roulis β comprises entre 20° et 90° sont prises en compte, tout en maintenant un angle d'attaque constant (α=30°).

Une seconde géométrie est prise en compte : une aile rectangulaire VG placée dans un écoulement entre des plaques parallèles avec différentes valeurs d'angles d'attaque [10°–30°]. Le nombre de Nusselt et le facteur de friction sont étudiés localement et globalement.

Ensuite, un VG contrôlé par la pression est proposé et l'interaction fluide-solide (FSI) est prise en compte : l'angle d'attaque du VG s'auto-adapte en fonction de la valeur de la vitesse d'entrée. Le nombre de Nusselt, le facteur de friction et le facteur d'amélioration thermique sont étudiés pour un régime d'écoulement turbulent. En parallèle, une étude expérimentale est réalisée pour une comparaison et une validation des résultats numériques obtenus.

Mots clés

Tourbillons longitudinaux ; amélioration du transfert de chaleur ; Interaction fluide-solide ; générateur de vortex à adaptation automatique ; efficacité énergétique.

Abstract

This study consists of different geometries of vortex generators (VG) placed in a rectangular channel. A numerical computation of laminar convection heat transfer is taken into consideration for static VG cases, and turbulent convection for the pressure driven VG, and their effect on the thermal enhancement of the system is analyzed.

In the first part, two different geometries of static VG are studied. First, a rectangular channel equipped with a rectangular winglet pair vortex generator located on the bottom wall of the channel, is taken into consideration. Different values of roll angle in the range [20°–90°] are considered, while maintaining a constant angle of attack equal to 30°.

A second geometry is taken into consideration: a rectangular wing VG placed in a parallel plate flow with different values of attack angles [10°–30°]. Nusselt number and friction factor are studied on local and global perspectives.
Then, a pressure driven VG is proposed and a computational design is set where the Fluid Structure Interaction (FSI) is taken into consideration: the angle of attack of the VG is auto adapted by the value of the inlet velocity. Nusselt number, friction factor and the thermal enhancement factor are studied for a turbulent flow regime. In parallel, an experimental study is done for a comparison and a validation of the numerical results obtained

Key Words

Longitudinal vortices; heat transfer enhancement; Fluid-structure interaction; Auto adaptive vortex generator; energy efficiency.